Multipass SAR Processing for Ice Sheet Vertical Velocity and Tomography Measurements

By

Gordon Ariho
BSc. Electrical Engineering, Makerere University, Uganda, 2003
MSc. Communication Engineering, University of Manchester, UK, 2009

Submitted to the graduate degree program in the Department of Electrical Engineering and Computer Science and the Graduate Faculty of the University of Kansas in partial fulfillment of the requirements for the degree of Doctor of Philosophy.

James Stiles, Chairperson

John Paden, Co-Chair

Shannon Blunt

Committee members

Christopher Allen

Emily Arnold

Date Defended: 27 April 2023

The dissertation committee for Gordon Ariho certifies that this is the approved version of the following dissertation:

Multipass SAR Processing for Ice Sheet Vertical Velocity and Tomography Measurements

_____

James Stiles, Chairperson

_____

John Paden, Co-Chair

Date Approved: 08 May 2023

Abstract

Vertical velocity is the rate at which ice moves vertically within an ice sheet, usually measured in meters per year. This movement can occur due to various factors, including accumulation, ice deformation, basal sliding, and subglacial melting. The measurement of vertical velocities within the ice sheet can assist in determining the age of the ice and assessing the rheology of the ice, thereby mitigating uncertainties due to analytical approximations in ice flow models.

We apply differential interferometric synthetic aperture radar (DInSAR) techniques to data from the Multichannel Coherent Radar Depth Sounder (MCoRDS) to measure the vertical displacement of englacial layers within an ice sheet. DInSAR's accuracy is usually on the order of a fraction of the wavelength (e.g., millimeter to centimeter precision is typical) in monitoring displacement along the radar line of sight (LOS). Ground-based Autonomous phase-sensitive Radio-Echo Sounder (ApRES) units have demonstrated the ability to precisely measure the relative vertical velocity by taking multiple measurements over time from the same location on the ice. Airborne systems can make a similar measurement but can suffer from deleterious spatial baseline effects since it is generally impossible to fly over the same stretch of ice on each pass with enough precision to ignore the spatial baseline. In this work, we compensate for spatial baseline errors using precise trajectory information and estimates of the cross-track layer slope using direction of arrival estimation. The current DInSAR algorithm is applied to airborne radar depth sounder data to produce results for flights near Summit Camp and the EGIG (Expéditions Glaciologiques Internationales au Groenland) line in Greenland. The existing approach estimates the parameters in multiple separated steps. However, each step has dependencies on all the values being estimated. To overcome this drawback, we have implemented a maximum likelihood estimator that jointly estimates the vertical velocity, the cross-track internal layer slope, and the unknown baseline error

due to GPS and INS (Inertial Navigation System) errors. We incorporate the Lliboutry parametric model for vertical velocity into the maximum likelihood estimator framework.

To improve the direction of arrival estimation of the internal layer slope, we also explore the use of focusing matrices against other wideband direction of arrival methods, such as wideband MLE, wideband MUSIC, and wideband MVDR, by comparing the mean squared error of the DOA estimates.

Acknowledgments

I want to thank God, who has enabled me to accomplish this milestone in my academic career. I am deeply grateful to my Ph.D. committee members for their invaluable support and guidance throughout my research journey. Their insights and feedback have been crucial to the completion of this dissertation. I sincerely thank my advisors, Dr. James Stiles and Dr. John Paden, for their unwavering support, patience, and encouragement. Their expertise and guidance were instrumental in shaping my research and refining my ideas.

I also want to thank my committee members, Dr. Shannon Blunt, Dr. Christopher Allen, Dr. Emily Arnold, and Dr. Carl Leuschen, for their feedback, suggestions, and comments. Their contributions helped me to identify new avenues of research and improve the quality of my work. I would also like to thank Dr. Victor Frost, who guided me at the beginning of my studies as I transitioned from industry to being a graduate student. His encouragement and guidance helped me not to quit. I am particularly indebted to Dr. Stiles, who taught me several valuable courses during my study but also shared great wisdom from his own experiences about transitioning from industry to being a graduate student. I have no words to describe what Dr. Paden has been in my life and my academic career. He has been a great mentor and thorough advisor with whom I have worked closely for the most part of my Ph.D. career.

I am grateful to the staff and faculty at the University of Kansas for their support and assistance throughout my Ph.D. program. Their dedication to teaching and research has inspired me to pursue my academic goals and helped me develop as a scholar.

I thank Dr. Nick Holschuh (Amherst College), Dr. Christiansson Knut (University of Washington), and Andrew Hoffman (University of Washington) for their invaluable support and guidance on glaciology-related works. I thank the Nichols Hall community, which has become like a family to

me, especially the students from I2S and CReSIS. I thank my fellow Ph.D. students in CReSIS (Talasila Hara Madhav and Ibukunle Oluwasonila) and previous graduates (Mohanad, Anjali Pare, and others) who have shared great moments and wisdom with me.

Finally, I want to express my gratitude to my family and friends for their love, support, and encouragement. Their unwavering belief in me and my abilities has strengthened and motivated me throughout my Ph.D. journey. I thank my parents, Aggrey and Beatrice Ndyaba, for always believing in me and supporting me in every way. I thank my siblings Doreen Ninsiima, Tony Ahumuza, Doris Atuhaire, Daisy Asiimwe, Donah Arinda, Samuel Mushabe, Samantha Nowamaani, and Uncle Seres for holding me up and keeping things running in Uganda while I was away for studies.

Dedication

I dedicate this dissertation to my dear family who either paused their lives for this academic adventure or were born during my Ph.D. adventure: Charlotte A. Kukundakwe, Curtis A. Akoragye, Gabriel A. Akampa, and Emmanuel C. A. Abaho.

I also dedicate this dissertation to my parents, Aggrey and Beatrice Ndyaba, who have always believed in me and supported my endeavors.

Table of Contents

List of Figures

List of Tables

1 INTRODUCTION

The quest to unravel the mysteries beyond human perception has captivated humanity for centuries. By the late 19th Century, Heinrich Hertz demonstrated that metallic objects could reflect radio waves, confirming the earlier hypothesis postulated by James C. Maxwell in his electromagnetism work [1]. In 1904, Christian Hülsmeyer built a ship detection device for collision avoidance based on this principle [2]. Radar, which stands for radio detection and ranging, was born out of this and has grown to be applied in various remote sensing-based applications. World War II further accelerated the development of radar technology, and as such, radar has deep military roots. There are also a growing number of civilian applications [3].

Radar works by transmitting electromagnetic (EM) waves toward a region of interest with targets and then receiving and detecting these EM waves after scattering from objects in that region. The major subsystems of a typical radar include a transmitter, an antenna, a receiver, and a signal processor, as shown in Figure 1-1.

The transmitter generates the EM waves fed into an antenna that introduces them into the propagation medium, usually the atmosphere. If a standard antenna is used for transmit and receive, a transmit/receive (T/R) device (usually a circulator or a switch) allows the transmitter and receiver to be attached simultaneously. At the same time, the T/R device provides isolation between the transmitter and receiver to protect the sensitive receiver components from the high-power transmit signal. The transmitted signal propagates through the medium to the target and induces currents on the target. The target reradiates into the environment and back to the antenna (and receiver circuitry). The received signal at the antenna is a linear superposition of the desired targets and unwanted clutter signals. The receiver circuitry amplifies, filters, and subsequently digitizes the signal with an analog-to-digital converter (ADC). A detector removes the carrier from

the modulated target return signal. The signal processor then analyzes the ADC-captured target data.

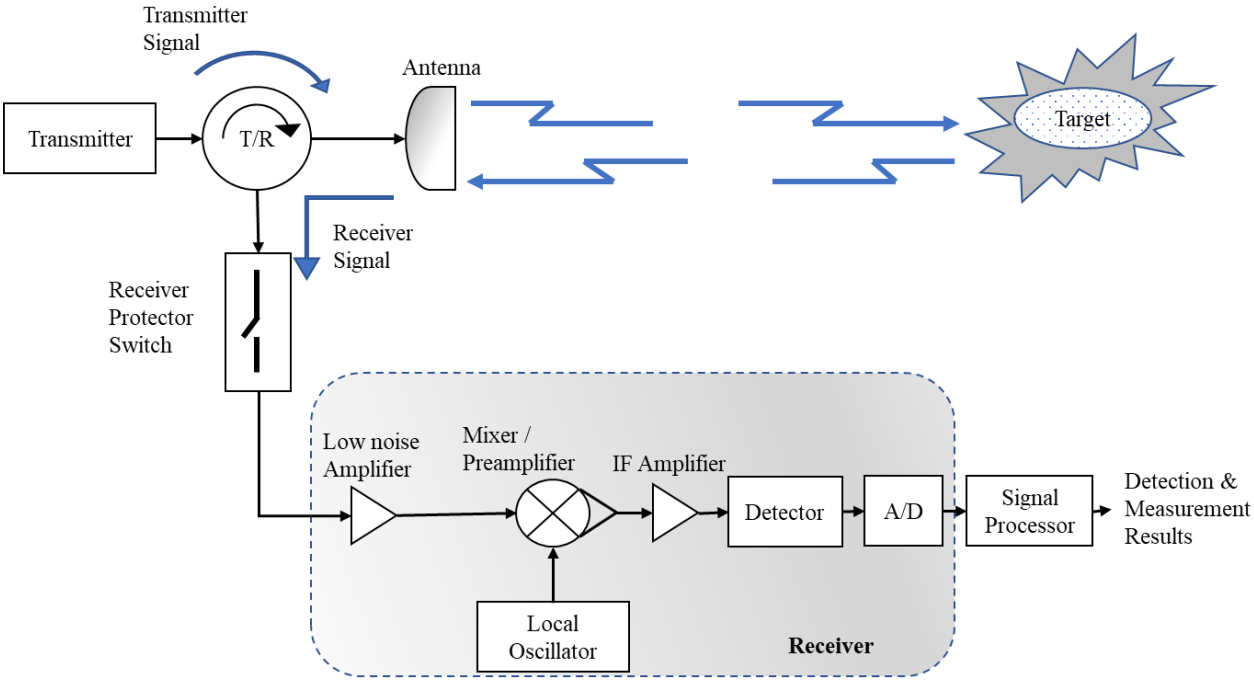

Figure 1-1: Example radar transmission/reception process [4].

Since the signal travels to and from the target, we can find the range, R to the target by using the distance equals the speed of light, c, multiplied by time, t_d , equation. We divide this by 2 to account for the two-way travel time.

$$R = \frac{c \times t_d}{2} \tag{1.1}$$

Generally, the returned signal will have interference from internal and external sources. The fundamental function of the radar's signal processor is to determine the presence of a target and/or estimate some target property in the presence of noise [4].

Radar has been extensively applied in remote sensing of ice sheets because ice (water) exhibits exceptionally low attenuation in specific regions of the electromagnetic spectrum, as

illustrated in Figure 1-2. This dissertation centers on the utilization of multipass radar sounder interferometry and tomography to investigate ice sheets.

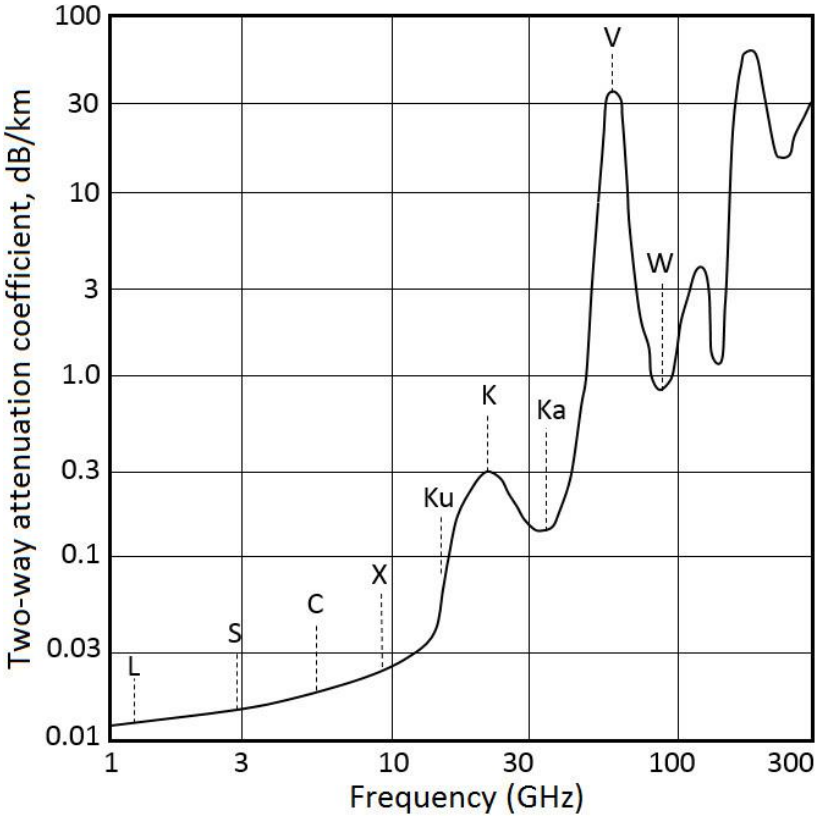

Figure 1-2: Attenuation of water versus frequency bands [5].

Ice sheets are a significant part of the Earth's system, and studying their behavior, especially the ice-sheet mass balance, which directly affects sea level rise, is therefore essential. Ice-sheet mass balance refers to the ice mass gain (accumulation) in relation to loss (ablation), and negative mass balance occurs if the loss exceeds the gain. Another example of how ice sheets affect the Earth's system is that meltwater from ice shelves (and melting icebergs) can lead to changes in the ocean's freshwater balance, hence affect climatic and ecological outcomes. Radar remote sensing can measure the thickness and changes in the ice sheets, including ice shelves. The measurements help reduce uncertainties in predicting these climatic and ecological outcomes [6]. The Center for

Remote Sensing and Integrated Systems (CReSIS) develops radar systems and techniques to study ice sheets, and this dissertation focuses on using data collected by the CReSIS multichannel coherent radar depth sounder (MCoRDS) [7].

1.1 CReSIS Radar Depth Sounder

CReSIS radar depth sounders (RDS) provide crucial boundary condition information to inform ice sheet models and facilitate other ice sheet analyses [8]. The RDS dataset comprises geolocated radar profile images along with ice thickness, ice surface, and ice bottom elevations acquired over Greenland, Canada, Alaska, and Antarctica. The RDS operates by transmitting a pulse of RF energy into the ice sheet, where a fraction of the energy reflects from the ice surface, ice bottom, and englacial targets; the reflections being caused by a contrast in the (electromagnetic) constitutive properties of the medium. The data collected by the RDSs have been continuously acquired since 1993, with support from NASA and NSF grants.

In the context of radio frequency signal propagation through the ice, it is typically observed that the signal detected from the ice surface is of greater magnitude than the signal received from the ice bottom. This is due to the attenuation of RF signals as they traverse through the ice and the greater range to the target. To adequately capture the large dynamic range of these signals, distinct receiver gains are used. To optimize the sensing capabilities of RF signals in ice, using multiple waveforms of varying pulse durations, usually two or three, is favored over a single pulse duration. In this regard, a waveform with a short pulse duration is employed for nearby targets that do not necessitate high sensitivity. For instance, a pulse with a duration of 1 μs coupled with lower receiver gain settings is utilized to measure the round-trip signal time for the ice surface echo. This way, the transmitter can be fully off before the returned signal arrives. Conversely, a pulse with a

longer duration of 10 μs and higher receiver gain settings is used to measure the round-trip signal time for the ice bottom echo, thereby enabling enhanced sensitivity.

1.2 Ice-Sheet Modeling

It is widely acknowledged within the literature that models, inherently approximations of complex realities, should not be unequivocally relied upon to produce perfect outcomes. However, as George Box (1987) wrote, "*all models are wrong, but some are useful*," we can use models to glean some understanding of the complex reality. Simulation of historical variations by models of the glaciers and ice sheets can enable the projection of forthcoming changes. These models need to consider two primary factors: the mass change induced by accumulation (snowfall) and ablation (snowmelt) on the glacier, and the ice flow under its weight [9].

Currently, ice sheet models are built upon 2D assumptions, as illustrated in Figure 1-3 for the Pine Island Glacier. The ice sheet's contribution to sea level rise (Figure 1-6) can be predicted using a 2D finite element model (Figure 1-3), the observed surface velocity (Figure 1-4), ice thickness (Figure 1-5), and other variables like climatic variables (such as temperature, precipitation, and wind patterns), oceanic variables (such as the temperature and salinity of the ocean), and glacier geometry. The inputs used to predict sea level rise from glaciers can be quite complex and may involve a range of environmental factors. A 2D finite element model is a mathematical representation that approximates the behavior of a physical system in two dimensions, such as the surface of an ice sheet. The model divides the system into small geometric shapes called finite elements and approximates the behavior of each element using mathematical equations. The model takes into account the physical properties of the system, such as the mechanical properties of the ice, and the boundary conditions, such as the forces acting on the ice. By solving the equations for each element, the model can be used to predict the behavior of the system as a whole.

The models typically used to simulate the ice sheet for sea-level projection are finite element models. They usually use a thin-film approximation (Shallow Ice Approximation) for the vertical velocity structure. Part of this comes from the fact that historically it has not been possible to measure the distributed vertical velocity of the ice sheet. So, these models have not been developed to naturally incorporate englacial datasets like radar layer geometry and radar-derived vertical velocity. This research enables the creation of reliable vertical velocity datasets that can be incorporated into new or updated ice sheet models.

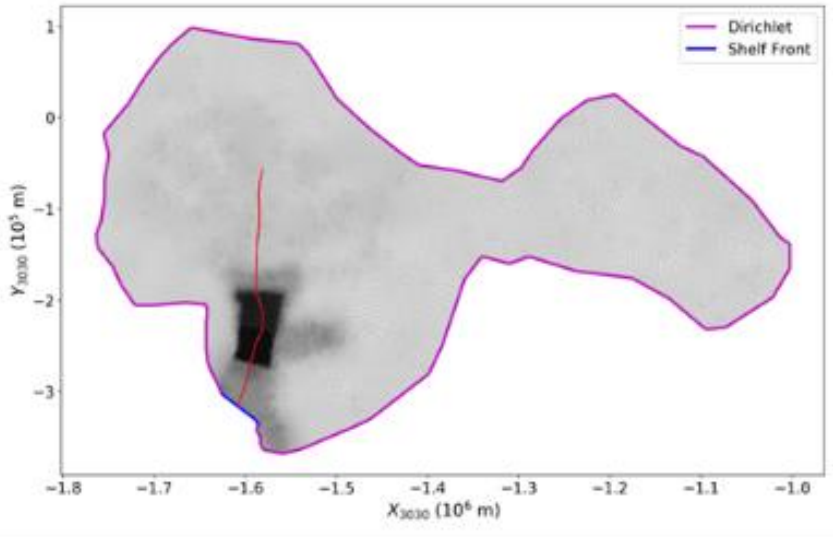

Figure 1-3: 2D finite element model and mesh of glaciated catchment [10].

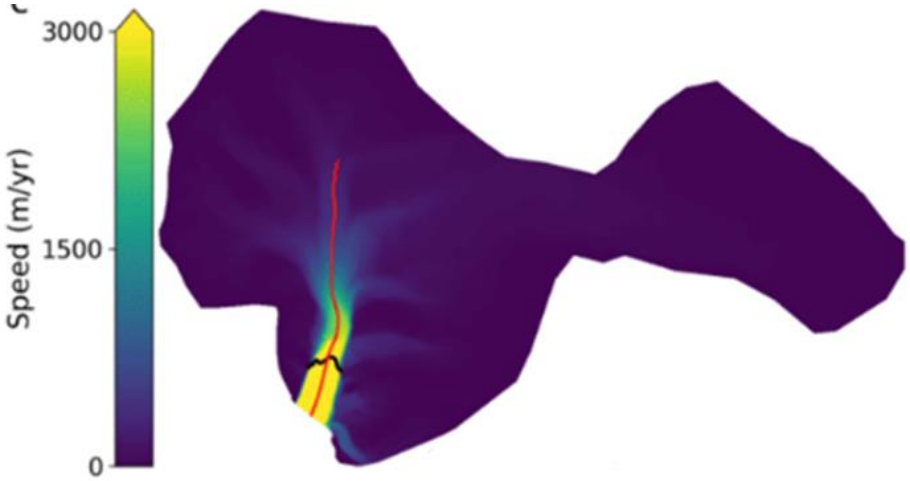

Figure 1-4: Observations of surface velocity [10].

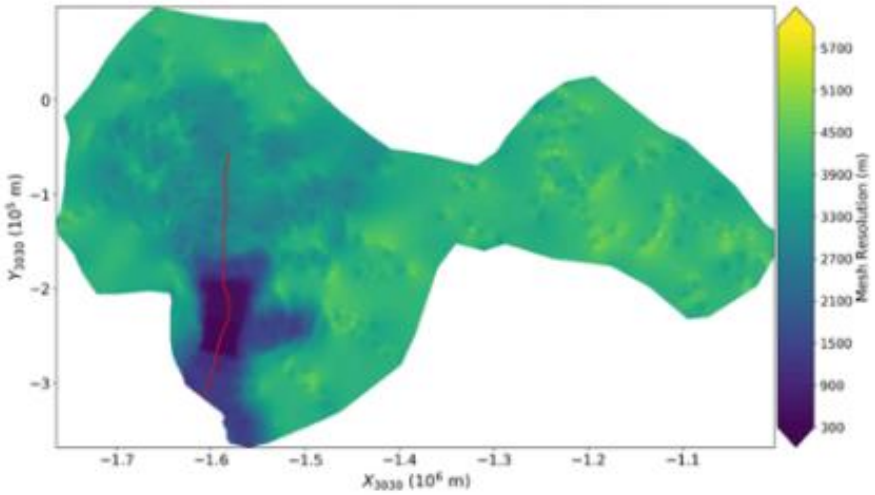

Figure 1-5: Ice thickness determined from ice-penetrating radar like MCoRDS [10]

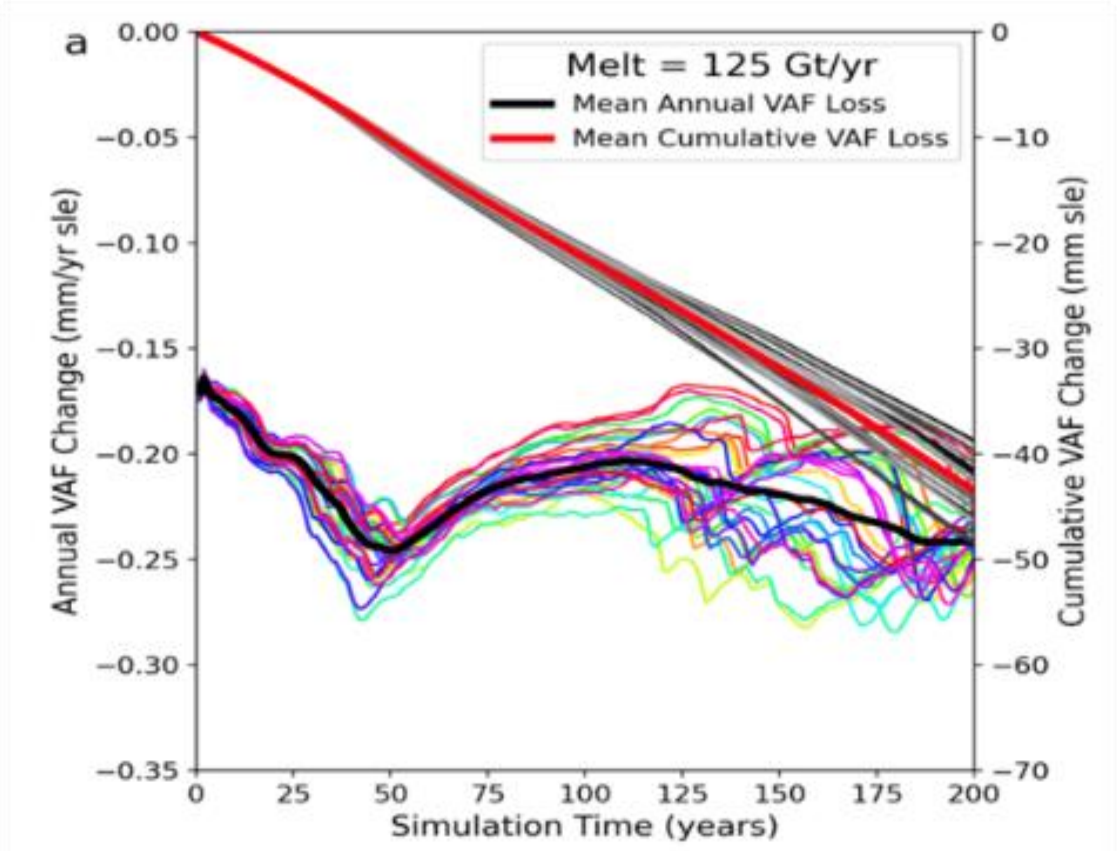

Figure 1-6: Prediction of ice sheet contribution to sea-level [10].

1.3 Motivation

The mass balance of ice sheets is a pivotal determinant in rising sea levels. Accurately predicting future sea-level rise relies heavily on reducing parametric uncertainty in ice-sheet models. Ice sheet flow models can benefit from englacial ice velocity measurements. Stationary ground-based Radio-Echo Sounders, like ApRES units, are being used to produce vertical velocity fields. However, the coverage of such systems is limited, and their precise positioning is achieved either by leaving them in position between repeat measurements or by using markers (flags) to ensure zero spatial baselines.

In contrast, airborne systems can cover larger areas but suffer from unknown baseline errors due to GPS and Inertial Navigation System (INS) errors. Currently, the airborne DInSAR algorithm estimates the baseline error due to GPS after Direction of Arrival (DOA) estimation. However, the accuracy of DOA estimation is contingent upon a precise baseline. Therefore, a Joint Maximum Likelihood Estimation (MLE) of the parameters is proposed to mitigate this issue. Comprehensive research endeavors are warranted to better understand the physical processes driving ice sheet mass balance and enhance our capacity to forecast its evolution in the face of ongoing climate change.

1.4 Study Area Location

The Summit region in Greenland has been chosen as the study area for this research. The Summit region, as shown in Figure 1-7, is situated in the central part of the Greenland ice sheet, and it is the highest point of the ice sheet, reaching an elevation of about 3,216 meters (10,551 feet) above sea level. This location provides a unique opportunity to study the dynamics of the Greenland ice sheet and its response to climate change.

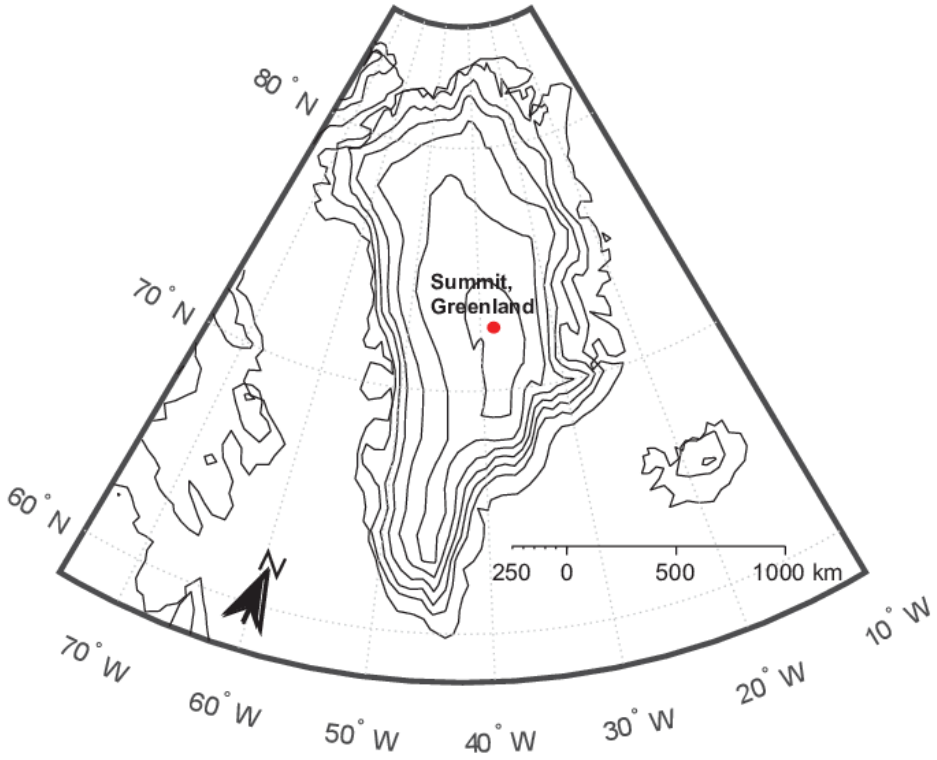

Figure 1-7. Geolocation of the study area [11]. (*Credit: A. Adolph, M. Albert, and D. Hall*)

One of the primary reasons for selecting the Summit region as the study area is the availability of good-quality data within the CReSIS archives. The CReSIS program is a collaborative effort between several institutions and government agencies to collect and analyze data on the Earth's polar ice sheets using airborne and satellite-based remote sensing technologies. The Summit region has been surveyed by the CReSIS program for many years, resulting in a wealth of data that can be used to study various aspects of the Greenland ice sheet, such as its thickness, velocity, and internal structure.

Another advantage of the Summit region is the presence of ground truth data that can be used to validate the results of the joint estimation process. Ice cores, for example, provide a record of past climate change that can be used to evaluate the accuracy of the proposed joint estimation algorithm. Additionally, crossing lines allow for accurate measurement of ice thickness and other

relevant parameters (e.g. layer slopes), which can be used to calibrate and validate remote sensing measurements. Another ground-based system that can provide valuable validation information for the Summit region is the phase-sensitive Radio Echo Sounder (pRES) (Figure 1-8) which can accurately measure the ice sheet's thickness and other parameters. While the pRES system has less coverage than airborne systems, its accuracy makes it a vital ground truth data source.

The Summit region in Greenland is an ideal location for this research and for studying the dynamics of the Greenland ice sheet due to the wealth of available data and ground truth information.

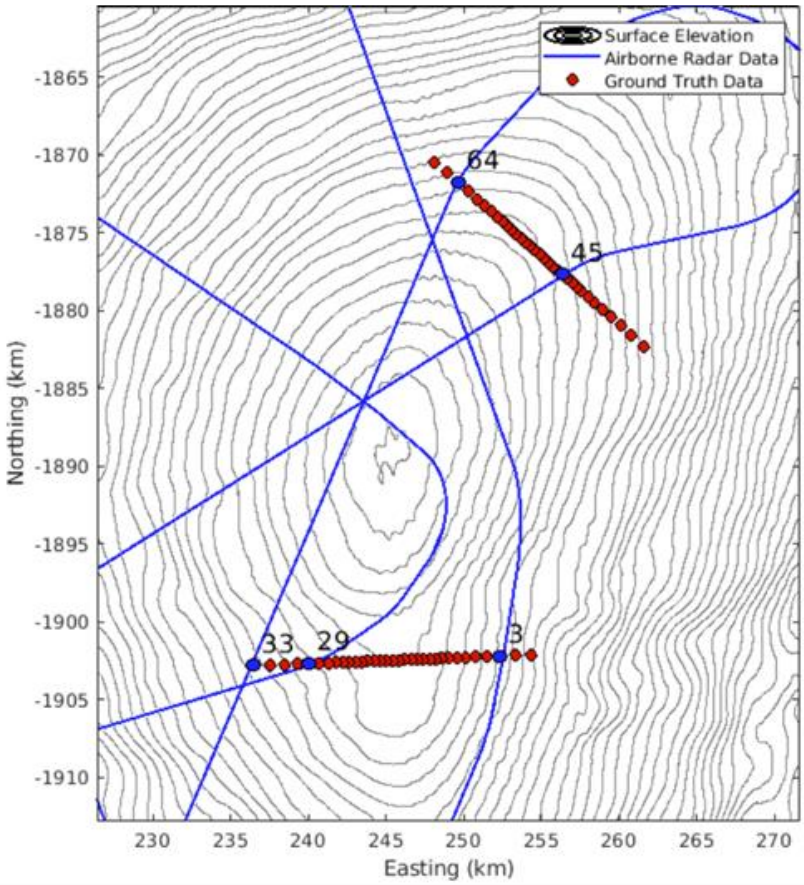

Figure 1-8. Map showing the Summit flight lines relative to ground-based (pRES) data collection. (*Credit: Dr. Nick Holschuh*)

1.5 Dissertation Outline

This dissertation addresses two main problems: joint estimation in multipass interferometry and focusing matrices for wideband tomographic processing. Chapter 2 covers the general background to introduce concepts necessary to understand the two problems: synthetic aperture radar (SAR), direction of arrival (DOA) estimation, and interferometry.

Chapter 3 discusses the multipass interferometry application in estimating ice layer displacement and cross-track slope. This chapter includes the results of the joint estimation framework using simulated data and actual data from CRESIS. It also compares the results from joint estimation with ground truth data.

Chapter 4 looks at the application of focusing matrices in DOA estimation for wideband arrays compared to other wideband methods.

Chapter 5 highlights the conclusions and recommendations drawn from the results in Chapters 3 and 4.

1.6 Notation and Terminology

Where it is not explicitly stated, the following terminology will be used:

The letter j denotes the imaginary part of a number and is defined as $\sqrt{-1}$.

Scalar quantities are denoted by uppercase or lowercase letters, while vector quantities are denoted by boldface, lowercase letters. Matrices are represented by boldface, uppercase letters.

Complex conjugation is denoted by $(\cdot)^*$.

$(\cdot)^T$ denotes the vector or matrix transpose operation.

$(\cdot)^H$ denotes the complex conjugate, or Hermitian vector or matrix transpose.

$\mathrm{Tr}(\cdot)$ is the trace operator.

The symbol $*$ denotes convolution.

Vertical bars $|\cdot|$ denote the modulus of a complex number or the magnitude of a real number. When around a vector, the vertical bars denote the Euclidean norm.

Double vertical bars $\|\cdot\|$ denote the Frobenius matrix norm.

1.7 Publication Record

Two conference papers were presented in 2020 and 2022 at the International Geoscience and Remote Sensing Symposium (IGARSS) and the International Symposium on Phased Array Systems and Technology (PAST), respectively. There is one paper on sparse array processing that is in the process of being submitted to the IEEE Transactions on Radar Systems. The list of publications is summarized here:

1. B. Miller, G. Ariho, J. Paden and E. Arnold, "Multipass SAR Processing for Radar Depth Sounder Clutter Suppression, Tomographic Processing, and Displacement Measurements," IGARSS 2020 - 2020 IEEE International Geoscience and Remote Sensing Symposium, 2020, pp. 822-825, doi: 10.1109/IGARSS39084.2020.9324498.
2. G. Ariho, J. Paden, A. Hoffman, K. Christianson and N. D. Holschuh, “Joint estimation of ice sheet vertical velocity and englacial layer geometry from multipass synthetic aperture radar data,” PAST 2022 – 2022 International Symposium on Phased Array Systems and Technology
3. G. Ariho, J. M. Stiles, and P. S. Tan “Processing of Non-contiguous Radar Transmission Spectra,” (*to be submitted to the IEEE Transactions on Radar Systems*)

2 BACKGROUND

This chapter aims to comprehensively review the background and fundamentals of SAR, InSAR, DInSAR, and related techniques. This review will set the stage for a detailed discussion of multipass interferometry, which represents a critical component in estimating the vertical velocities of ice sheets.

2.1 Introduction

Interferometry utilizes the phase difference between two Synthetic Aperture Radar (SAR) images to generate a geometric terrain image of the scene. Interferometric SAR (InSAR) combines (i.e., interferes) two images acquired from marginally different positions or phase centers to produce three-dimensional (topographic) images of the earth's surface. Differential InSAR (DInSAR) is an advanced technique that builds upon the principles of conventional InSAR to enable precise measurements of surface deformation over time. Both InSAR and DInSAR make use of the interferometric phase to deduce changes in the range to the scene between 2 or more SAR images; InSAR handles the phase variations due to the elevation angle of the target, and DInSAR handles the phase variations due to radial or range displacements of the target over time.

2.2 Synthetic Aperture Radar (SAR)

Synthetic aperture radar (SAR) is a coherent active remote sensing system that exploits the platform motion to simulate a very large antenna (aperture) electronically, using the fact that several (usually many) pulses illuminate the target (image scene) as the radar beam passes over it. A coherent combination of the received signals permits the realization of an effective simulated aperture that is considerably longer than the physical antenna length. Figure 2-1 illustrates the formation of a synthetic antenna array. Compared to the real (physical) aperture, this larger

synthetic aperture leads to finer spatial resolution in the SAR image. A SAR image is a two-dimensional map of the scattering intensity of the image scene. Each pixel in the radar image is a complex number representing the energy scattered back to the antenna. When multiple antennas arrayed in the cross-track dimension each collect SAR data, the SAR images can be combined to generate three-dimensional images of the scene [12].

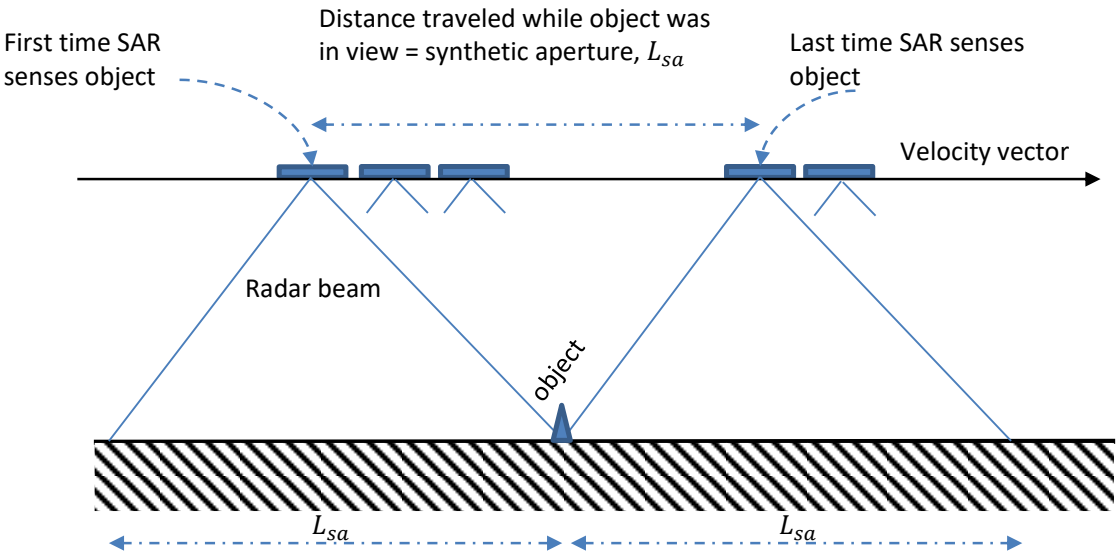

Figure 2-1: Formation of a synthetic antenna array considering horizontal beamwidth on the ground.

For a real aperture radar (RAR), the spatial resolution depends on the size of the physical antenna used, pulse duration (τ_p), and the antenna beamwidth. The larger the antenna, the finer the spatial resolution. This dependence on the antenna's physical size can lead to typical resolutions on the order of several kilometers. The range, σ_r, and azimuth, σ_x, resolution for RAR are defined in equations 2.1 and 2.2, respectively.

$$\sigma_r = \frac{c\tau_p}{2} \qquad 2.1$$

where c is the speed of light, and τ_p is the compressed pulse duration. For side-looking radar, the ground range resolution is $\sigma_{gr} = \frac{\sigma_r}{\sin(\theta_i)}$ where θ_i is the incidence angle. The azimuth resolution is given by:

$$\sigma_{x,RAR} \approx \frac{\lambda R}{d_a}, \tag{2.2}$$

where d_a is the physical/real antenna length, R is the distance between the antenna and the object, and λ is the wavelength of the center frequency.

SAR benefits from the Doppler history of the radar echoes to synthesize a very large antenna that allows finer azimuth resolution despite a physically small antenna. Taking the beamwidth of an antenna of length d_a to be approximately $\beta_a = \lambda/d_a$, we can deduce from Figure 2-2 that the corresponding maximum synthetic aperture length is given by $L_{sa} = \beta_a R_o = \lambda R_o/d_a$. R_o is the slant range associated with the range of closest approach to the target. The synthetic beamwidth for this aperture is $\beta_{sa} = \lambda/2L_{sa}$ where the factor of 2 occurs since both the transmit and receive path are affected when the radar platform is moved; hence doubling the effect. This results in the azimuth resolution, σ_x, given in Equation 2.3.

$$\sigma_x = R_0\beta_{sa} = R_0\frac{\lambda}{2L_{sa}} = \frac{d_a}{2} \tag{2.3}$$

Equation 2.3 shows that the azimuth resolution for SAR is independent of both the wavelength and the distance from the radar to the target. It further suggests that a shorter antenna offers the potential for a finer azimuth resolution because a larger synthetic aperture can be constructed due to the wide beamwidth of a smaller antenna [13]. Very small resolution cells are achievable since the azimuth resolution is directly proportional to the length of the actual antenna. However, SAR

data are rarely processed at the finest possible resolution because of the desire to average the returns over several neighboring resolution cells to reduce speckle noise [14].

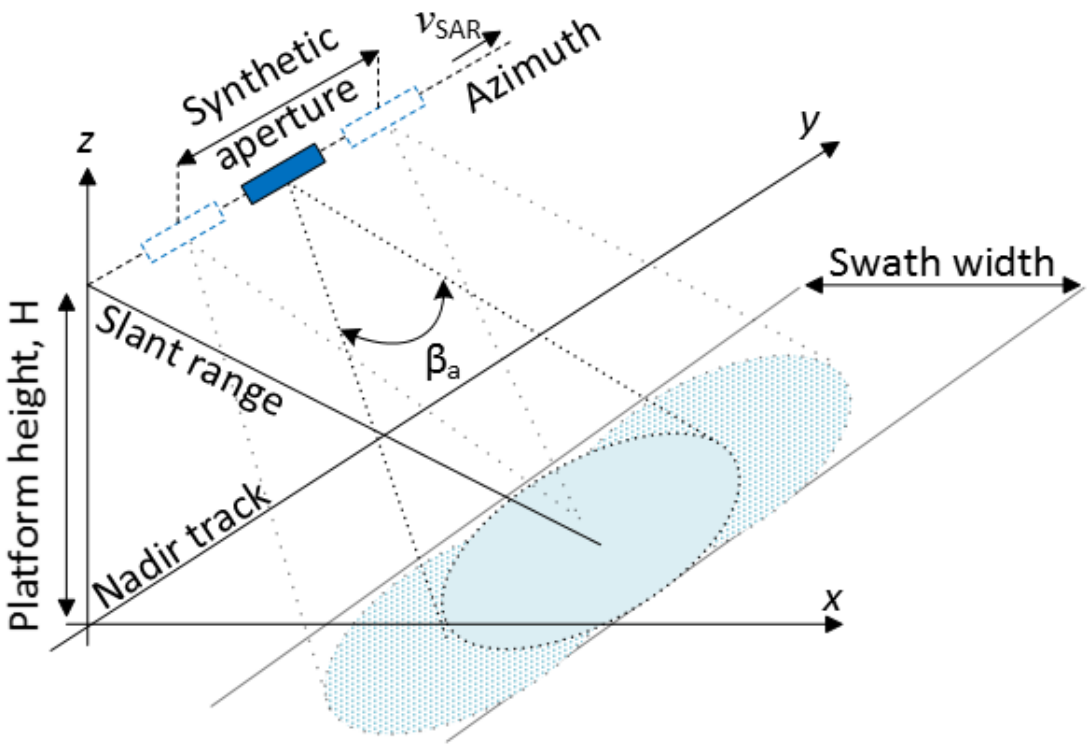

Figure 2-2: Illustration of the SAR imaging geometry. β_a is the azimuth beamwidth and v_{SAR} is the sensor velocity[13].

The two-dimensional image scene produced by SAR processing is a result of the coherent matched filter processing of the raw data, also known as phase history. The processed/focused image has two orthogonal axes: the range axis, determined by the time delay of the received pulse, and the cross-range (azimuth) axis, determined by the synthetic aperture length. To obtain a geocoded image of the physical features of the image scene, the physical features are projected into the two-dimensional ground plane during processing, shown by the swath in Figure 2-2 [15].

The SAR image can have fine resolution in the range direction due to the use of wide bandwidth pulses like the linear frequency modulated chirp (Equation 2.4).

$$s(t) = rect\left(\frac{t}{T_{pd}}\right) e^{j(2\pi f_c t + \pi \alpha t^2)} \quad 2.4$$

where the pulse has a carrier frequency f_c, frequency modulation (FM) or chirp rate α, and duration T_{pd}.

The SAR image also has a fine resolution in the cross-range direction because of the use of a synthesized antenna and coherent processing of the phase history of the received signals from several successive pulses (also known as azimuth compression). Before the signal processing begins, the collection of the target's total phase and amplitude history for the duration of the integration or dwell time is required. Typical integration times are application dependent but usually on the order of a second [15]. SAR resolves both the amplitude and phase of the backscattered echoes. However, the phase of a single SAR image is generally of no practical use except when there are two (or more) SAR images that can be used to form an interferometric pair or pairs.

2.3 Interferometric Synthetic Aperture Radar (InSAR)

Interferometric SAR uses the differential phase from multiple passes or multiple displaced phase-centers on a single pass to form an image known as an interferogram (measured in radians of phase difference). The distance between two passes in the plane perpendicular to the flight path is called the interferometer baseline, B (Figure 2-3), and its projection perpendicular to the slant range is the perpendicular baseline, $B_\perp$. The slave image is co-registered and resampled to the same grid as the master image. The interferogram is the product of the master image and the conjugate of the slave image.

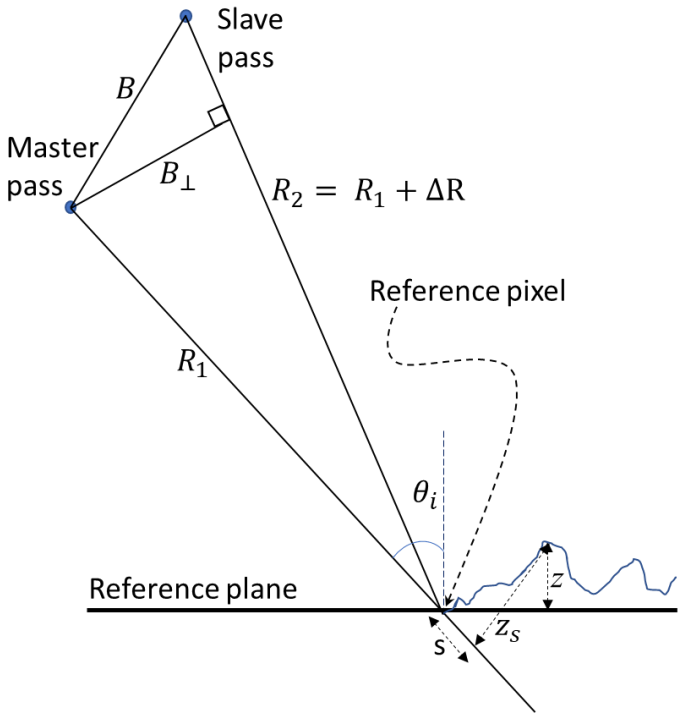

Figure 2-3: InSAR geometry.

If we approximate the transmitted signal (of wavelength λ) to a pure sinusoid with phase ϕ, that has a linear relationship with the slant range coordinate, r, we can write:

$$\phi = \frac{2\pi r}{\lambda}. \qquad 2.5$$

Assuming that the transmitted signal has a phase of zero, then the backscattered signal that travels a distance of $2R$, incurs a phase delay (in radians) of:

$$\phi = -\frac{4\pi R}{\lambda} + \phi_{scat}, \qquad 2.6$$

where ϕ_{scat} is the phase due to the scattering within the resolution cell.

So, for the master and slave pass, we have $\phi_1 = -\frac{4\pi R_1}{\lambda} + \phi_{scat,1}$ and $\phi_2 = -\frac{4\pi R_2}{\lambda} + \phi_{scat,2}$ respectively. Therefore, the interferometric phase is then given by:

$$\phi_{int} = \phi_2 - \phi_1 = \left(-\frac{4\pi R_2}{\lambda} + \phi_{scat,2}\right) - \left(-\frac{4\pi R_1}{\lambda} + \phi_{scat,1}\right). \quad 2.7$$

Since $R_2 = R_1 + \Delta R$ and if we assume the scattering phases are approximately the same so that $\phi_{scat,1} \approx \phi_{scat,2}$, we can rewrite Equation 2.7 as:

$$\phi_{int} = -\frac{4\pi \Delta \mathrm{R}}{\lambda}. \quad 2.8$$

The scattering phases are the same when the baseline is small enough that the target scattering is coherent between the two passes. This is the case as long the baseline is less than the critical baseline for the target, and the target scattering properties have not changed [16].

The interferogram phase changes from one range bin to the next due to the slight change in the look angle between the range bins. If we denote the perpendicular-to-the-slant-range offset between one range bin and the next range bin as z_s, then the change in interferometric range, ΔR, between the neighboring range bins can be approximated by $B_\perp z_s/R$ such that Equation 2.8 becomes [17];

$$\phi_{int} = -\frac{4\pi}{\lambda}\frac{B_\perp z_s}{R}. \quad 2.9$$

This interferometric phase variation can be divided into two contributions: one related to the difference in elevation z between the two neighboring range bins, and the other proportional to the slant range displacement s between the two neighboring range bins assuming a flat reference plane as shown in Equation 2.10 [18].

$$\phi_{int} = -\frac{4\pi}{\lambda}\frac{B_\perp z}{R\sin\theta_i} - \frac{4\pi}{\lambda}\frac{B_\perp s}{R\tan\theta_i} \quad 2.10$$

The operation of computing and subtracting the already known second term in Equation 2.10 from the interferometric phase is known as *interferogram flattening* or removal of the flat earth

interferometric phase. This operation creates a phase map proportional to the relative terrain elevation.

To produce an interferogram, two (or more) SAR images corresponding to the master and slave passes are first coregistered by correlation to find the offset and difference in geometry between the two images. The slave image is then re-sampled to match the geometry of the master image, such that pixels are aligned to the same area on the ground in both images. Then, the conjugate multiplication of each pixel within the two images (i.e., the slave image with the complex conjugate of the master image) and removal of the phase due to the nominal or known elevation of the scene (interferogram flattening) creates the interferogram. The interferometric phase at each SAR image pixel is only influenced by the change in the travel paths from the SAR sensor to the resolution cell in consideration during the acquisition of each image. Phase unwrapping is then applied to produce a continuous deformation field by adding integer multiples of 2π phase, usually in a way that minimizes the overall phase discontinuities and produces the smoothest possible phase map. At this point, incoherent areas of the image may be masked out since low coherence usually indicates the phase is unreliable. Finally, the interferogram is geocoded by resampling from the acquisition geometry into the preferred geographic projection [17, 19, 20].

It should be noted that there is an upper limit of the spatial baseline (the critical baseline, B_c), over which the interferometric phase is pure noise. For a distributed area target, the critical baseline is

$$B_c = \frac{\Delta f R \tan(\theta - \gamma)}{f_o} \tag{2.11}$$

where Δf is the chirp bandwidth of the radar system; R denotes the distance from the sensor to the target; f_0 is the transmit frequency; θ is the incidence angle; γ represents the slope angle of the ground surface or landform, which is generally ignored for simplification [16].

Interferometric SAR is used to measure tectonic deformation, volcanic inflation, ground subsidence, glacier movement (ice flow and tidal flexing), the stability of built structures, and to produce digital elevation maps (DEMs).

2.4 Differential Interferometric Synthetic Aperture Radar (DInSAR)

Differential InSAR (DInSAR) [21] reveals the respective topographic changes of an image scene that occurred during the time period between the first pass and the current pass, for example, in the event of subsidence. The topographic changes of an image scene over time introduce an additive phase term that is independent of the baseline; $\Delta\phi_d = 4\pi d/\lambda$, where d is the relative scatterer displacement projected onto the slant range direction. The flattened interferometric phase now comprises both the altitude (surface elevation) and motion contributions:

$$\phi_{int} = -\frac{4\pi}{\lambda}\frac{B_\perp z}{R\sin\theta_i} + \frac{4\pi}{\lambda}d. \qquad 2.12$$

To get the differential interferogram, the altitude contribution must be subtracted from the interferometric phase, so a DEM must be available for the motion component to be measured.

The basic principle of the DInSAR technique is illustrated in Figure 2-4 for a single-pixel footprint. During the master pass, the sensor generates the first SAR image at a time t_0 associated with the phase Φ_M. Then during the next pass, which is referred to as the slave pass, the sensor acquires a second SAR image at a time t associated with the phase Φ_S and a land displacement $z(t)$ from point $P(t_0)$ to $P'(t)$. DInSAR methods take advantage of the phase difference $\Phi_{int} = \Phi_M - \Phi_S$ (i.e., the interferometric phase) to reveal information about the land displacement $z(t)$.

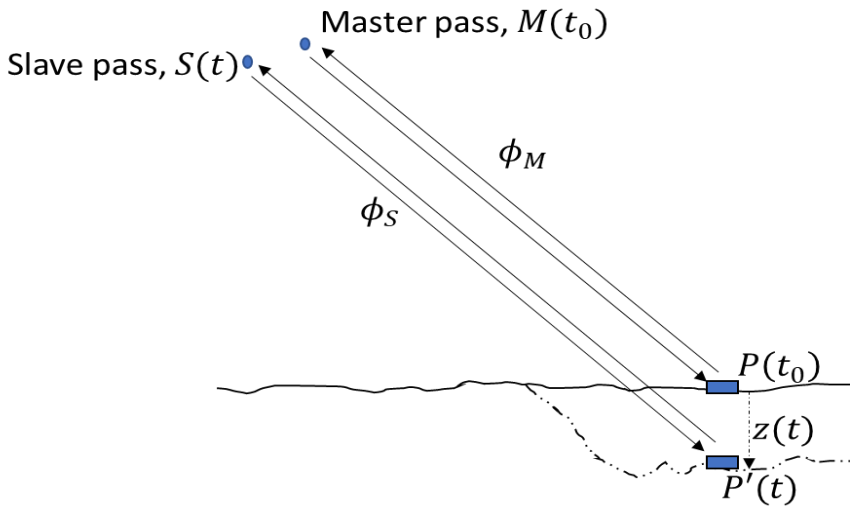

Figure 2-4: The principle of DInSAR

Therefore, we see that with two passes (i.e., two SAR images of the observed scene), we can generate topographic maps using InSAR. When a third flight is combined with these passes, we can now perform differential interferometry. Table 2-1 below summarizes the differences between InSAR and DInSAR.

Table 2-1: Summary and comparison of InSAR and DInSAR [22]

InSAR	DInSAR
Application: Digital Elevation Maps (DEM)	Application: Displacement Maps
Preferably simultaneous acquisitions	Acquisitions that span the event to be studied in time
Accuracy in the order of meters	Relative accuracy in the order of millimeters
Perpendicular baseline must be large	Perpendicular baseline should be small
Sensitivity: $\mathrm{k_z} = -\frac{4\pi}{\lambda}\frac{B_\perp z}{\rho \sin\theta_i}$	Sensitivity: $\mathrm{k}_\phi = -\frac{4\pi}{\lambda}$ $\mathrm{k}_v = -\frac{4\pi}{\lambda}\Delta t$

2.5 Direction of Arrival Estimation

Direction of arrival (DOA) estimation in radar uses signal processing to pinpoint the signal scattering's angle of arrival relative to the sensor. DOA estimation requires a signal model relating the positions of the sources or scatterers to the sensor array measurements. For this research, an arbitrary planar array is assumed, as shown in Figure 2-5, where the angle θ_q is the direction of arrival of a single source.

2.5.1 Signal model for DOA estimation

Consider an arbitrary antenna array with a collection of P elements in a two-dimensional plane with respect to a reference point that will serve as the origin for the array that is near the center or centroid of the elements. Figure 2-5 illustrates this arbitrary planar array configuration. We assume Q sources or targets that are uncorrelated. We also assume the sources to be narrowband. We do not make the far-field assumption [23].

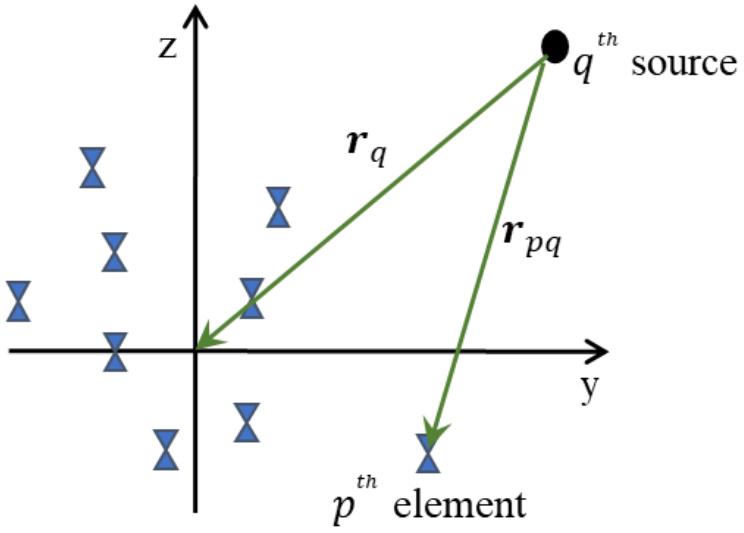

Figure 2-5: Arbitrary planar array configuration

The sensors will receive the same signal but at marginally different time instants. Let the signal measured at a reference point be denoted by $s(\tau)$ and $\Delta\tau_p$denote the relative difference in the signal propagation between the reference point and the p^{th} sensor, then the received signal at the p^{th} sensor can be written as;

$$x_p(\tau) = s\big(\tau - \Delta\tau_p\big) + n_p(\tau), \tag{2.13}$$

where $n_p(\tau)$ is additive noise.

From the geometry of Figure 2-5, we can write the extra distance traveled by the signal to each sensor relative to the centroid as;

$$d_p = |\boldsymbol{r}_{pq}| - |\boldsymbol{r}_q|, \tag{2.14}$$

where $\boldsymbol{r}_q$ is the range of the q^{th} source and $\boldsymbol{r}_{pq}$ is the distance from q^{th} source to p^{th}element of the receiver.

The corresponding delay in time is obtained by dividing this extra distance by the speed of propagation;

$$\Delta\tau_p = \frac{r_{pq} - r_q}{c}, \qquad \text{for } p = 1,2,\ldots\ldots,P \tag{2.15}$$

where c is the speed of propagation.

By combining Equations 2.13 and 2.15, we get the model for a single source [23]:

$$x_p(\tau) = s\left(\tau - \frac{r_{pq} - r_q}{c}\right) + n_p(\tau). \tag{2.16}$$

This model is valid for both wideband and narrowband cases.

2.5.2 Narrowband Signal Model

For narrowband arrays with center frequency ω_c, the domain of possible values for $\Delta\tau$ is small enough that the signal envelope stays relatively constant over the array, and the signal delayed by $\Delta\tau$ can be approximated by [24]:

$$s(\tau - \Delta\tau) \approx s(\tau)e^{-j\omega_c\Delta\tau}, \tag{2.17}$$

where $s(\tau) = \alpha e^{j\omega_c\tau}e^{j\phi(\tau)}$ is the modulated signal, α is the amplitude, and ϕ the phase of the signal. Using Equation 2.16 in 2.13 yields

$$x_p(\tau) = s(\tau)e^{-j\omega_c\Delta\tau_p} + n_p(\tau). \tag{2.18}$$

By combining this for all sensors into a vector, we get

$$\begin{bmatrix} x_1(\tau) \\ x_2(\tau) \\ \vdots \\ x_P(\tau) \end{bmatrix} = \begin{bmatrix} e^{-j\omega_c\Delta\tau_1} \\ e^{-j\omega_c\Delta\tau_2} \\ \vdots \\ e^{-j\omega_c\Delta\tau_P} \end{bmatrix} s(\tau) + \begin{bmatrix} n_1(\tau) \\ n_2(\tau) \\ \vdots \\ n_P(\tau) \end{bmatrix}. \tag{2.19}$$

This can be written in vector form as

$$\boldsymbol{x}(\tau) = \boldsymbol{a}(\theta, \omega_c)s(\tau) + \boldsymbol{n}(\tau). \tag{2.20}$$

The vector $\boldsymbol{a}(\theta, \omega_c) = \begin{bmatrix} e^{-j\omega_c\Delta\tau_1} & e^{-j\omega_c\Delta\tau_2} & \dots & e^{-j\omega_c\Delta\tau_P} \end{bmatrix}^T$ is known as the *steering vector*. Equation 2.19 (and 2.20) is the DOA estimation model for a narrowband source signal.

2.5.3 Wideband Signal Model

For wideband signals, the steering vector depends on the frequency since the signal can no longer be assumed to remain constant across the whole array, as we did with the narrowband case. To formulate the wideband signal model, we need to decompose the wideband signals into several narrowband signals using a filter bank. The received signal is a superposition of signals from multiple sources that simultaneously impinge on the sensor array. For Q sources and the

narrowband component $s_q(m,\omega_k)$ associated with the center frequency ω_k of the q^{th} source at snapshot index m, we can write Equation 2.19 as

$$\begin{bmatrix} x_1(m,\omega_k) \\ x_2(m,\omega_k) \\ \vdots \\ x_P(m,\omega_k) \end{bmatrix} = \begin{bmatrix} \boldsymbol{a}(\theta_1,\omega_k) & \boldsymbol{a}(\theta_2,\omega_k) & \cdots & \boldsymbol{a}(\theta_Q,\omega_k) \end{bmatrix} \begin{bmatrix} s_1(m,\omega_k) \\ s_2(m,\omega_k) \\ \vdots \\ s_Q(m,\omega_k) \end{bmatrix} + \begin{bmatrix} n_1(m,\omega_k) \\ n_2(m,\omega_k) \\ \vdots \\ n_P(m,\omega_k) \end{bmatrix}, \quad 2.21$$

This can be written using matrix operations as:

$$\boldsymbol{x}(m,\omega_k) = \boldsymbol{A}(\omega_k)\boldsymbol{s}(m,\omega_k) + \boldsymbol{n}(m,\omega_k), \qquad m = 1,\dots,M \text{ and } k = 1,\dots,K. \quad 2.22$$

Since the steering vectors don't depend on m, we write a single matrix expression for all snapshots as:

$$\boldsymbol{X}(\omega_k) = \boldsymbol{A}(\omega_k)\boldsymbol{S}(\omega_k) + \boldsymbol{N}(\omega_k), \qquad k = 1,\dots,K \quad 2.23$$

where $\boldsymbol{X}$ is $P \times M$, $\boldsymbol{A}$ is $P \times Q$, $\boldsymbol{S}$ is $Q \times M$, $\boldsymbol{N}$ is $P \times M$, and $Q < P$. Each of the M columns of the matrices corresponds to a separate snapshot.

2.5.4 Narrowband DOA Methods

Just as the narrowband signal model is fundamental in developing the wideband signal model, similarly, the narrowband DOA methods are vital parts of wideband DOA estimation. A few narrowband DOA estimation methods will be highlighted here for the completeness of this report.

2.5.4.1 Spatial Filtering

Spatial filtering, which is analogous to convolution in the time domain, involves receiving the signal at the sensors and multiplying by filter coefficients and the directions where the power estimate peaks define the DOA estimates. The condition for receiving the signal from one direction of interest θ_q with no attenuation is the constrain that $\boldsymbol{w}^H\boldsymbol{a}(\theta_q) = 1$, where $\boldsymbol{w}$ is the filter. The filter receives signals from that direction while attenuating all other directions. The condition for

canceling all other directions is $\boldsymbol{w}^H\boldsymbol{a}(\theta) \approx 0$ for $\theta \neq \theta_q$. The received signal from different sensors, represented by vector $\boldsymbol{x}(m, \omega_k)$, is filtered with $\boldsymbol{w}$ to obtain

$$x_{filtered}(\omega_k) = \boldsymbol{w}^H\boldsymbol{x}(m, \omega_k). \quad 2.24$$

The spectrum estimate when $\boldsymbol{w}$ has been designed for θ_q is given by

$$S(\theta_q) = \boldsymbol{w}^H(\theta_q)\widehat{\boldsymbol{R}}\boldsymbol{w}(\theta_q), \quad 2.25$$

where $\widehat{\boldsymbol{R}} = \frac{1}{M}\sum_{m=1}^{M}\boldsymbol{x}(m, \omega_k)\boldsymbol{x}^H(m, \omega_k)$ is the estimated covariance matrix.

Beamformer: This is the most basic spatial filtering estimation method, which seeks to minimize $\boldsymbol{w}^H\boldsymbol{w}$ subject to $\boldsymbol{w}^H\boldsymbol{a}(\theta) = 1$, when $\boldsymbol{w}$ is independent of the data. The solution to this optimization problem is

$$\boldsymbol{w} = \frac{\boldsymbol{a}(\theta)}{\boldsymbol{a}^H(\theta)\boldsymbol{a}(\theta)} = \frac{\boldsymbol{a}(\theta)}{P}, \quad 2.26$$

where P is the number of variables in $\boldsymbol{w}$. Inserting Equation 2.26 into 2.25 yields the spectral estimate:

$$S(\theta) = \frac{\boldsymbol{a}^H(\theta)\widehat{\boldsymbol{R}}\boldsymbol{a}(\theta)}{P^2}. \quad 2.27$$

Minimum Variance Distortionless Response (MVDR): Also known as the Capon method, MVDR involves designing a filter $\boldsymbol{w}$ such that the overall power of the signal $\left(E\left[\left|x_{filtered}\right|^2\right]\right)$ is minimized subject to receiving a signal from one direction undistorted, i.e., to minimize $\left(E\left[\left|x_{filtered}\right|^2\right]\right)$ subject to $\boldsymbol{w}^H\boldsymbol{a}(\theta) = 1$. Using the Lagrange multiplier technique to handle the constrained optimization, the solution to this optimization problem is;

$$\boldsymbol{w} = \frac{\widehat{\boldsymbol{R}}^{-1}\boldsymbol{a}(\theta)}{\boldsymbol{a}^H(\theta)\widehat{\boldsymbol{R}}^{-1}\boldsymbol{a}(\theta)}. \quad 2.28$$

And using Equation 2.25, we get the spectral estimate as:

$$S(\theta) = \frac{1}{\boldsymbol{a}^H(\theta)\widehat{\boldsymbol{R}}^{-1}\boldsymbol{a}(\theta)}. \quad 2.29$$

When the estimated covariance matrix is accurate enough, MVDR resolves sources better than the beamformer because of the data dependency of the optimization problem.

2.5.4.2 Parametric Methods

Parametric methods assume a model for the signal and estimate the parameters of the model. Usually, this is the assumption that the signal is a linear composition of complex exponentials. Examples of parametric methods include ESPRIT, MUSIC, and MLE, but we shall only expound on the MUSIC and MLE algorithms.

MUltiple SIgnal Classification (MUSIC)[25]*:* MUSIC breaks the signal into noise and signal subspaces by applying eigenvalue decomposition to the covariance matrix ($\boldsymbol{R}$) of the measurements and generates a pseudospectrum that peaks very sharply around the true angles. Using the signal model in Equation 2.22, the covariance matrix can be expressed as:

$$\boldsymbol{R} = \mathrm{E}[\boldsymbol{x}\boldsymbol{x}^H] = \mathrm{E}[(\boldsymbol{A}\boldsymbol{s}+\boldsymbol{n})(\boldsymbol{A}\boldsymbol{s}+\boldsymbol{n})^H)] = \mathrm{E}[\boldsymbol{A}\boldsymbol{s}\boldsymbol{s}^H\boldsymbol{A} + \boldsymbol{A}\boldsymbol{s}\boldsymbol{n}^H + \boldsymbol{n}\boldsymbol{s}^H\boldsymbol{A}^H + \boldsymbol{n}\boldsymbol{n}^H] \quad 2.30$$

$$= \boldsymbol{A}\mathrm{E}[\boldsymbol{s}\boldsymbol{s}^H]\boldsymbol{A}^H + \boldsymbol{A}\mathrm{E}[\boldsymbol{s}\boldsymbol{n}^H] + \mathrm{E}[\boldsymbol{n}\boldsymbol{s}^H]\boldsymbol{A}^H + \mathrm{E}[\boldsymbol{n}\boldsymbol{n}^H]\,.$$

Denoting the $Q \times Q$ source covariance matrix with $\boldsymbol{R}_s$ and noise covariance with $\boldsymbol{N}_c$, we can write;

$$\boldsymbol{R} = \boldsymbol{A}\boldsymbol{R}_s\boldsymbol{A}^H + \boldsymbol{N}_c, \quad 2.31$$

since the noise and the source signals are not correlated. By assuming that the noise is complex white noise, $\boldsymbol{N}_c$ is simplified to $\sigma_{n,k}^2\boldsymbol{I}$.

$$\boldsymbol{R}(\omega_k) = \boldsymbol{A}(\omega_k)\boldsymbol{R}_s(\omega_k)\boldsymbol{A}^H(\omega_k) + \sigma_{e,k}^2\boldsymbol{I}. \quad 2.32$$

The rank of $\boldsymbol{AR_sA^H}$ needs to be equal to the number of sources Q. $\boldsymbol{AR_sA^H}$ is positive semidefinite with Q non-zero eigenvalues and $P - Q$ eigenvalues equal to zero. The eigenvalue decomposition (EVD) of $\boldsymbol{R}$ has the eigenvectors in $\boldsymbol{U}$ and eigenvalues[1] on the diagonal of $\boldsymbol{V}$:

$$\boldsymbol{R} = \boldsymbol{UVU^{-1}}. \tag{2.33}$$

$\boldsymbol{U}$ can be split into two parts: $\boldsymbol{U_S}$ has the Q first eigenvectors corresponding to the eigenvalues $\lambda_1, \lambda_2 \cdots \lambda_Q$ and $\boldsymbol{U_N}$ holds the rest of the eigenvectors corresponding to the eigenvalues $\lambda_{Q+1}, \lambda_{Q+2} \cdots \lambda_P$. $\boldsymbol{U_S}$ is known as the signal subspace and $\boldsymbol{U_N}$ as the noise subspace.

From the definition of eigenvalues and the positive semidefinite properties of the two components of $\boldsymbol{R}$;

$$\boldsymbol{RU_N} = \boldsymbol{U_N}\begin{bmatrix}\lambda_{Q+1} & 0 & 0\\ 0 & \cdots & \vdots\\ 0 & 0 & \lambda_P\end{bmatrix} = \boldsymbol{U_N}\begin{bmatrix}\sigma_n^2 & 0 & 0\\ 0 & \cdots & 0\\ 0 & 0 & \sigma_n^2\end{bmatrix} = \sigma_n^2\boldsymbol{U_N}. \tag{2.34}$$

But also, from Equation 2.33,

$$\boldsymbol{RU_N} = \boldsymbol{AR_sA^HU_N} + \sigma_n^2\boldsymbol{U_N}. \tag{2.35}$$

Such that;

$$\boldsymbol{RU_N} = \boldsymbol{AR_sA^HU_N} + \boldsymbol{RU_N} \Longrightarrow \boldsymbol{AR_sA^HU_N} = 0. \tag{2.36}$$

Since the steering vectors are linearly independent, $\boldsymbol{AR_s}$ has full rank, implying that;

$$\boldsymbol{A^HU_N} = 0. \tag{2.37}$$

[1] It is assumed that the eigenvalues are sorted in descending order i.e., $\lambda_1 \geq \lambda_2 \geq \cdots \geq \lambda_P$.

The true angles of the sources $\theta_1, \ldots\ldots, \theta_Q$ satisfy $\boldsymbol{a}(\theta_q)\boldsymbol{U}_N\boldsymbol{U}_N^H\boldsymbol{a}^H(\theta_q) = 0$, and the MUSIC pseudo-spectrum peaks very sharply around the true angles when using the estimated covariance matrix to obtain $\boldsymbol{U}_N$ and is given by;

$$S(\theta) = \frac{1}{\boldsymbol{a}(\theta)\boldsymbol{U}_N\boldsymbol{U}_N^H\boldsymbol{a}^H(\theta)}. \tag{2.38}$$

MUSIC requires a decision for the number of sources Q prior to performing the final spectrum estimation. This decision can have a major impact on the result. Sravya et al and Mohanad et al discussed model order estimation to estimate Q in [26] and [27]. Assuming the white noise model for the covariance matrix of the noise, the Minimum Description Length (MDL) criterion [28] can be used to detect the number of sources using Equation 2.39.

$$MDL(q) = -\log\left(\left(\frac{\prod_{d=q+1}^{P}\lambda_d^{(1/P-q)}}{\frac{1}{P-q}\sum_{d=q+1}^{P}\lambda_d}\right)^{(N-q)M}\right) + \frac{1}{2}q(2P-q)\log M \tag{2.39}$$

The minimum of the MDL criterion gives the estimate of the number of sources:

$$\hat{Q} = \arg\min_{q=1,2,\ldots,P} MDL(q). \tag{2.40}$$

It should be noted that the number of sources $\hat{Q}$ for coherent methods can also be estimated using the Akaike Information Criterion (AIC) [29];

$$AIC(q) = (P-q)M\log\left(\frac{\frac{1}{P-q}\sum_{d=q+1}^{P}\lambda_d}{\left(\prod_{d=q+1}^{P}\lambda_d\right)^{1/(P-q)}}\right) + q(2P-q), \tag{2.41}$$

such that;

$$\hat{Q} = \arg \min_{q=1,2,\ldots,P} AIC(q). \tag{2.42}$$

Maximum Likelihood Estimator (MLE): DOA estimation using MLE tries to maximize the likelihood function that the received signals came from a particular set of angles (θ). By assuming that the noise $\boldsymbol{n}(t)$ is a stationary, ergodic, and Gaussian process of zero mean and variance $\sigma^2\boldsymbol{I}$ with statistically independent samples, we can write the joint density function of the sampled data as:

$$f(\boldsymbol{X}) = \prod_{m=1}^{M} \frac{1}{\pi \det[\sigma^2\boldsymbol{I}]} \exp\left(-\frac{1}{\sigma^2}|\boldsymbol{x}(m,\omega_k) - \boldsymbol{A}(\theta)\boldsymbol{s}(m,\omega_k)|^2\right). \tag{2.43}$$

The log likelihood function is given by

$$\boldsymbol{L}(\theta) = -MP\log\sigma^2 - \frac{1}{\sigma^2}\sum_{m=1}^{M}|\boldsymbol{x}(m,\omega_k) - \boldsymbol{A}(\theta)\boldsymbol{s}(m,\omega_k)|^2, \tag{2.44}$$

with constant terms disregarded.

We can further write the log-likelihood function as

$$\boldsymbol{L}(\theta) = \sum_{m=1}^{M}\left|\boldsymbol{P}_{\boldsymbol{A}(\theta)}\boldsymbol{x}(m,\omega_k)\right|^2 = \mathrm{Tr}(\boldsymbol{P}_{\boldsymbol{A}(\theta)}\boldsymbol{R}), \tag{2.45}$$

where, $\boldsymbol{P}_{\boldsymbol{A}(\theta)} = \boldsymbol{A}(\theta)\left(\boldsymbol{A}^H(\theta)\boldsymbol{A}(\theta)\right)^{-1}\boldsymbol{A}^H(\theta)$ is the projection of the steering matrix.

For deterministic MLE, the maximum likelihood estimate is found by maximizing the deterministic cost function below, assuming that the noise variance and target signal are unknown but non-random [30];

$$\boldsymbol{J}_{MLE} = \mathrm{Tr}\left(\boldsymbol{P}_{\boldsymbol{A}(\theta)}\boldsymbol{R}\right), \tag{2.46}$$

MLE seeks to maximize the cost function, J_{MLE} such that;

$$\theta = \arg\max_{\theta}(\boldsymbol{J}_{MLE}). \quad 2.47$$

2.5.5 Wideband Methods

In this section, wideband methods that are frequently encountered in signal processing are discussed. The wideband spectrum estimate S is evaluated at grid points denoted by ϑ_g while using a subset of the sub-bands denoted by κ. The reasoning behind the use of a subset of the sub-bands is that the low and high-frequency sub-bands are often susceptible to low signal-to-noise ratio and aliasing. Wideband methods can broadly be categorized as incoherent, coherent, or sparse. Sparse methods, which are generally formed around l_1-optimization, for example l_1-SVD, are not discussed here. Note that the maximum likelihood estimator method extends to wideband processing, too, and does not fall into the above categories [31].

2.5.5.1 Incoherent Wideband Methods

The incoherent methods are based on incoherently averaging narrowband results. They utilize narrowband methods for each sub-band ω_k independently and then combine these independent estimates that are denoted by S_k. The wideband spectrum estimate S is the summation of the sub-band spectra. Summation-based MVDR (MVDR-S) and summation-based MUSIC (MUSIC-S) are examples of incoherent wideband DOA methods whose algorithms are presented below. The measurements are represented by $\boldsymbol{X}_k$ and the angle grid by $\vartheta_1, \ldots, \vartheta_G$

Summation-based MVDR (MVDR-S): For each k^{th} sub-band (where $k \in \kappa$), the covariance matrix $\widehat{\boldsymbol{R}}_k$ is estimated as $\widehat{\boldsymbol{R}}_k = \frac{1}{M}\boldsymbol{X}_k\boldsymbol{X}_k^H$, and for each of G grid points, a corresponding narrowband spectrum estimate S_k is processed as $S_k(\vartheta_g) = \frac{1}{\boldsymbol{a}^H(\vartheta_g)\widehat{\boldsymbol{R}}_k^{-1}\boldsymbol{a}(\vartheta_g)}$. Then the wideband spectrum estimate S is the summation of the sub-band spectra estimates:

$$S(\vartheta_g) = \sum_{k\in\kappa} S_k(\vartheta_g). \qquad 2.48$$

Summation-based MUSIC (MUSIC-S) [25]*:* For each k^{th} sub-band (where $k \in \kappa$), the following are done:

- The covariance matrix is estimated as: $\widehat{\boldsymbol{R}}_k = \frac{1}{M}\boldsymbol{X}_k\boldsymbol{X}_k^H$.
- The EVD of $\widehat{\boldsymbol{R}}(\omega_k)$ is calculated as: $\widehat{\boldsymbol{R}}(\omega_k) = \widehat{\boldsymbol{U}}(\omega_k)\widehat{\boldsymbol{V}}(\omega_k)\widehat{\boldsymbol{U}}^{-1}(\omega_k)$.
- The number of sources $\hat{Q}_k$ is estimated using Equation 2.40.
- The matrix $\widehat{\boldsymbol{U}}_N(\omega_k)$ is obtained, that contains eigenvectors of $\widehat{\boldsymbol{U}}(\omega_k)$ corresponding to the $P - \hat{Q}_k$ smallest eigenvalues.

Like with the MVDR-S algorithm above, for each of G grid points, a corresponding narrowband spectrum estimate S_k is processed as $S_k(\vartheta_g) = \frac{1}{\boldsymbol{a}^H(\vartheta_g,\omega_k)\widehat{\boldsymbol{U}}_N(\omega_k)\widehat{\boldsymbol{U}}_N^H(\omega_k)\boldsymbol{a}(\vartheta_g,\omega_k)}$. Then the wideband spectrum estimate S is the summation of the sub-band spectra estimates:

$$S(\vartheta_g) = \sum_{k\in\kappa} S_k(\vartheta_g). \qquad 2.49$$

2.5.5.2 Coherent Wideband Methods

The coherent methods transform the sub-bands to a single reference frequency (generally the center frequency) so that narrowband methods can be applied. This contrasts with the previously discussed incoherent methods that combine the individual DOA estimates from different sub-bands by summing the individual outputs. The Coherent Signal-Subspace Method (CSSM) algorithm that Wang introduced and Kaveh [29] performs the DOA estimation based on a single covariance matrix, the universal spatial covariance matrix (USCM), that characterizes the wideband signal. For the single reference frequency ω_0 that is representative of the wideband signal; we can write the narrowband signal model (Equation 2.32) as:

$$\boldsymbol{R}(\omega_k) = \boldsymbol{A}(\omega_0)\boldsymbol{R}_s(\omega_0)\boldsymbol{A}^H(\omega_0) + \sigma_{n,0}^2\boldsymbol{I}. \quad 2.50$$

We can then apply a subspace method like MUSIC to this model. The proceeding section demonstrates that these transformed sub-bands approximate the narrowband signal model. The method for estimating the transformation is discussed in chapter 4.

Coherent methods are based on the idea that a steering matrix $\boldsymbol{A}(\omega_k)$ can be transformed into another steering matrix $\boldsymbol{A}(\omega_0)$ at the reference frequency ω_0 by using an $P \times P$ transformation matrix

$$\boldsymbol{T}(\omega_k)\boldsymbol{A}(\omega_k) = \boldsymbol{A}(\omega_0). \quad 2.51$$

This matrix is called a *focusing matrix* [29]. The measurements are transformed by this matrix:

$$\boldsymbol{Y}_t(\omega_k) = \boldsymbol{T}(\omega_k)\boldsymbol{X}(\omega_k). \quad 2.52$$

Using Equation 2.52, the covariance of the transformed measurements then becomes

$$\boldsymbol{R}_t(\omega_k) = \sum_{k\in\kappa} \mathrm{E}[\boldsymbol{X}_t(\omega_k)\boldsymbol{X}_t(\omega_k)^H] = \sum_{k\in\kappa} \mathrm{E}[\boldsymbol{T}(\omega_k)\boldsymbol{X}(\omega_k)\boldsymbol{T}(\omega_k)^H\boldsymbol{X}(\omega_k)^H] \quad 2.53$$

$$= \sum_{k\in\kappa} \boldsymbol{T}(\omega_k)\boldsymbol{R}(\omega_k)\boldsymbol{T}(\omega_k)^H.$$

When Equation 2.53 is used in Equation 2.32 to substitute for $\boldsymbol{R}(\omega_k)$ while using the statement of Equation 2.51, we get

$$\sum_{k\in\kappa} \boldsymbol{T}(\omega_k)\boldsymbol{R}(\omega_k)\boldsymbol{T}(\omega_k)^H = \sum_{k\in\kappa} \boldsymbol{T}(\omega_k)\boldsymbol{A}(\omega_k)\boldsymbol{R}_s(\omega_k)\big(\boldsymbol{T}(\omega_k)\boldsymbol{A}(\omega_k)\big)^H + \sigma_k^2\boldsymbol{T}(\omega_k)\boldsymbol{T}(\omega_k)^H$$

$$= \sum_{k\in\kappa} \boldsymbol{A}(\omega_0)\boldsymbol{R}_s(\omega_k)\boldsymbol{A}(\omega_0)^H + \sigma_{n,k}^2\boldsymbol{T}(\omega_k)\boldsymbol{T}(\omega_k)^H.$$

For Unitary transformation matrices, this simplifies to

$$\sum_{k\in\kappa} \boldsymbol{T}(\omega_k)\boldsymbol{R}(\omega_k)\boldsymbol{T}(\omega_k)^H = \boldsymbol{A}(\omega_0)\sum_{k\in\kappa} \boldsymbol{R}_s(\omega_k)\boldsymbol{A}(\omega_0)^H + K\sum_{k\in\kappa}\big(\sigma_{n,k}^2\big)\boldsymbol{I}\,. \quad 2.54$$

By denoting $\boldsymbol{R}_s(\omega_0) = \sum_{k\in\kappa} \boldsymbol{R}_s(\omega_k)$, $\sigma_{n,0}^2 = K\sum_{k\in\kappa}\sigma_{n,k}^2$, and $\boldsymbol{R}(\omega_0) = \sum_{k\in\kappa} \boldsymbol{T}(\omega_k)\boldsymbol{R}(\omega_k)\boldsymbol{T}(\omega_k)^H$, Equation 2.54 becomes similar to Equation 2.50 and hence concludes the proof. A subspace method such as MUSIC is now applicable to the estimate $\widehat{\boldsymbol{R}}(\omega_0) = \sum_{k\in\kappa} \boldsymbol{T}(\omega_k)\widehat{\boldsymbol{R}}(\omega_k)\boldsymbol{T}(\omega_k)^H$, from which the wideband spectrum can be obtained. MUSIC would require a decision for the number of sources Q in order to performing the final spectrum estimation and this is achieved by using the model order estimation methods shown in section 2.5.4.2 (Equations 2.41 and 2.39).

2.5.5.3 Wideband Maximum Likelihood Estimator

To extend the MLE discussed in section 2.5.4.2 to the wideband case, the signal bandwidth is subdivided into K sub-bands and the narrowband MLE is applied to the combined likelihood function, which is the summation of all the individual likelihood functions assuming the sub-bands are independent[31]. The wideband MLE cost function then becomes;

$$\boldsymbol{J}_{WMLE} = \sum_{k=1}^{K} \boldsymbol{J}_{MLE}(\omega_k), \tag{2.55}$$

where $J_{MLE}(\omega_k)$ is the narrowband MLE cost function at frequency ω_k.

Wideband MLE maximizes the cost function such that;

$$\theta = \arg\max_{\theta}(\boldsymbol{J}_{WMLE}). \tag{2.56}$$

2.6 SAR Processing for Layered Media

The dielectric properties of ice sheets are depth-dependent. This is due to variations in the density and chemistry of the ice, as well as the presence of impurities such as dust and air bubbles. The dielectric properties of the ice are typically estimated using a model that assumes the ice is a layered media with variation in the z-axis (vertical) only.

Range Doppler Algorithm (RDA) and Chirp Scaling Algorithm are signal processing techniques commonly used in radar imaging and remote sensing applications. However, in wideband scenarios, these algorithms cannot be applied reliably. In wideband scenarios, F-k migration (ω_k algorithm (WKA)) is more reliable.

The RDA algorithm employs a two-dimensional Fourier transform to convert the raw radar data from the time domain to the range-Doppler domain. The algorithm then applies filtering and thresholding to suppress noise and clutter and enhance the target signals.

The Chirp Scaling Algorithm employs a time-domain scaling operation to transform the signal from the received domain to the transmitted domain, where it can be processed more efficiently.

The F-k migration algorithm is based on the principle of wave propagation and is used to compensate for the effect of phase delays that arise due to variations in the radar antenna position. The F-k migration algorithm applies a two-dimensional Fourier transform. This transformation converts the data from the space-time domain to the frequency-wavenumber domain, where phase delays can be more easily identified and corrected. The algorithm then applies a phase correction to the data and performs an inverse Fourier transform to produce the final high-resolution image of the target scene [32].

F-k migration is based on the exploding source model [33] and the scalar wave equation:

$$\Psi = e^{-j\boldsymbol{k}^T\boldsymbol{R}+j\omega t} \qquad 2.57$$

where Ψ is the wave function, that represents the amplitude and phase of the wave at a given point in space and time. $\boldsymbol{k}$ is the wavenumber vector, which describes the direction and magnitude of the wave's propagation in space. $\boldsymbol{R}$ is the position vector, which describes the location of the point in space where the wave function is being evaluated. ω is the angular frequency, and t is time.

The rectangular components of the wavenumber vector obey the separation equation;

$$k_x^2 + k_y^2 + k_z^2 = k^2 = \omega^2/v_m^2 \qquad 2.58$$

where v_m is the phase velocity, and k_x, k_y, and k_z are the rectangular components of the wavenumber vector in the x, y, and z axis.

2.6.1 F-K Migration Algorithm

The first step in the F-K migration algorithm is to transform the SAR signal data from the time domain to the frequency domain using a two-dimensional fast Fourier transform (FFT).

In the next step, a reference function is computed for a selected range, usually the mid-swath range. This reference function is then multiplied by the frequency-domain data to apply both range and azimuth compression (reference frequency multiply (RFM)). The targets at the reference range are correctly focused, but targets away from that range are only partially focused.

The next step in the F-K migration algorithm is to use Stolt interpolation to focus the remainder of the targets that were not fully focused by the RFM step. Stolt interpolation is a form of frequency-wavenumber (F-k) migration that uses linear interpolation to adjust the wave numbers of the signal data in the frequency domain.

The final step in the F-k migration algorithm is to transform the data back to the space-time domain using a two-dimensional inverse fast Fourier transform (IFFT). This step generates the final image in the SAR image domain, which is a focused representation of the subsurface targets [32].

Figure 2-6 summarizes the process flow for the F-k migration algorithm.

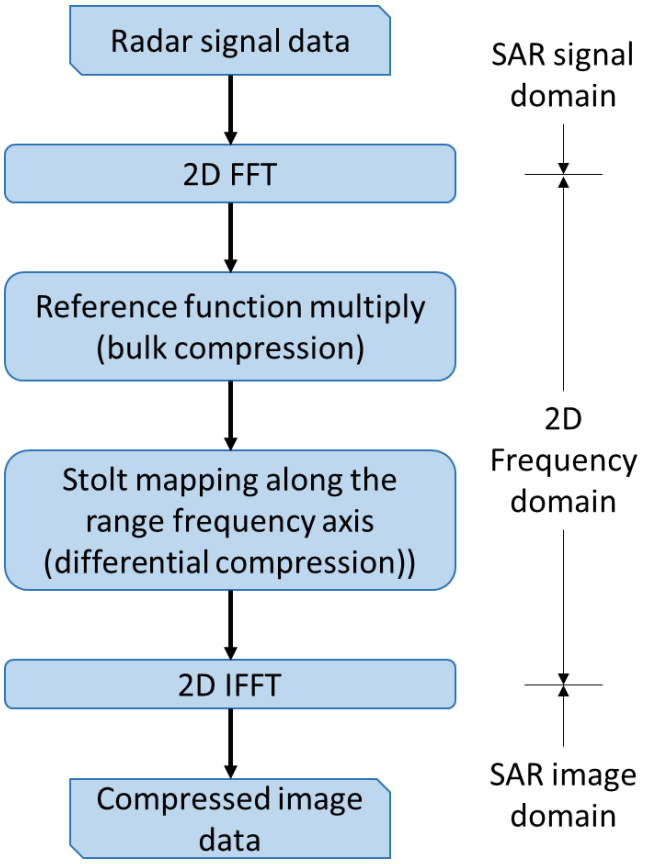

Figure 2-6: The F-k migration algorithm [32]

2.6.2 Uniform Dielectric Half-space Model

The uniform dielectric half-space model assumes that the subsurface consists of a uniform, homogeneous layer of a single dielectric material that extends to infinity in the horizontal direction. This model is often used as a first-order approximation of the subsurface. In the uniform dielectric half-space model, the subsurface is assumed to be characterized by two parameters: the permittivity and the conductivity of the material. The permittivity is a measure of how much the material can store electric charge, while the conductivity is a measure of how well the material conducts electricity. These parameters affect the way in which electromagnetic waves propagate through the subsurface and are used to model the reflection and transmission of these waves. While

the uniform dielectric half-space model is a useful approximation of the subsurface in some applications, it may not be accurate for more complex subsurface structures. In such cases, more sophisticated models, such as the layered subsurface model, may be necessary to accurately represent the subsurface and interpret the GPR data [34].

2.6.3 F-K Migration for Layered Media

F-K migration for layered media involves extrapolating the wavefield through each layer individually by applying a phase shift to the wavefield at each depth within the layer [35].

For an image $I(x,z)$ of the exploding sources, a wave field $p(t,\ x,\ z)$ is computed when the imaging condition is to set $t\ =\ 0$, such that;

$$I(x,\ z)\ =\ p(t=\ 0, x\, z,\ ). \tag{2.59}$$

The field in time-space coordinates under this condition in equation (2.59) becomes:

$$I(x, Z+\Delta z) = \iint_{-\infty}^{+\infty} P(\omega, k_x, Z) e^{jk_z \Delta z} e^{jk_x x} \mathrm{d}k_x \mathrm{d}\omega \tag{2.60}$$

where $P(\omega, k_x, Z)$ is the wave field.

Equation (2.60) is iteratively applied to create an image line by line by applying it for all depths, Z + Δz, to be imaged. If we consider $l\ =\ 1,\ 2, \ldots, L$ layers as illustrated in Figure 2-7 and let d_l and c_l denote the thickness and wave velocity of layer l, respectively, then,

$$k_{zl} = -\mathrm{sgn}(\omega)\ \sqrt{\frac{\omega^2}{\hat{c}_l^2} - k_x^2} \tag{2.61}$$

where the effective wave velocity $\hat{c} = c/2$ is used because the exploding reflector model is assumed.

Extrapolation through several layers directly is not possible in a multilayer case, but extrapolation within each layer is still possible;

$$P(\omega, k_x, Z_l + \Delta z) = P(\omega, k_x, Z_l)e^{jk_{zl}\Delta z}\ ,\ \Delta z < d_l \qquad 2.62$$

where $P(\omega,\ k_x, Z_l\ )$ denotes the field at the interface Z_l, and $P(\omega,\ k_x, Z_l$+ Δz) denotes the field at a depth z =Z_l+ Δz.

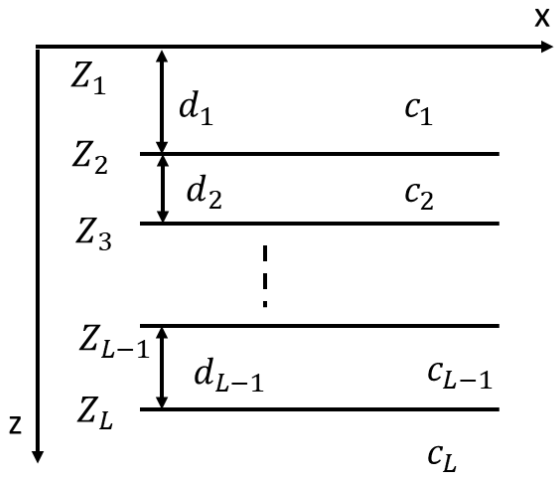

Figure 2-7: Layered media geometry [35] (Credit: Martin H. Skjelvareid et al., 2011)

For layer l, the imaging algorithm can be summarized as follows:

1. The wave field at the top of the layer interface, $P(\omega,\ k_x,\ Z_l)$ is computed.
2. At each depth $Z_l\ +\ \Delta z$ to be imaged within the layer:
    - The wave field is shifted downwards with Δz by multiplying with a phase factor to obtain $P(\omega,\ k_x,\ Z_l\ +\ \Delta z)$, using equation 2.62.
    - An image line $I(x,\ Z_l\ +\ \Delta z)$ is created by integrating with regard to ω and inverse transforming with regard to k_x, according to equation 2.60.

The Stolt interpolation may be adapted to the multilayer case to enable imaging of an entire layer through a single inverse Fourier transform rather than creating an image of each layer line by line.

The traditional F-k migration method involves focusing on a specific reference point or the center of the scene and applying Stolt interpolation to correct the rest of the scene. However, when adapting this method for a dielectric half-space, each row is focused on individually. This means that the IFFT step can be avoided by using summation, which can significantly increase processing speed for multi-layer setups. To achieve this, an additional phase delay is added to the previous result without having to re-compute the previous rows. This is because each subsequent row has the same information as the previous rows, but with a slightly more updated perspective. Following this process can reduce the need for time-consuming steps, resulting in faster and more efficient processing [36].

2.6.4 CReSIS RDS Data Processing

The Radar Depth Sounder (RDS) processing steps are described by [37]. The processing steps for involve converting quantization to voltage, removing DC-bias, applying channel compensation, and pulse compression. The SAR processing involves applying an along-track spatial frequency window and finding the location of the ice surface using a fully automated approach. The channel combination combines channels within a sub-array, followed by multi-looking and spatial averaging. The primary error sources for ice-penetrating radar data are electronic system noise, multiples, and off-nadir reflections. The echogram is used to track ice surface and ice bottom reflections, which is usually done manually. The antenna beam structure and data processing are designed to reduce off-nadir reflected energy sources.

3 MULTIPASS INTERFEROMETRY

3.1 Introduction

This chapter examines the utilization of Multipass (DInSAR) methods on data obtained from the Multichannel Coherent Radar Depth Sounder (MCoRDS). These techniques allow us to assess the vertical movement of layers within the ice sheet located beneath the surface of an ice sheet [36]. The cartoon in Figure 3-1 illustrates the dynamics involved in multipass interferometry. Here we have two passes imaging the ice sheet below. The accumulation rate is a measure of snowfall, and in steady state, it equals the surface velocity of the ice sheet. For airborne systems, there exists a baseline between the passes since the aircraft cannot easily retrace the same trajectory for each pass.

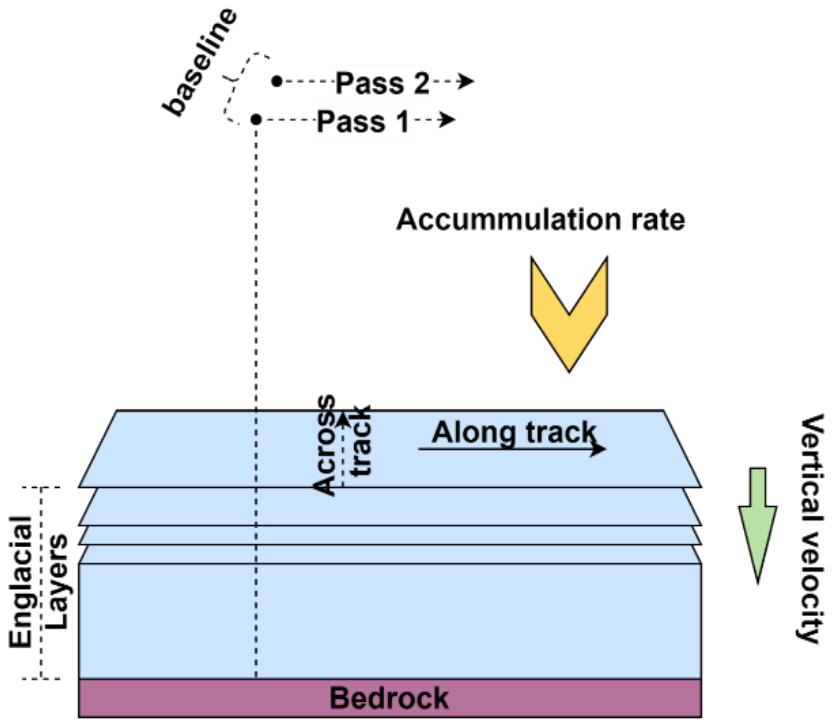

Figure 3-1: Multipass interferometry.

To estimate the vertical displacement accurately, we account for the spatial baseline by incorporating precise trajectory information and determining the cross-track layer slope through the direction of arrival analysis. MCoRDS [7] is a multichannel radar that was developed by the Center for Remote Sensing and Integrated Systems (CReSIS) and has 15 cross-track antenna elements (four on the left wing, seven on the fuselage, and four on the right wing), which are used for array processing [7]. The MCoRDS specifications are shown in Table 3-1 below. Multipass results from flights along the EGIG line and near the Summit camp in Greenland are discussed here [36]. These results illustrate the capabilities of the DInSAR algorithm.

Table 3-1: Typical operating parameters for the MCoRDS radar in the CReSIS instrument package [7].

Parameter	**MCoRDS/I**
Measurement	Bedrock topography, 3D Imaging, Deep internal layering
Center frequency	195 MHz
Bandwidth	30 MHz
Peak transmit power	up to 1200 W
Pulse duration	1 to 30 μs
Pulse repetition frequency (PRF)	< 12 kHz
Operational altitude	500 to 10,000 m
Measurement depth	< 4 km
Vertical resolution	~ 6 m in ice (Twin Otter / NASA P-3) ~ 20 m in ice (NASA DC-8)

3.2 Problem Formulation

Ground-based Autonomous phase-sensitive Radio-Echo Sounder (ApRES) [37] units have been widely utilized to successfully capture point measurements of the vertical velocity field of ice sheets using DInSAR [19]. The spatial baseline is eliminated with ground-based units because the unit can be precisely positioned or even left in place for the required repeat measurements. However, we cannot achieve a zero spatial baseline with airborne systems, leading to displacement measurement errors if the spatial baseline is not adequately accounted for.

The scattering sources for the DInSAR measurements are quasi-specular near-horizontal englacial layers throughout the ice column, as shown in Figure 3-2.

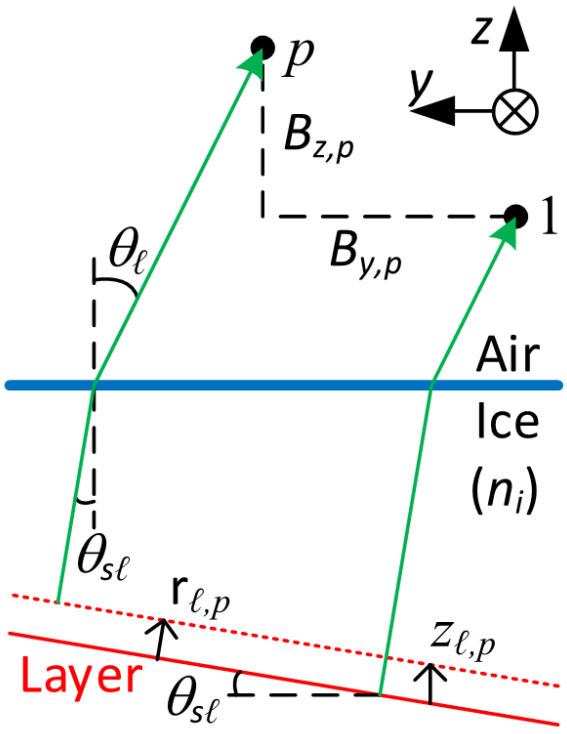

Figure 3-2: Multipass geometry.

The phase difference between two radar passes taken at different times gives an indication of the average vertical velocity of the layer under investigation [36]. If we consider a set of P passes ($p =$

$1, \ldots\ldots, P$), the cross track geometry shown in Figure 3-2 shows that $B_{z,p}$ and $B_{y,p}$ are the z and y coefficients respectively of the p^{th} baseline vector between pass 1 and the p^{th} pass. θ_l is the Direction of Arrival (DoA) of the signal in air, and θ_{sl} is the cross-track slope of the internal layer, l. θ_{sl} is also equal to the DoA within the ice. Using Equation 2.12, which makes use of the plane wave approximation, and subtracting the phase change for pass p from that of pass 1, we get the interferometric phase, ϕ, due to the spatial baseline and layer displacement for pass p relative to pass 1 as

$$\phi = -B_{z,p}k\cos\theta_l + B_{y,p}k\sin\theta_l + r_{l,p}k, \qquad 3.1$$

where $k = \frac{4\pi}{\lambda}$ is the wavenumber in air, λ is the wavelength in air, $\sin\theta_l = n_i \sin\theta_{sl}$, n_i is the refraction index of ice, and $r_{l,p}$ is the range displacement of layer, l. The layer slope is assumed to remain the same over the collection period of the passes.

For simplicity, each element of the antenna array on the aircraft is treated as a separate pass. For the case of MCoRDS, there would be 15 passes corresponding to the 15 antenna elements in the system. This simplification allows us to assume that the temporal baseline is zero (thus $r_{l,p} = 0$), and that baseline components are known precisely (using information from the inertial measurement unit – IMU and ground surveys of antenna elements that account for wing lift during flight). With these assumptions, the interferometric phase for a single flight can be obtained using

$$\phi = -B_{z,p}k\cos\theta_l + B_{y,p}k\sin\theta_l\,. \qquad 3.2$$

We can now use classic tomographic SAR techniques [38] with Equation 3.2 to estimate θ_l.

3.2.1 Layer Slope Errors and Baseline Errors:

From Equation 3.2 we can evaluate the uncertainty associated with the interferometric measurements using the Tylor series expansion, and assuming statistical independence. We can then write the displacement accuracy as a function of cross-track slope and baseline as

$$\sigma_{\phi}^{2} = \left(\frac{\partial \phi}{\partial B_y}\right)^{2} \sigma_{B_y}^{2} + \left(\frac{\partial \phi}{\partial B_z}\right)^{2} \sigma_{B_z}^{2} + \left(\frac{\partial \phi}{\partial \theta_l}\right)^{2} \sigma_{\theta_l}^{2}. \qquad 3.3$$

where σ is the standard deviation. Dividing this equation by the wavenumber we get the displacement equivalent;

$$\sigma_{d}^{2} = \sigma_{B_y}^{2}(\sin\theta_l)^2 + \sigma_{B_z}^{2}(\cos\theta_l)^2 + \sigma_{\theta_l}^{2}\left(B_y \cos\theta_l + B_z \sin\theta_l\right)^2. \qquad 3.4$$

From Equation 3.4, a plot (Figure 3-3) showing the contribution of the baseline components to the error in the displacement was obtained. For B_y curve, $\sigma_{By} = 0.05m$ and for B_z curve, $\sigma_{Bz} = 0.1m$. We see that the contribution of the B_y and B_z errors depend on θ_l only and not the nominal value of B_y and B_z respectively. This shows that errors in B_y do not directly affect the displacement accuracy for small layer slopes, but errors in B_z directly impact the displacement accuracy. Note that baseline errors are constant with depth. This means that they do not affect the interpretation of the relative velocity and strain rate and are therefore of lower concern.

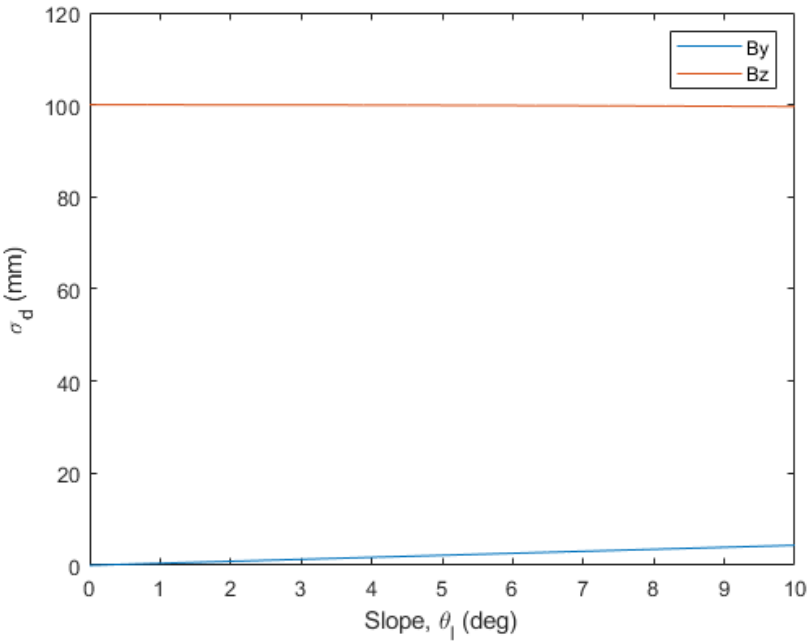

Figure 3-3: Displacement accuracy as a function of baseline. $\sigma_{By} = 0$ and $\sigma_{Bz} = 0.1$ m.

Likewise, we can also determine the displacement accuracy as a function of the slope and the resultant plots are shown in

Figure 3-4 and Figure 3-5 for B_z and B_y components respectively. For these plots, $\sigma_{\theta_l} = 0.2°$. It can be seen from Equation 3.4 that the errors in the slope are amplified by B_y, B_z, and the slope. Reasonable repeat pass accuracy of tracks is known to be on the order of 5 m RMS error.

Figure 3-4 shows that large vertical baselines can be tolerated since the displacement errors are small with respect to the vertical baseline. Figure 3-5 shows that even for the very small slope error of 0.2°, displacement errors greater than 1 cm are expected with this trajectory accuracy. When displacement accuracies on the order 1-2 mm are desired, the horizontal baseline must be kept below about 0.25 m. Given that the ideal airborne trajectory accuracy is 5 m RMS, one possible solution may be to use a large aperture, i.e., greater than 5 m, so that different sub apertures from each trajectory can be utilized for the phase centers of the respective apertures to

meet the tight horizontal baseline requirement. Finally, note that layer slope errors are a function of depth since the layer slope is a function of depth. These errors directly impact the interpretation of the vertical velocity and strain rate as a function of depth – the primary measurements of interest.

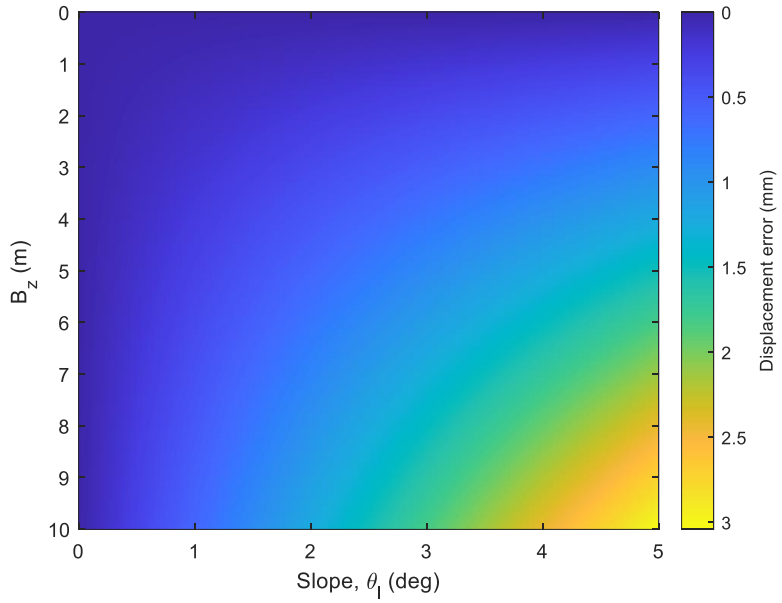

Figure 3-4: Displacement accuracy as a function of layer slope and cross-track baseline (B_z). $\sigma_{By} = 0$ and $\sigma_{Bz} = 0$.

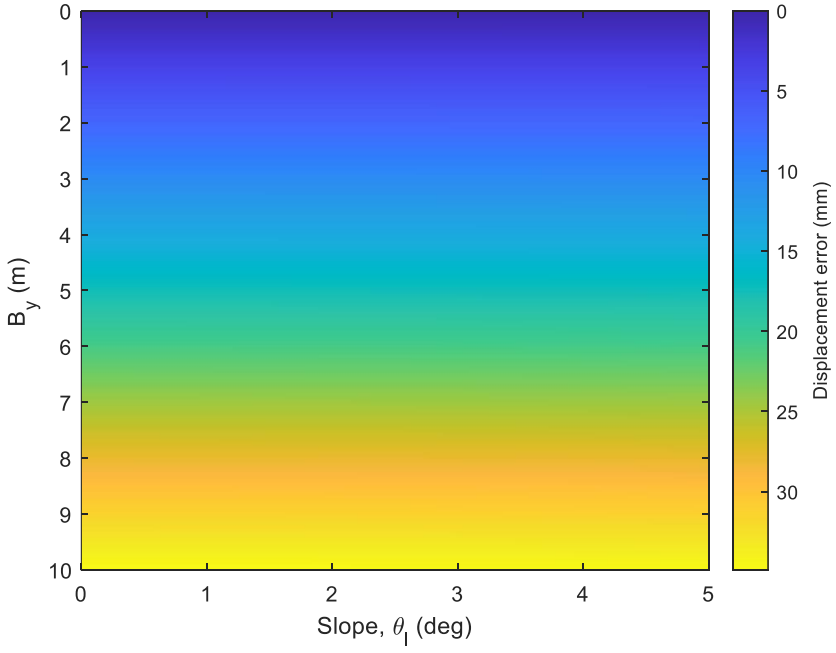

Figure 3-5: Displacement accuracy as a function of layer slope and cross-track baseline (B_y). $\sigma_{By} = 0$ and $\sigma_{Bz} = 0$.

Relative displacement accuracy as a function of position/baseline accuracy can also be determined by considering two layers that have different displacements but experience the same position/baseline error. Using the small angle approximations, the relative displacement error, d_r, is given by;

$$d_r = \frac{B_{z,p}(\theta_{l2} + \theta_{l1})}{2}(\theta_{l2} - \theta_{l1}) - B_{y,p}(\theta_{l2} - \theta_{l1}). \quad 3.5$$

where θ_{l1} and θ_{l2} are the DoA's corresponding to the two layers.

Dividing the relative displacement error into a component caused by the z-baseline and the y-baseline, we get;

$$d_{r,z} = \frac{B_{z,p}(\theta_{l2} + \theta_{l1})}{2}(\theta_{l2} - \theta_{l1}), \quad 3.6$$

and

$$d_{r,y} = B_{y,p}(\theta_{l2} - \theta_{l1}). \quad 3.7$$

GPS vertical position errors tend to be about twice that of horizontal position errors based on the MCoRDS GPS manufacturers Novatel and Applanix. Assuming the trajectory error in z is twice that of the trajectory error in y, we can write $B_{z,p} = 2B_{y,p}$ for the purposes of determining the displacement offset. If we further assume that the trajectory drift is random and independent in y and z, then we can take the square root of the variances; $d_{r,RMS} = \sqrt{d_{r,z}^2 + d_{r,y}^2}$.

Assuming $\theta_{l2} + \theta_{l1} \ll 1$ and $\theta_{l2} - \theta_{l1} \ll 1$, then

$$d_r \approx B_{y,p}(\theta_{l2} - \theta_{l1}) \approx B_{y,p}\sin(\theta_{l2} - \theta_{l1}). \quad 3.8$$

This is similar in form to that obtained for a single layer: $d \approx B_{y,p}\sin(\theta_l)$. This shows that the y-dimension of the unknown cross track baseline is the most important to relative displacement measurement.

The accuracy of slope estimation in the error analysis is found to be magnified by the baseline. Longer baselines, which are larger apertures, generally result in more precise slope estimates. This effect cancels out the magnified layer slope error caused by the baseline. The beamwidth (BW) of the delay and sum beamforming technique can be determined using the equation $BW = \lambda/d$. To estimate the beamwidth numerically, a rule of thumb is to use three times to ten times over the delay and sum beamforming technique. The beamwidth can now be expressed as $BW = \lambda/(3d)$ or $\lambda/(10d)$.

In general, higher signal-to-noise ratio (SNR) values result in more accurate direction of arrival (DOA) estimations. Multiple baselines can enhance DOA estimation accuracy by providing additional information to resolve ambiguity.

The MUSIC algorithm is SNR dependent and provides better resolution than the delay and sum beamforming technique. The resolution is inversely proportional to the baseline, while the error is proportional to the baseline. However, they roughly cancel out so that the error is independent of the baseline. The best results may be obtained by using a large baseline to calculate the slope and a small baseline to estimate the displacement.

3.2.2 Vertical Velocity Modelling

Englacial ice velocity evaluation is an important factor in dating ice (e.g. to determine the ideal location for an ice core site) [39]. To model the vertical velocity profiles, we need to first understand the geometry of the ice divide flow model as illustrated in Figure 3-6. The ice divide is the border dividing the opposing flow directions of ice in an ice sheet. The area to the sides of the divide are called the flanks. We expect lower vertical velocities near the divide than with the flanks [39]. For our modelling, we assume that the ice accumulates at a steady and homogeneous rate, a, at the ice sheet surface [39].

An ice sheet is in equilibrium when its average surface elevation is not changing. In this case, there is still snow accumulation due to new snow falls. This new snow accumulation becomes a new layer on top and the layers from the previous years each move down as illustrated in Figure 3-7.

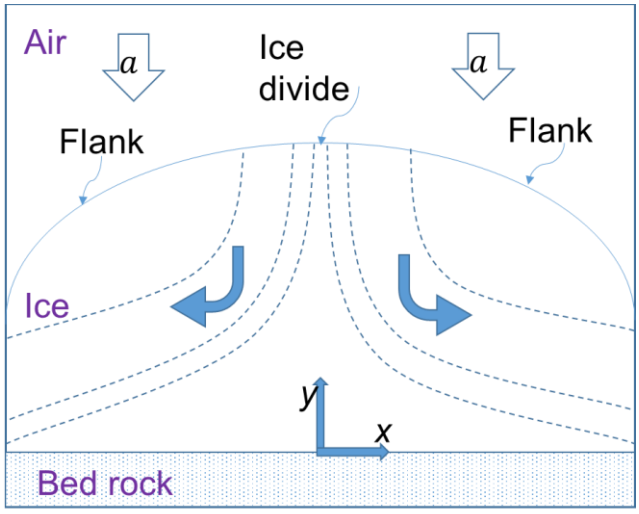

Figure 3-6: Ice divide flow model geometry.

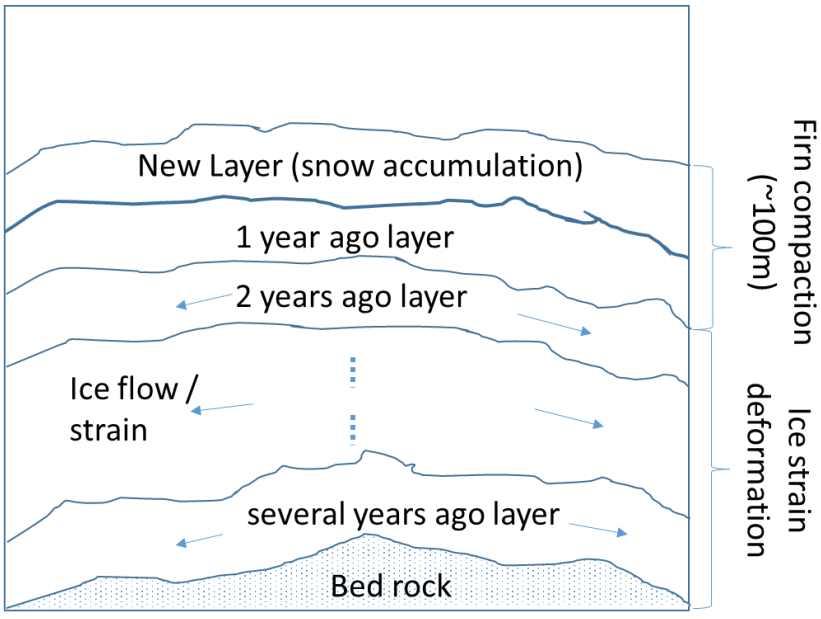

Figure 3-7: Ice sheet layer illustration.

The *overburden pressure* due to the weight of the new snow accumulation layer causes compression in the deeper ice layers by pushing air out of the snow. This is called *firn compaction*. In addition to firn compaction, the overburden pressure causes divergence of the ice by pushing the ice to the sides. This is referred to as *ice flow* or *ice strain*. In equilibrium, the amount of snow accumulation is equal to the vertical velocity, and thus;

$$Snow\ Accumulation = Firn\ Compaction + Strain\ Deformation \tag{3.9}$$

From the Lliboutry (1979) model (Equation 3.10) [39], we are able to plot the expected vertical velocity profiles as shown in Figure 3-8.

$$v(v_s, p, \zeta_l) = v_s \left(1 - \frac{p+2}{p+1}(1-\zeta_l) + \frac{1}{p+1}(1-\zeta_l)^{p+2}\right) \tag{3.10}$$

where ζ_l is the elevation of layer l normalized to the ice thickness, v_s is the vertical velocity at the surface, and p is the ice rheology parameter. Figure 3-8 shows an example for several different realizations of the ice rheology and a typical annual snow accumulation (0.02 m) and ice thickness (2750 m).

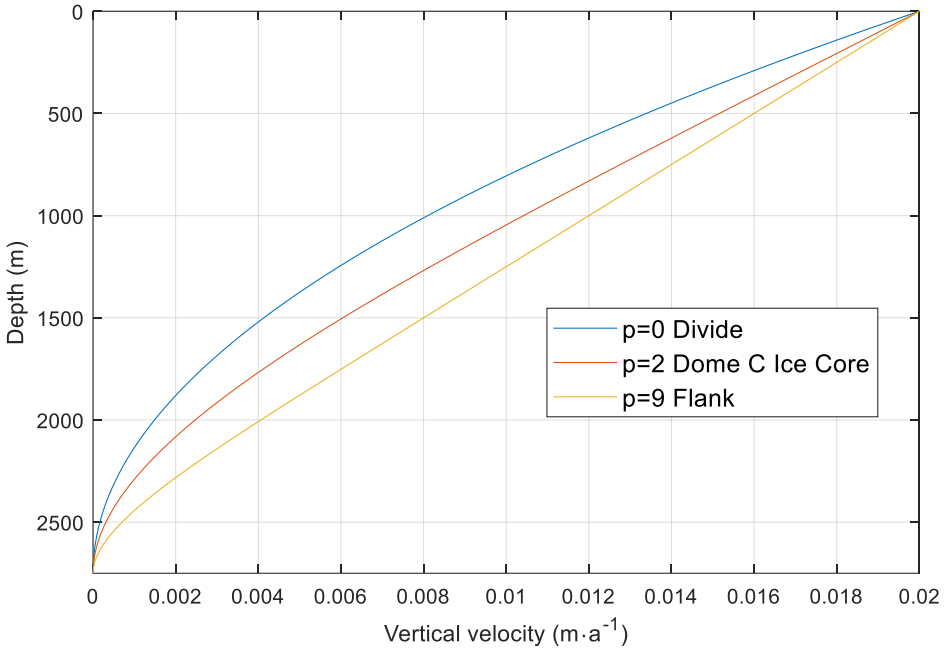

Figure 3-8: Expected vertical velocity profiles

It is important to note that the Lliboutry model is a simplified representation of the behavior of ice and may not accurately capture all of the physical processes that are important for accurately modeling ice dynamics. Nonetheless, it remains a widely used and well-established model for studying ice sheets and glaciers and can provide useful insights into the behavior of these complex systems.

3.2.3 Vertical Velocity Measurement

The ice sheet vertical velocity measurement can be done using ground-based or airborne methods. Ground-based methods are conducted from the ice sheet's surface or the surrounding terrain, while airborne methods involve using aircraft or satellites to gather data from above the ice sheet. Ground-based systems can provide high-resolution data on small spatial scales. Ground-based systems include seismic surveys, ice core analysis, strain gauges, and ground-based radar. On the other hand, airborne methods can cover larger areas more quickly and provide a more

comprehensive view of the ice sheet. Airborne methods can include airborne radar systems, laser altimeters, or satellite-based remote sensing techniques. These methods can provide data on the entire ice sheet or large portions of it, allowing for a better understanding of the overall behavior and trends of the ice sheet. Combining these methods may provide the most comprehensive understanding of ice sheet dynamics.

3.2.3.1 Airborne or Spaceborne Systems

Satellite Altimetry: Satellite altimetry measures the distance between the satellite and the Earth's surface, which can be used to infer changes in ice surface elevation over time. By combining this information with other data, such as ice density and surface slope, researchers can estimate the internal vertical velocity of the ice sheet. This method can provide a large-scale view of ice sheet vertical velocity, but it may not be as accurate as other methods.

Airborne Radar Systems: Radar altimetry measures the distance between the aircraft and the ice surface, which can be used to infer ice surface elevation changes over time. Ice-penetrating radar can provide detailed images of the internal structure of an ice sheet. By analyzing these images, researchers can identify and measure the motion of different layers within the ice sheet. Vertical englacial velocity profiles have been estimated using repeat-pass interferometry with the multitemporal airborne radar sounding surveys: like MCoRDS from CReSIS , and High Capability Airborne Radar Sounder (HiCARS) from the University of Texas.

Airborne Laser Altimetry: This method uses laser pulses to measure the height of the ice surface and its variations. By combining the height measurements with GPS data, the surface velocity of the ice can be determined.

3.2.3.2 Ground-based Sounder Systems

Seismic surveys: Seismic surveys can measure an ice sheet's vertical motion by placing sensors on the ice surface and using sound waves to measure changes in ice thickness. Researchers can calculate ice sheet vertical velocity by combining seismic data with GPS data.

Ice Core analysis: Ice core analysis provides information about ice sheet vertical velocity by analyzing the age of layers in ice cores to determine how quickly the ice sheet has accumulated over time.

Global Positioning System (GPS): GPS receivers can measure the vertical motion of ice sheets when placed on the ice surface to measure the changes in height over time. This method can provide accurate ice sheet vertical velocity measurements, but it is limited to areas where GPS signals can be received.

Strain Gauges: Strain gauges can be attached to the ice sheet surface to measure the deformation of the ice as it moves. By measuring the changes in strain over time, it is possible to determine the velocity of the ice sheet.

Ground-based Radar Systems: These can measure the thickness of the ice sheet and the internal layers within the ice. By comparing radar images taken at different times, it is possible to determine the vertical velocity of the ice sheet. An example of a ground-based radar systems for which this has been demonstrated include the network-analyzer based phase-sensitive radio echo sounder (pRES) and the deramp on receive autonomous phase-sensitive radio echo-sounder (ApRES).[40]

3.3 Review of Prior Work

Since the DInSAR technique was first proposed in 1989 by Gabriel et al [41], it has been improved and applied to monitoring and measuring of phenomenon such as glacier movement [42], volcanic activity [43], seismic activity [44], mining activity [45], and urban subsidence [45]. DInSAR's accuracy is in the order of a few millimeters in monitoring ground displacement along the Radar line of sight (LOS). However, DInSAR is prone to temporal decorrelation of surface scatterers due to surface change processes, spatial decorrelation due to the large baseline between SAR image acquisitions, atmospheric disturbances causing variation in signal delays, and problems with resolving the phase ambiguity [46] [47]. These lead to a limited number of image pairs suitable for interferometric processing.

The accuracy of future sea-level rise projections is limited by parametric uncertainty in ice-sheet models [48]. Dating ice cores requires knowledge of englacial ice velocities and it is done by counting annual variations in ice properties. This is well expounded upon by Kingslake et al. (2014) in [39] where the measured (from radar data) vertical velocity was fitted to the expected vertical velocity model using the Lliboutry (1979) model. Ground-based *phase sensitive Radio Echo Sounders* (pRES) are commonly used in measuring deformation in real-time using time-lapse imagery of point targets in the subsurface as demonstrated by Nichols et al. (2015) [37]. For airborne applications, we need to isolate changes in range for subsurface targets associated with ice flow using the well-known precise time-varying platform position. Castelletti et al. (2020) and Miller et al. (2020) showed that differential interferometric methods can be used on airborne radar depth sounder data to estimate the englacial range displacement of ice-sheet internal layers by using data from the High Capability Radar Sounder (HiCARS) and MCoRDS respectively [36, 49].

This research applies new swath radar processing techniques to englacial layering to facilitate subsurface interferometric processing of the Operation IceBridge (OIB) radar data archive. This will result in the concurrent production of fine-resolution maps of the subglacial topography and direct observations of ice deformation and transport from measured englacial vertical velocities. These data products will be used to evaluate ice-sheet dynamics on various timescales, which will expand on the understanding of glacier processes that affect ice mass balance and sea-level rise. By measuring patterns of englacial velocity associated with solely stable ice-divide flow (the Raymond effect), subsurface radar interferometry can be used to diagnose ice-divide response times over longer timescales than any other observational method [39]. We use distributed interferometric measurements to provide the first comprehensive estimate of Greenland divide dynamics and identify any disequilibrium (englacial velocities that are inconsistent with surface mass balance, surface velocity, and elevation) in ice flow across the divide that might drive future divide migration.

3.3.1 DInSAR Algorithm

SAR interferometry requires a pixel-to-pixel match between common scattering features in SAR image pairs, and thus coregistration, which aligns the SAR images from two passes, is an essential step for accurately determining phase difference. The imprecise repeat-pass geometry makes coregistration difficult.

The following steps highlight the process of the current DInSAR algorithm (Figure 3-9) implemented in the CReSIS toolbox:

1. Equalization and time shift of each MCoRDS SAR image to correct for system phase and time deviations for each channel or pass.

2. Coregistration of the SAR images using cross-correlation and motion compensation assuming zero slope layers. In this step, each image is projected onto a master image using the trajectory information followed by interpolating each image onto the along-track master image pixel locations. A time-delay is applied in the frequency-domain to each image to compensate for the difference in elevation between flights. This time delay removes the phase and time delay due to the vertical component of the baseline for zero-slope or perfectly horizontal layers.
3. Estimation of the direction of arrival for each image pixel using the array of coregistered images to estimate cross-track slope phase contributions. This step only uses passes from a single flight to ensure precise knowledge of the relative baselines. In this step, the coregistered images are combined using the Multiple Signal Classification (MUSIC) array processing method and the DoA of the returned signal is estimated using a basic peak tracking algorithm.
4. The coregistered images are interfered after application of phase corrections for motion compensation using the estimated cross-track slope and estimated GPS position errors.

Cross-track slope compensation involves applying a phase correction after motion compensation and before array processing that is based on the estimated cross-track slope. The phase correction is related to the slope by the interferometric phase in Equation 3.2.

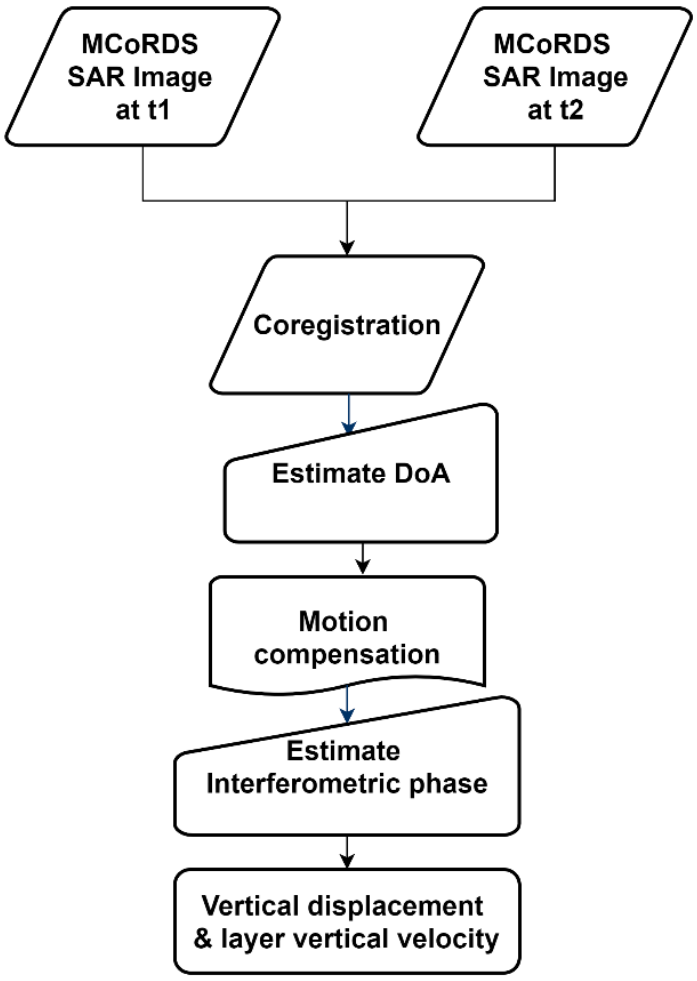

Figure 3-9: The CReSIS DInSAR Algorithm.

The DInSAR algorithm is applied to data from NASA Operation Ice-Bridge (OIB), and section 3.3.2 shows the results for the flights near the Summit camp in Greenland and the EGIG (Expéditions Glaciologiques Internationales au Groenland) line.

3.3.2 CReSIS Toolbox Multipass Algorithm Results

The existing multipass method exploits passes from a single flight, as discussed in section 3.3.1, to estimate the layer slope, θ_l, and then uses this result and differential interferometry to estimate $r_{l,p}$ from two separate flights. Figure 3-11, Figure 3-12, and Figure 3-13 show the resulting

interferogram, coherence plot, and range displacement for a pair (2012 and 2014) of NASA Operation Ice-Bridge (OIB) flights near Summit in Greenland after motion and cross-track slope compensation. The dark or black regions in the interferogram correspond to low coherence, whereas bright or colorful regions designate high coherence. It should be noted that baseline components for the second flight have an additional error due to the GPS trajectory errors.

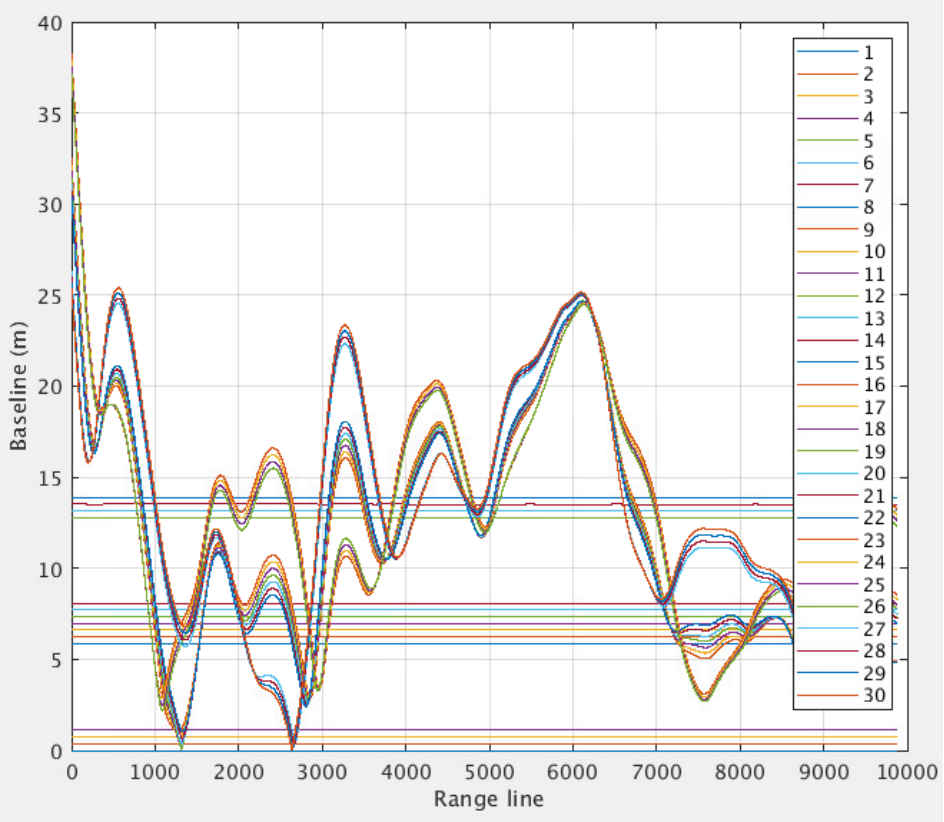

Figure 3-10: Baselines across combined frames from the Summit line.

From Figure 3-10, it can be seen that the baselines vary between 0 m to about 40 m. This gives an indication of the separation between the repeat flights.

In multipass interferometry, the baseline determines the spatial resolution of the interferogram and affects the accuracy of the displacement measurement. If the baseline is long, the spatial resolution of the interferogram is high, but the deformation measurement is less sensitive. On the other hand,

if the baseline is short, the spatial resolution of the interferogram is low, but the deformation measurement is more sensitive [50].

As described in the previous chapter, in traditional InSAR, the height-to-phase conversion equation is given by:

$$z = -\frac{\phi_{int}\lambda R \sin\theta_i}{4\pi B_\perp} \tag{3.11}$$

From this equation, it can be seen that as the baseline increases, the interferometric phase becomes more sensitive to height changes. In other words, larger baselines result in greater sensitivity to height changes. Equivalently for ice sheet measurements, larger baselines lead to finer layer slope resolution. Conversely, smaller baselines result in lower sensitivity to height changes.

It is important to note that the relationship between baseline and accuracy is not linear and depends on several other factors, such as the coherence of the interferogram, the noise level, and the geometry of the imaging system. Therefore, the optimal baseline for a given DInSAR application depends on a careful trade-off between spatial resolution and sensitivity to height changes.

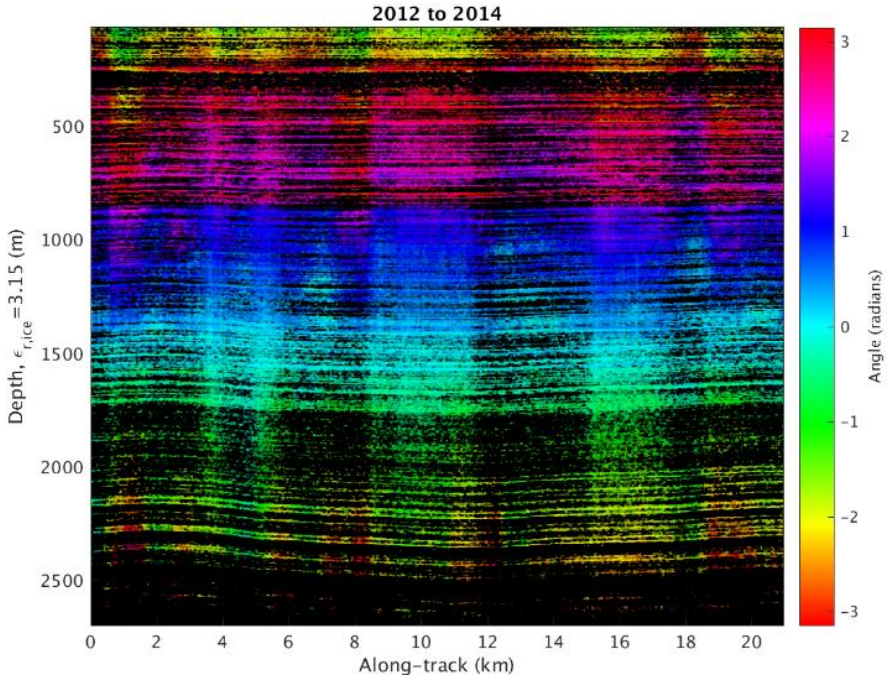

Figure 3-11: An example of an interferogram made by two flights near Summit, Greenland.

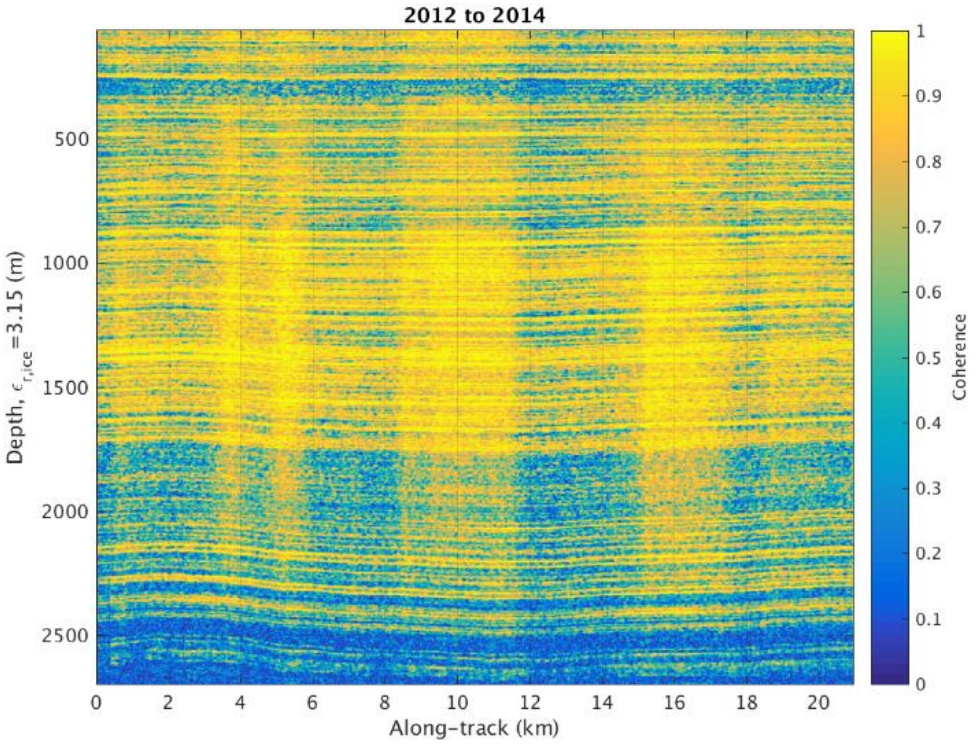

Figure 3-12: Coherence plot for passes near Summit, Greenland.

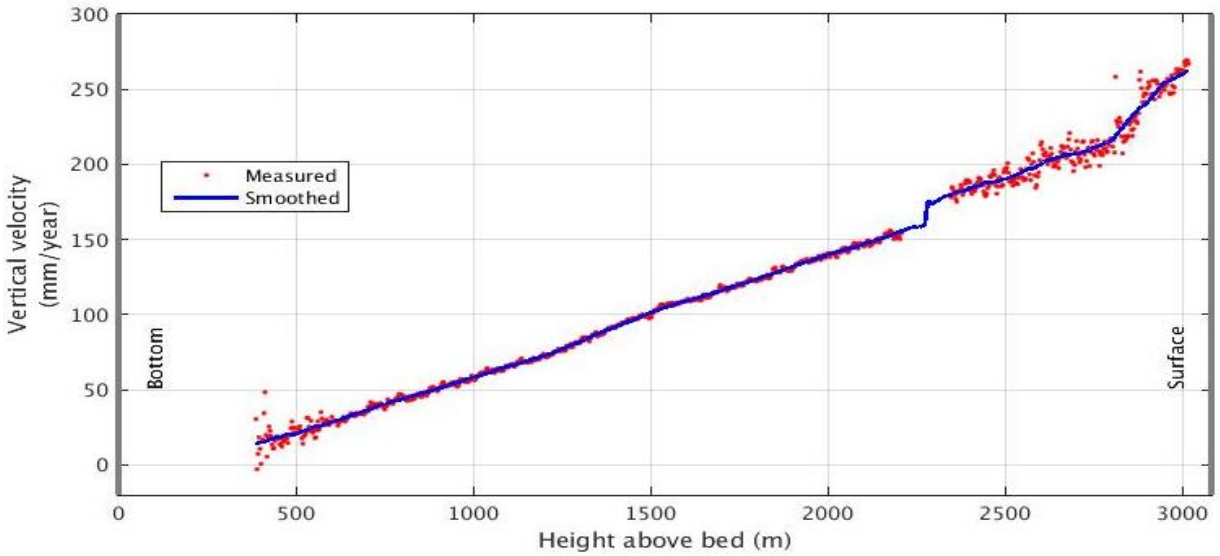

Figure 3-13: An example of the range displacement at the center of the interferogram.

We see that the vertical velocity plot in Figure 3-13 exhibits the same general trend as the plot derived from the Lliboutry model in Figure 3-8. We expect close to zero vertical velocity at the bottom (bedrock), which gradually increases in a near-linear way towards the surface, as shown in the plot obtained from actual data.

Furthermore, the results of combined repeat pass images from the EGIG line are presented here. The master pass for all results is pass 8 which was taken in 2014. The plots presented in this section show the baseline between each pass and the master pass (Figure 3-14), the interferogram (Figure 3-15), the interferogram coherence (Figure 3-16), and the estimated vertical strain rates based on the phase ramp within the interferograms (Figure 3-17).

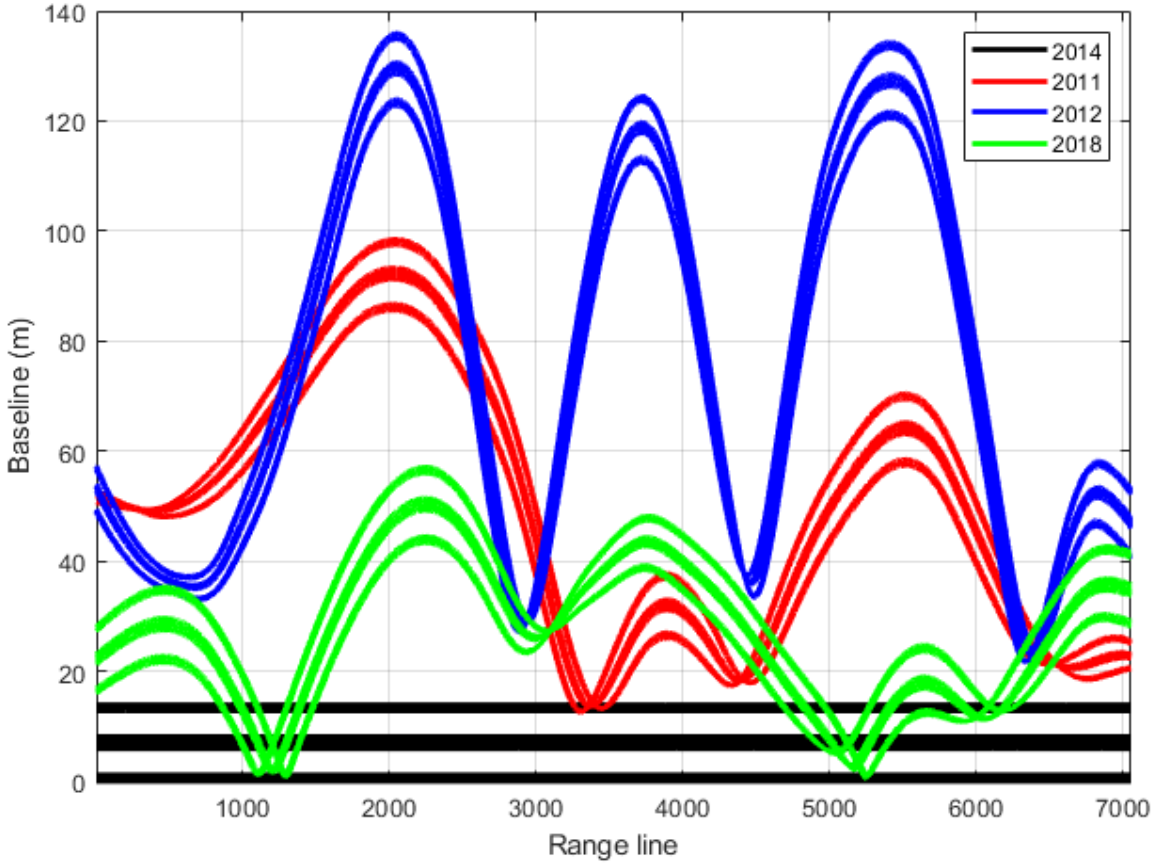

Figure 3-14: Baselines across combined frames from the EGIG line.

From Figure 3-14, it can be seen that the baselines vary between 0 m to about 140 m. This gives an indication of the spatial separation variation between the repeat flight trajectories.

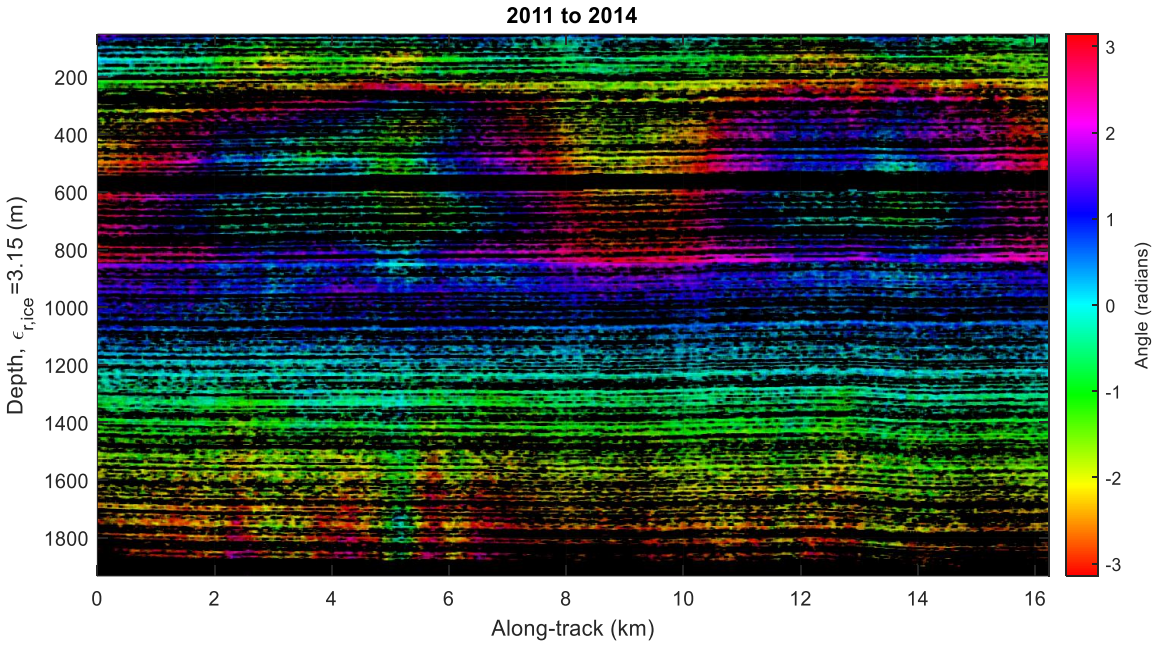

Figure 3-15: 2011 to 2014 Interferogram from the EGIG line

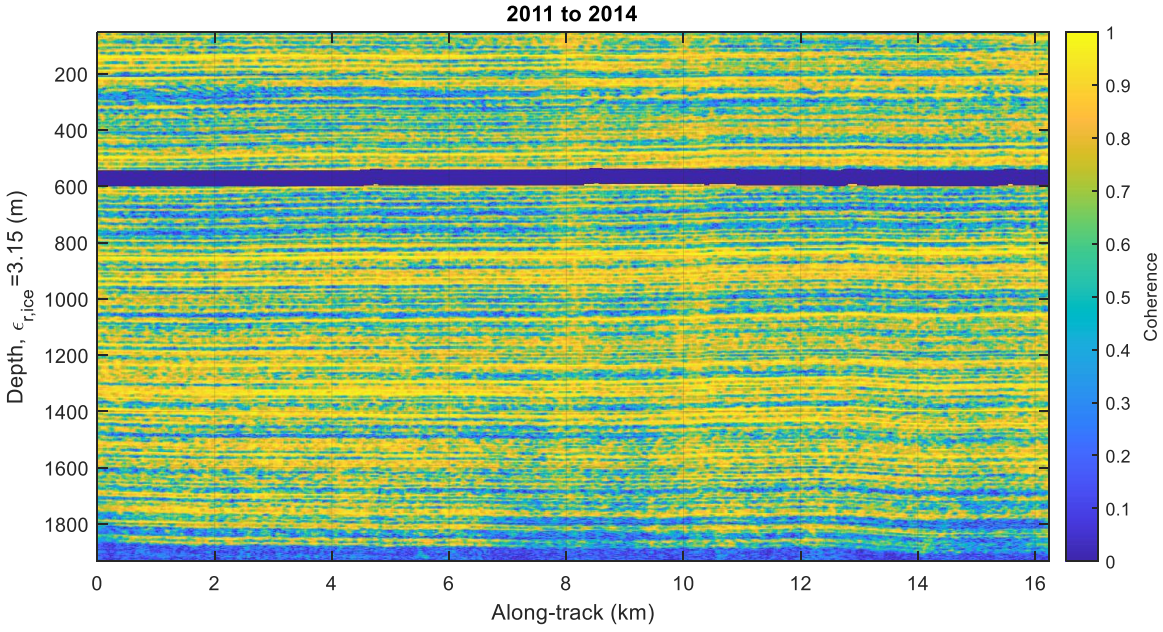

Figure 3-16: Coherence plot for 2011 to 2014 for the EGIG line

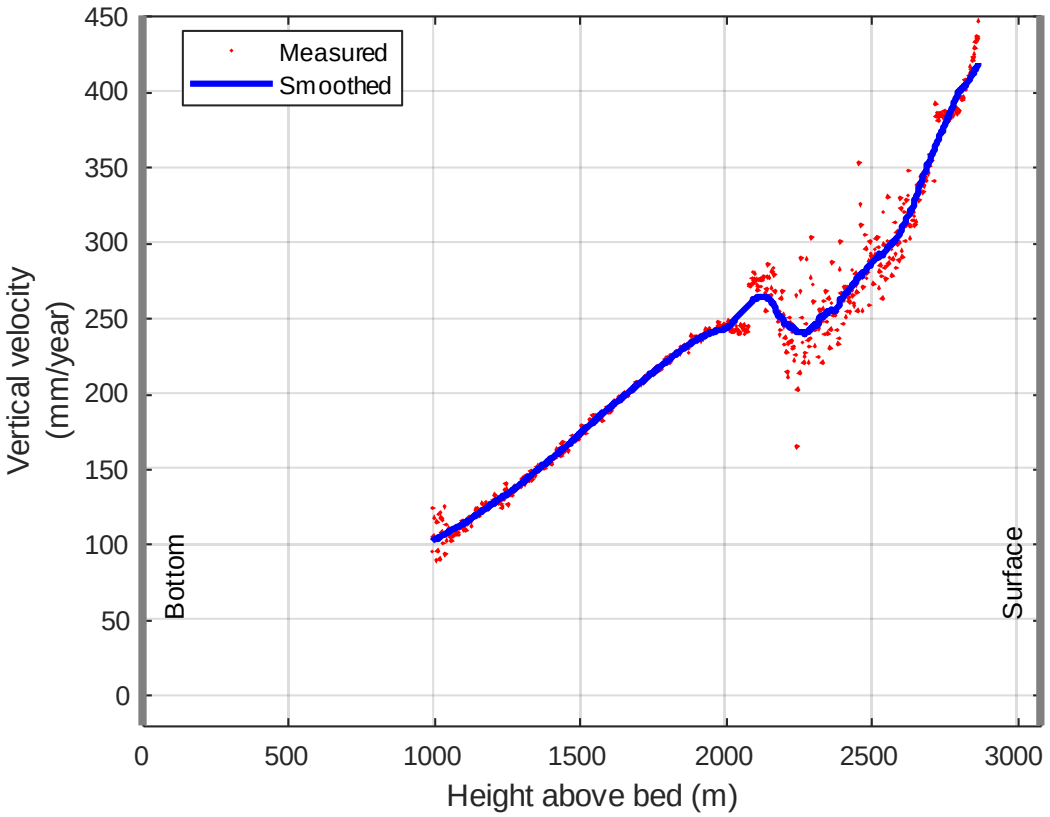

Figure 3-17: Vertical velocity (depth change) estimate between 2011 and 2014 for EGIG line.

Figure 3-15 shows the plot of the interferometric phase for 2011 to 2014 passes. Each pass produces an image from each of the 15 antenna elements. The 15 images from each flight are coherently summed according to the delay and sum beamformer before forming the interferometric phase between the flights. As the time separation decreases, the phase wrapping reduces since the phase wrapping represents the integration of the vertical strain rate of the ice sheet over time. The longer the integration duration, the greater the accumulated displacement will be. Due to the ice physics at this location, the layers at the top of the image are moving away from the radar faster than the layers at the bottom. Therefore, as we travel back in time, the layers at the top of the image would have been closer and closer to the radar, and this is the cause of the increasing positive phase toward the top of the image. The opposite is true toward the bottom of the images.

The coherence for the interferogram is shown in Figure 3-16. The phase and coherence are estimated using a 9 by 45 boxcar window.

Figure 3-17 shows the vertical velocity calculated for the 2011 to 2014 interferogram and using the entire time gate of each interferogram to estimate the phase ramp. The phase ramp is estimated using an oversampled FFT of the interferogram. Estimating the vertical strain rate or change in velocity with depth is done by estimating the slope of the phase ramp present within the interferogram images. At this location, the vertical velocity and the vertical strain rate are expected to be greatest at the surface and decrease in rate until they approach zero at the bedrock in agreement with the ice sheet model of Figure 3-8. The vertical velocity plots exhibit a kink for both the EGIG and Summit lines that is attributed to a waveform-to-waveform phase discontinuity that is discussed in section 3.4.7.

These results show that airborne DInSAR is possible with MCoRDS data. The strain rate measurements are consistent with the expected trend.

3.4 Joint Parameter Estimation

To improve the accuracy of both the tomographic swaths and vertical velocity measurements produced from multipass measurements, joint parameter estimation has been implemented first on simulated data and then on actual data collected by CReSIS.

The standard deviation of the baseline errors that are due to GPS/INS trajectory errors can be estimated based on manufacturer datasheets and precise point positioning (PPP) software. The standard deviation of this position error is on the order of 5 cm. Since this error affects all the ice layers in the ice column the same way, the relative displacement measurement between layers in a single column is unaffected to the first order, but the direction of arrival measurement to handle the slope is directly affected.

The range displacement of layer l is related to the horizontal and vertical displacement by:

$$r_{l,N} = \cos(\theta_l)\, v_l t_p + \sin(\theta_l)\, h_l t_p \,, \qquad 3.12$$

where v_l is the average vertical velocity of the layer, h_l is the average horizontal velocity, and $t_{l,p}$ is the temporal baseline between pass p and pass 1.

We jointly solve for the observed directions of arrival, θ_l for each layer, the baseline, and the range displacement using a maximum likelihood estimator (Figure 3-18), similar to array calibration using surface scatterers [51]. Instead of solving for the slope from a single flight, then solving for the displacement between two flights, followed by estimating the baseline, we jointly solve for these.

Finally, we incorporate parametric models for the vertical displacement and the above-mentioned horizontal velocity into the maximum likelihood estimator framework. The vertical velocity model parameters that are tuned by the maximum likelihood estimator are the vertical velocity at the surface, v_s, and an ice rheology parameter, p. The vertical velocity is equal to the surface accumulation when the ice sheet is in a steady state, and this may be estimated from other remote sensing measurements or weather models [52]. Similarly, the horizontal velocity can be measured from satellite remote sensing measurements [53] and propagated to depth using models [54].

The estimated vertical velocity is compared against ice flow models from the glaciology community, pRES/ApRES measurements, and ice core data. These are trusted sources of data that can be used as ground truth for vertical velocity. The estimated cross-track slope is compared to that obtained from along-track SAR processing of crossing lines.

The joint estimation framework is applied to data collected by MCoRDS over the Summit line. The Summit Line was chosen because it has multiple flights, the presence of in-situ measurements, and the fact that the Summit Line crosses the ice divide.

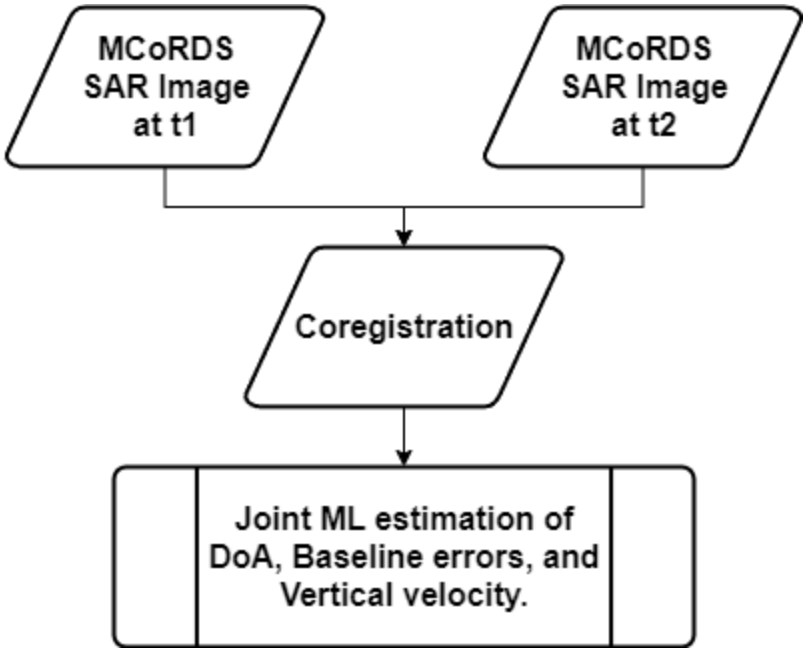

Figure 3-18: Proposed joint estimation framework.

By extension from Equation 2.45, the log-likelihood function for the joint estimation of the parameters for each SAR pixel can be written as;

$$\boldsymbol{L}_{r,c} = -MP\log\sigma^2 - \frac{1}{\sigma^2}\sum_{m=1}^{M}\left|\boldsymbol{x}_{r,c} - \boldsymbol{A}\left(\theta_{l,r,c}, v_{l,r,c}, h_{l,r,c}, B_{y_c}, B_{z_c}\right)\boldsymbol{s}_{r,c}\right|^2, \tag{3.13}$$

where the subscript r and c represent range bin (rows) and range line (column) indices respectively, B_{y_c} and B_{z_c} are the baseline errors, $v_{l,r,c}$ is the vertical velocity (which is constrained by the ice rheology parameter, $p_{r,c}$ and surface velocity, $v_{s,r,c}$), $h_{l,r,c}$ is the model-constrained horizontal velocity, and $\theta_{l,r,c}$ is the slope. The steering matrix elements for pass p are now defined as

$$\boldsymbol{a}\left(\theta_{l,r,c}, v_{l,r,c}, h_{l,r,c}, B_{y_c}, B_{z_c}\right) = e^{-jk\left(d + r_{l,N}\right)} \qquad 3.14$$

$$= e^{-jk\left(\left(v_{l,r,c}t_p - B_{z_c}\right)\cos\theta_{l,r,c} + \left(B_{y_c} + h_{l,r,c}t_p\right)\sin\theta_{l,r,c}\right)},$$

where t_p is the temporal baseline, $d = -B_{z_c,p}\cos\theta_{l,r,c} + B_{y_c,p}\sin\theta_{l,r,c}$ is the displacement derived from Equation 3.2, and $r_{l,N} = \cos\left(\theta_{l,r,c}\right) v_{l,r,c}t_p + \sin\left(\theta_{l,r,c}\right) h_{l,r,c}t_p$ is the range displacement from Equation 3.12. The steering vector above is obtained by taking into account the contributions from the layer motion and offsets added to all the slave pass sensors because of the GPS error.

We can now write the joint estimation log-likelihood function as

$$\boldsymbol{L}\left(\theta, v\,, B_z, B_y\right) = \sum_{c=1}^{N_x}\sum_{r=1}^{N_t}\boldsymbol{L}_{r,c}, \qquad 3.15$$

where N_x is the number of along-track samples in the complex SAR image (i.e. number of range lines in the azimuth dimension) and N_t is number of fast-time samples in the complex SAR image (i.e. number of snapshots in the range dimension) to consider in the joint estimation.

As in Equation 2.47 the joint maximum likelihood estimation is achieved by doing the maximization across all these log likelihood cost functions:

$$\theta, v\,, B_z, B_y = \arg\max_{\theta, v\,, B_z, B_y}\sum_{c=1}^{N_x}\sum_{r=1}^{N_t}\left(\boldsymbol{P}_{\boldsymbol{A}\left(\theta, v\,, B_z, B_y\right)}\boldsymbol{R}\right). \qquad 3.16$$

3.4.1 Joint Estimation Simulation

To demonstrate the feasibility of the joint parameter estimation framework for vertical velocity, cross-track slope, and baseline errors, preliminary results from a MATLAB simulator are presented in section 3.4.2.

The simulation set-up makes the following assumptions:

- Each flight has 15 antenna elements, and each element is considered to be a single pass (15 passes per flight). Therefore, for each flight, the baseline is precisely known between the passes. The baseline between passes on different flights is not precisely known because the GPS error for each flight is different. The baseline error exists between flights i.e., between the first 15 passes and the next 15 passes. Fifteen elements were considered to match the elements found on the MCoRDS system (Table 3-1).
- It is assumed that SAR processing is done and we do not consider the effects of ice.
- It is assumed that there is no along-track variation of parameters and that all variation is in the cross-track or range dimension.

The maximum cross-track slope and maximum absolute slope change are constrained to 1 degree. The baseline error is limited to 0.1 m. The maximum vertical velocity is constrained to 1 m/a, and does not change over time, and changes slowly (and linearly) versus depth. Therefore, the vertical velocity model can be fitted with a 1^{st} degree polynomial as a function of depth and does not change in the along-track direction. The simulation was set up using 100 cross-track pixels and 50 along-track pixels for 100 Monte Carlo runs.

The joint MLE framework outlined earlier was used to estimate the parameters, and then it was run for different vertical velocities, cross-track slopes, and baseline errors. Then, all the likelihood functions were summed up using those errors. This sum is the overall likelihood for that particular set of vertical velocity, slope, and baseline error parameters. The joint estimate for the vertical velocity, cross-track slope, and baseline error parameters is the set of parameters that gives the highest summed likelihood.

In general, the joint estimation simulator is capable of handling data from any number of passes collected across any number of flight lines as long as the steering vectors for the passes can be

parameterized and the parameters estimated uniquely. The initial version of the simulator considers a limited set of possible dependencies (e.g., zero correlation between fast-time samples, constant internal layer slope field, constant baseline error, linear vertical velocity dependence on depth, and no dependence in along-track). The simulator will be adapted to consider fast-time correlation and more complex spatial dependencies for each of the other parameters. The simulator and joint estimator will also be adapted for deployment on a computer cluster.

3.4.2 Simulation Results

The following simulation results were obtained after running the optimizer for the joint estimation of vertical velocity, cross-track slope, and baseline errors. Figure 3-19 to Figure 3-21 show the RMSE analysis for each of the parameters, and we see that as the SNR increases, the RMSE reduces as expected.

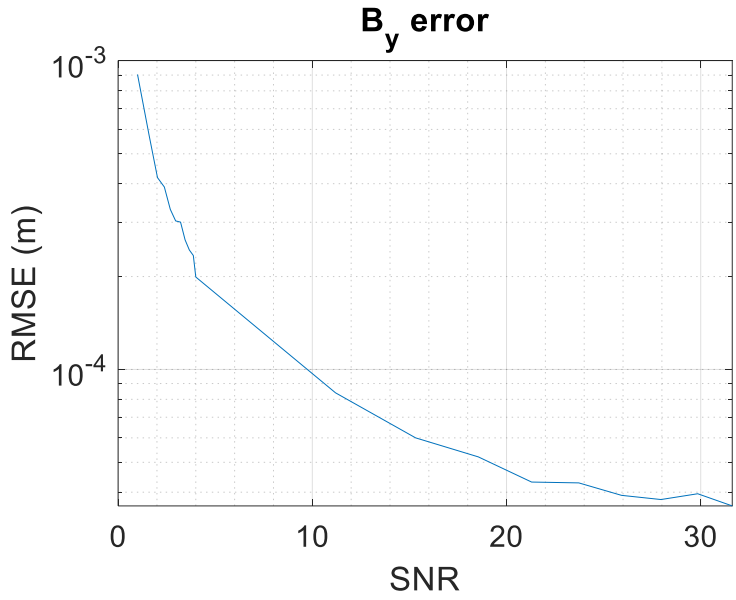

Figure 3-19: RMSE plot for baseline errors.

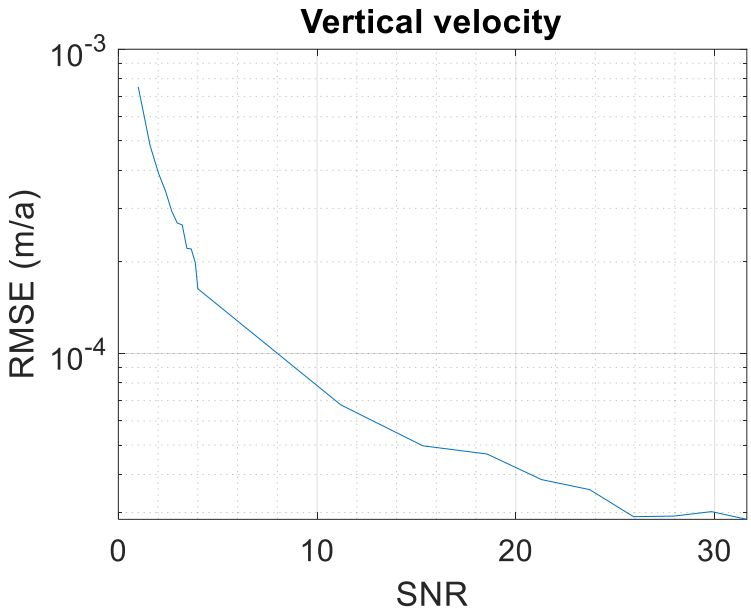

Figure 3-20: RMSE plot for vertical velocity.

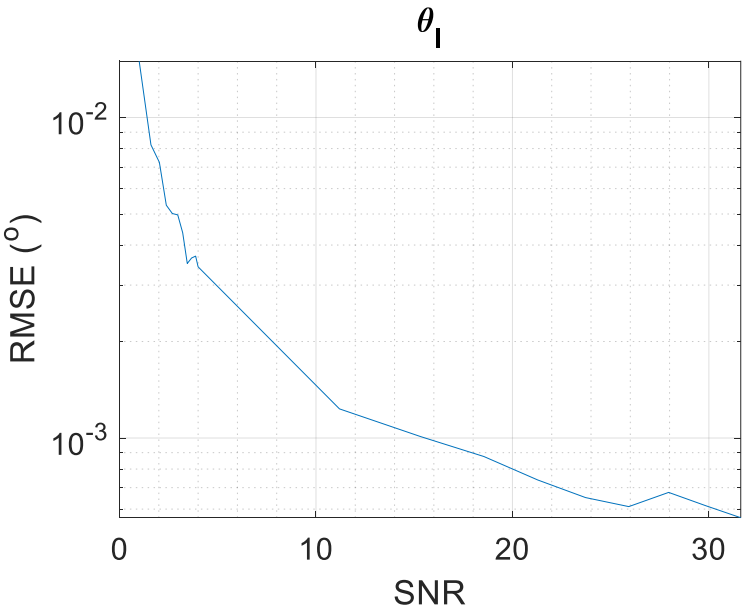

Figure 3-21: RMSE plot for slope.

The RMSE plots above are not smooth, probably due to the limited number of runs used in this simulation. However, the general trend is clear.

Figure 3-22 shows the interferograms generated using passes on the same flight and therefore, there is no temporal baseline between the 15 elements on the same flight. The master pass is pass 1. These results are similar to non-differential InSAR processing results.

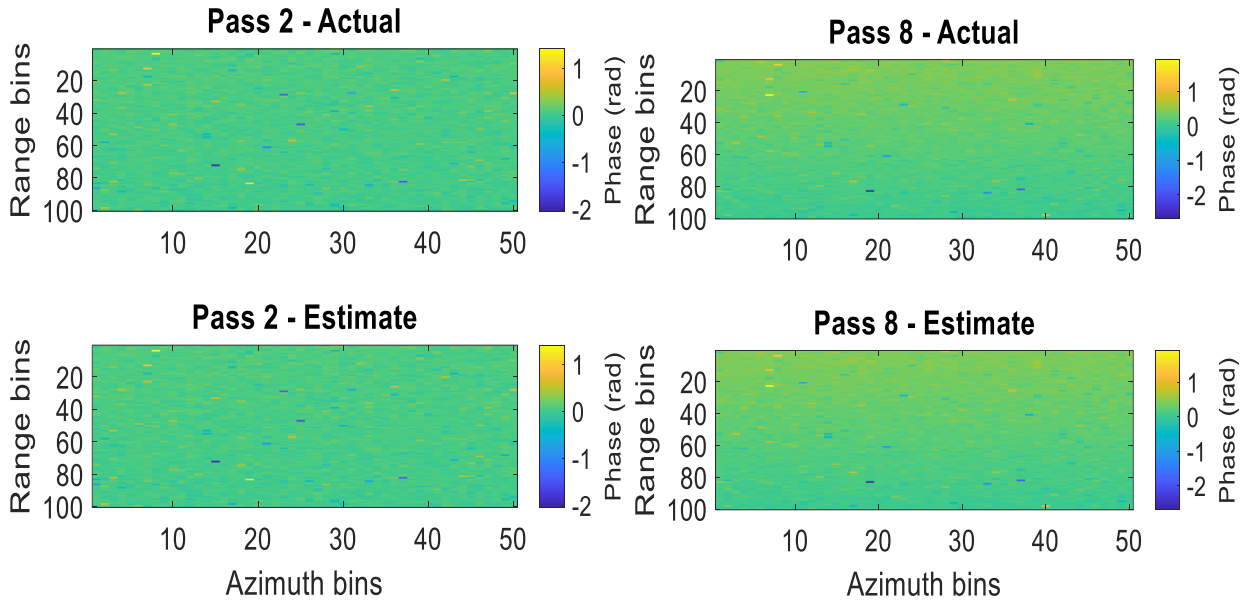

Figure 3-22: Interferograms for passes 2 and 8 (using pass 1 as the master pass).

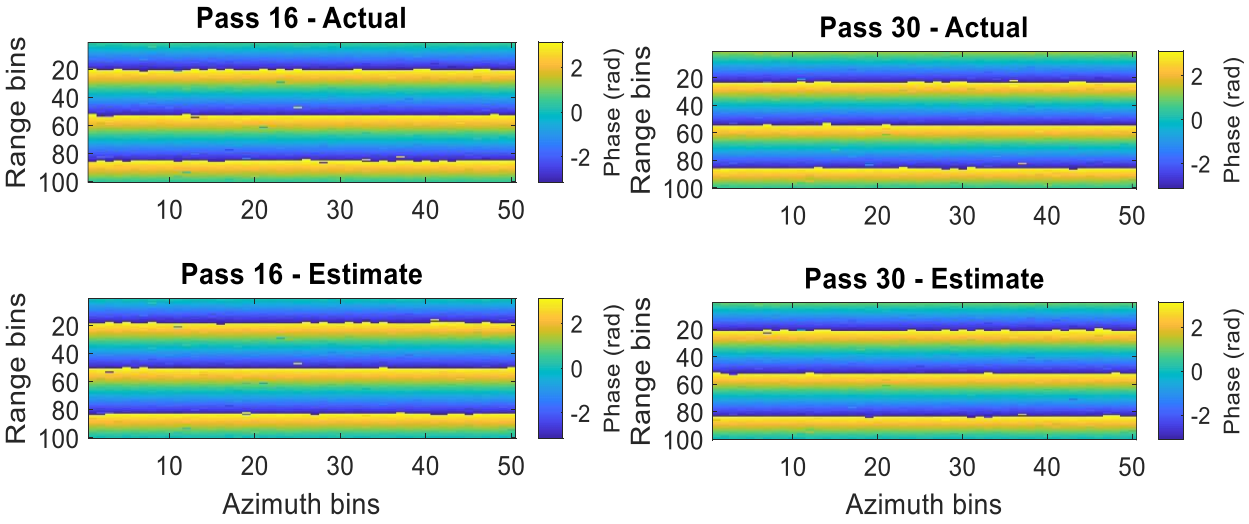

Figure 3-23: Interferograms for passes 16 and 30 (using pass 1 as the master pass).

Figure 3-23 shows interferograms obtained using passes from the second flight and the master pass from the first flight. These results are differential InSAR results and include both an unknown baseline error and a target position shift due to the temporal baseline. For both the single flight passes and the repeat flight passes, the master or reference pass used to form the interferograms is pass 1.

In the pairs of interferograms shown in Figure 3-22 and Figure 3-23, the top plots show the measured interferograms, and the bottom plots show the interferograms generated by the jointly estimated parameters. For the correct jointly estimated parameters, these plots should be identical except for the effects of the additive noise to the signal, as shown in Figure 3-22 and Figure 3-23. From the results, we saw that there is potential for the concept of using joint estimation rather than breaking the problem down to solving for the slope from a single flight and then solving for the vertical displacement between two flights, followed by estimating the baseline between flights.

After optimizing the solver and setting up the simulator to be as close to the real-life environment as possible, this joint estimation framework is applied to actual data collected by CReSIS, and the results are discussed below.

3.4.3 Joint Estimation with MCoRDS Data

The current multipass routine (Figure 3-9) has been modified to apply joint estimation after co-registration instead of the former stepwise implementation as shown in Figure 3-18. To increase the efficiency of the algorithm, the data is broken down into blocks in both the fast time and slow time axis. This is made possible because of the assumption that the parameters being estimated don’t change too quickly within the block. This is in agreement with the physical ice sheet dynamics. The joint estimation algorithm is applied to data from flights near Summit camp for the years 2012 (frame 8) and 2014 (frame 41). The geographical location of the two frames is shown

in Figure 3-24 and Figure 3-25 for 2012 and 2014 respectively. The results are compared with ground truth data to validate the joint estimation framework performance.

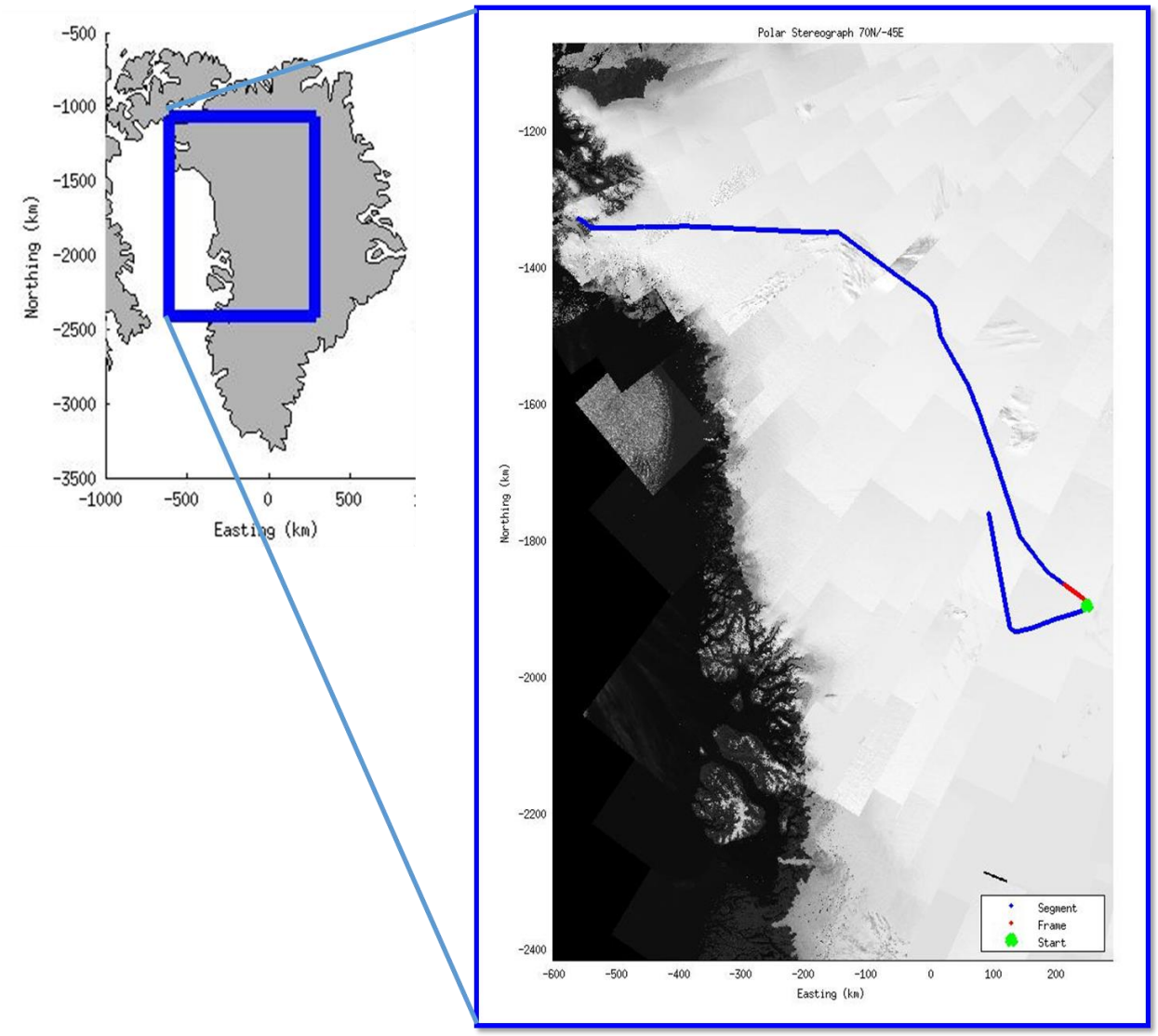

Figure 3-24: 20120330_03 frame 8 (*shown in red*).

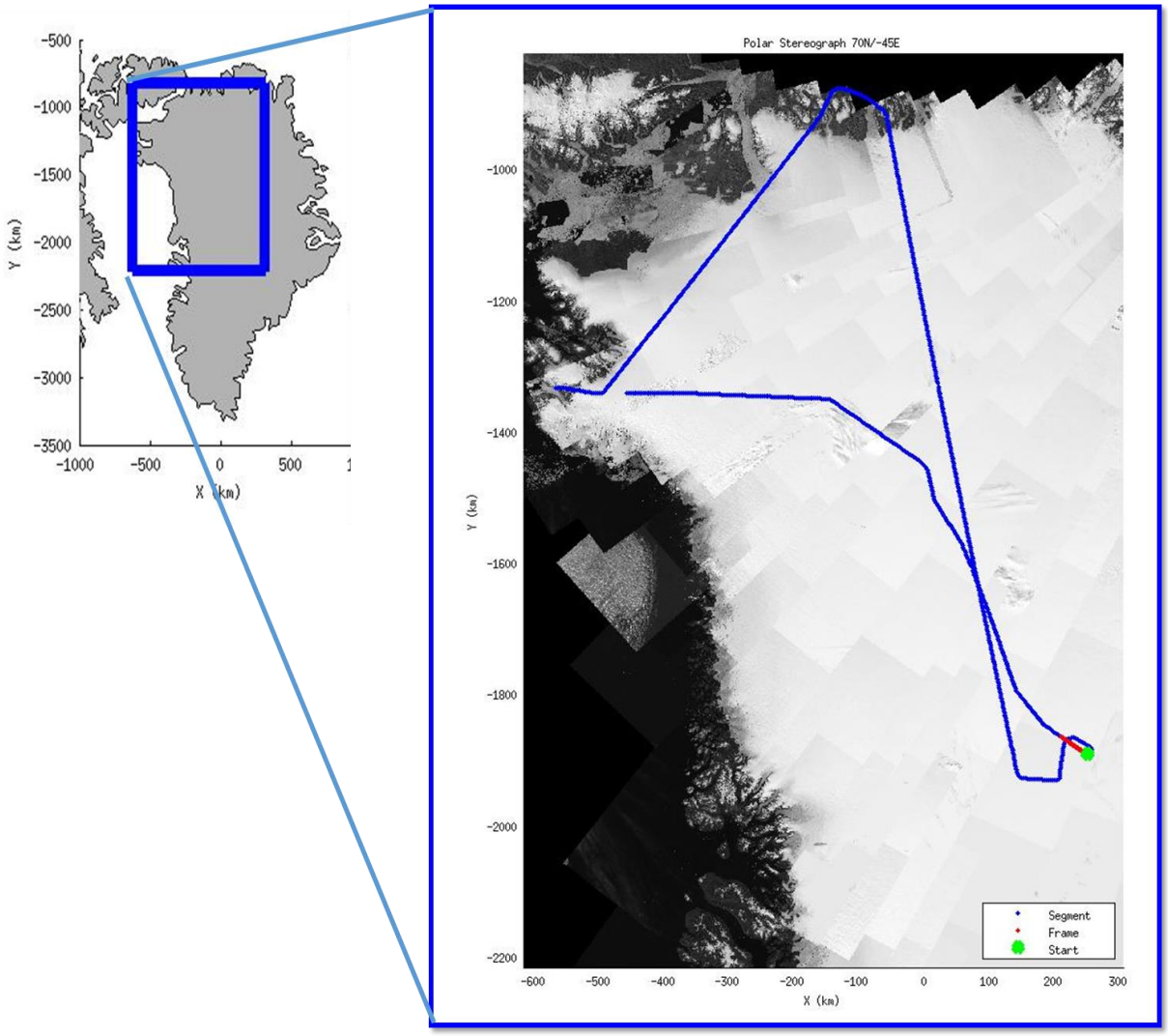

Figure 3-25: 20140502_01 frame 41 (*shown in red*).

3.4.3.1 MATLAB Implementation

The MATLAB implementation of the joint parameter estimation task uses a global optimization method. The optimization algorithm used is the Sequential Quadratic Programming (SQP) method, which is a type of nonlinear programming optimization method. The optimization finds the best set of parameters that minimizes the cost function for the given dataset.

The optimization is performed using the *fmincon* function, which is a built-in optimization function in MATLAB that solves constrained nonlinear optimization problems. The function requires an initial guess for the parameters (i.e., the lower and upper bounds for the parameters), and optimization options.

Then the MATLAB *GlobalSearch* function is used to perform a global search for the optimal solution. This function starts by performing several local searches in different parts of the parameter space and then combines the local solutions to find the global optimum. The function requires an optimization problem as an input.

The objective function is defined to calculate the cost or the error between the estimated data and the actual data.

The optimization problem is divided into small blocks of data, and the optimization is performed independently on each block using the same objective function. This approach is used to reduce the computational cost and allows for parallel processing of the optimization problem. The optimal parameters for each block are stored and interpolated to span the entire data.

Local minima can be a concern even when the cost function has a global minimum. If the optimization algorithm gets stuck in a local minimum, it may not find the global minimum. However, with Global optimization algorithms such as such as the globalsearch function in MATLAB, we can avoid getting stuck in local minima. These algorithms search the entire parameter space to find the global minimum rather than just searching for a local minimum. Analyzing the local minima of the cost function can help us understand the behavior of the optimization algorithm and identify potential improvements.

We perform a local minima analysis for grid values between -5 and 5 for optimization parameters, and we see that the cost function has a global minimum, as shown in Figure 3-26 to Figure 3-31.

For each of these figures, only two parameters are compared by evaluating the cost function at the grid values while keeping the rest of the parameters constant at the optimal values obtained during joint estimation.

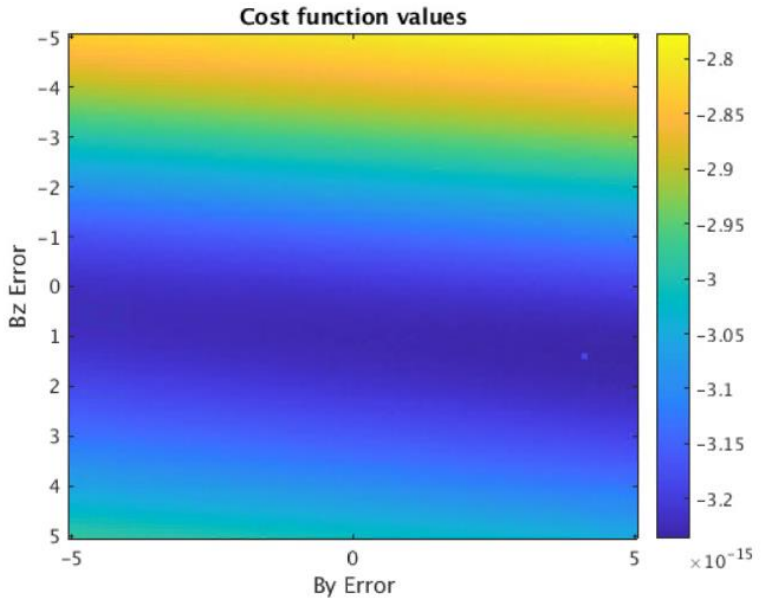

Figure 3-26: Cost function analysis for baseline errors.

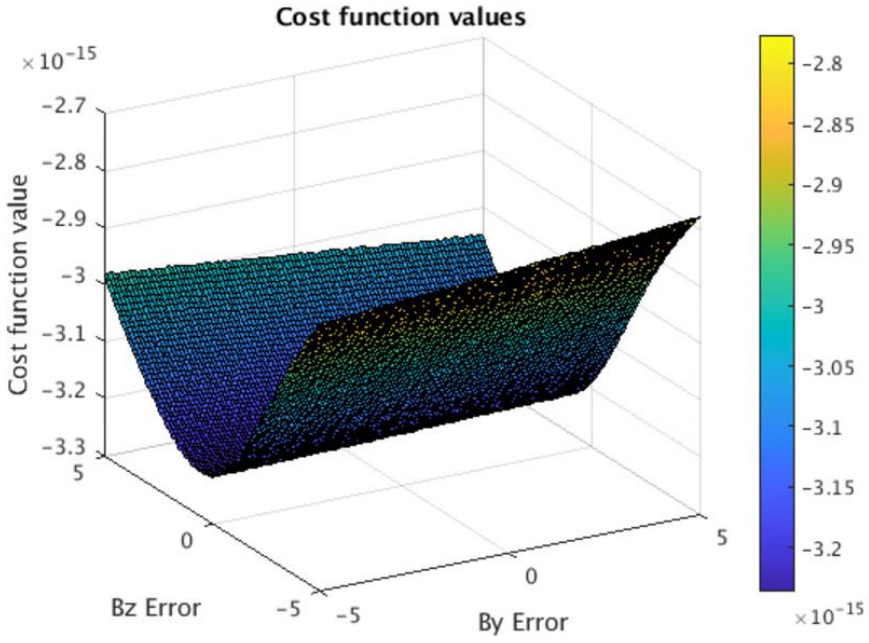

Figure 3-27: Cost function analysis for baseline errors (surface plot).

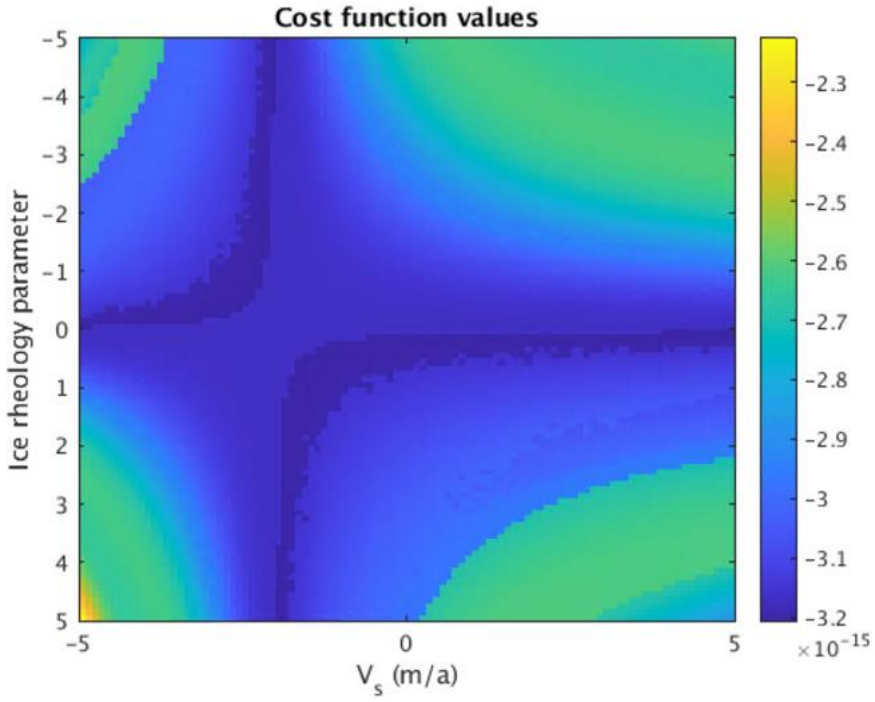

Figure 3-28: Cost function analysis for surface velocity and ice rheology parameter.

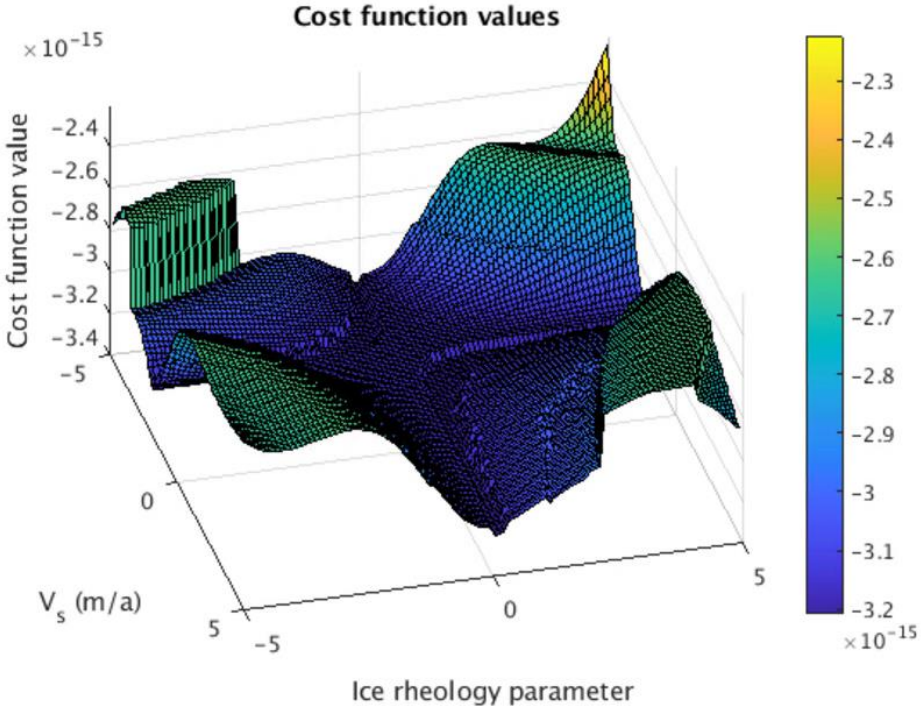

Figure 3-29: Cost function analysis for surface velocity and ice rheology parameter (surface plot).

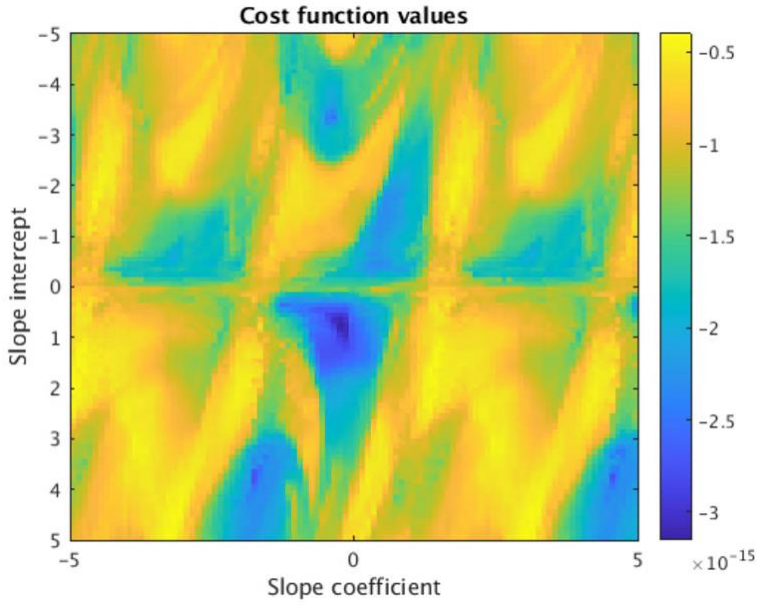

Figure 3-30: Cost function analysis for slope parameters.

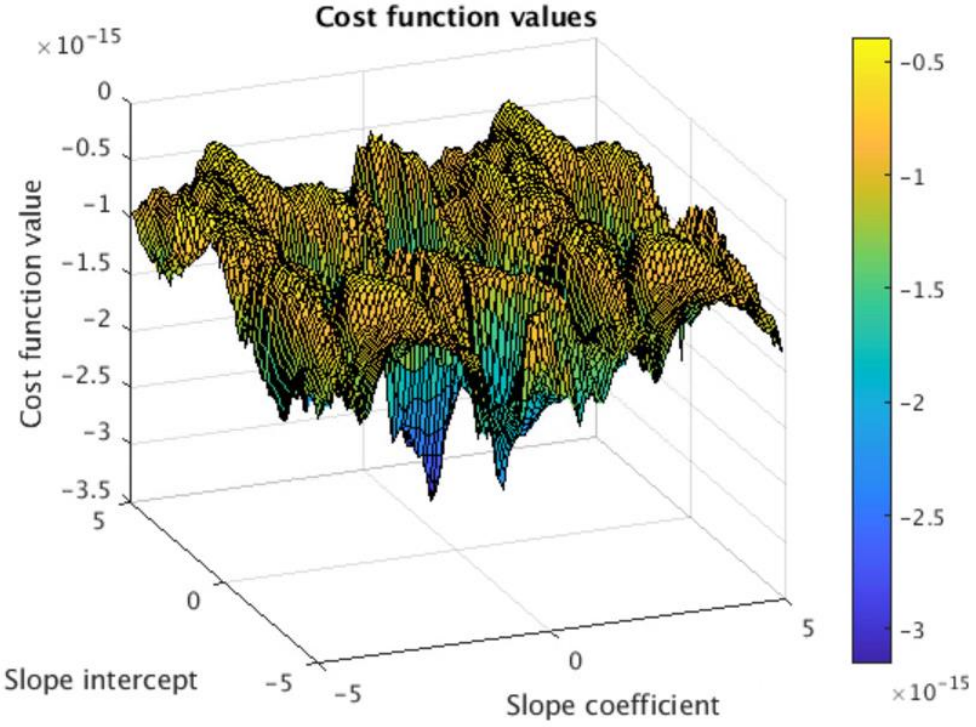

Figure 3-31: Cost function analysis for slope parameters (surface plot).

3.4.4 Joint Estimation Results

The joint estimation framework produces results for baseline errors, as shown in Figure 3-32 and Figure 3-33 for horizontal and vertical baseline, respectively. The baseline values are adjusted accordingly using these estimated baseline errors. This adjustment ensures that the range measurements are more accurate and can be used for further analysis or processing.

The rheology of ice refers to how ice deforms under stress, and it is an important parameter for understanding the flow of ice in glaciers and ice sheets. The joint estimation framework produces estimates of the ice rheology parameter which is used in the Lliboutry model.

Figure 3-34 shows the joint estimation results for vertical velocity for selected block columns. They all exhibit the predicted trend as per the Lliboutry model. These are averaged to generate the mean vertical velocity profile in Figure 3-35. The mean vertical velocity estimates are validated against the results from pRES estimation, which act as the ground truth for vertical velocity estimation (Section 3.4.5).

Figure 3-36 shows the joint estimation results for the cross-track slope for selected block columns. These are averaged to generate the mean cross-track slope profile in Figure 3-37. The mean cross-track slope estimates are validated against the results from crossover analysis which act as the ground truth for cross-track slope estimation (Section 3.4.6).

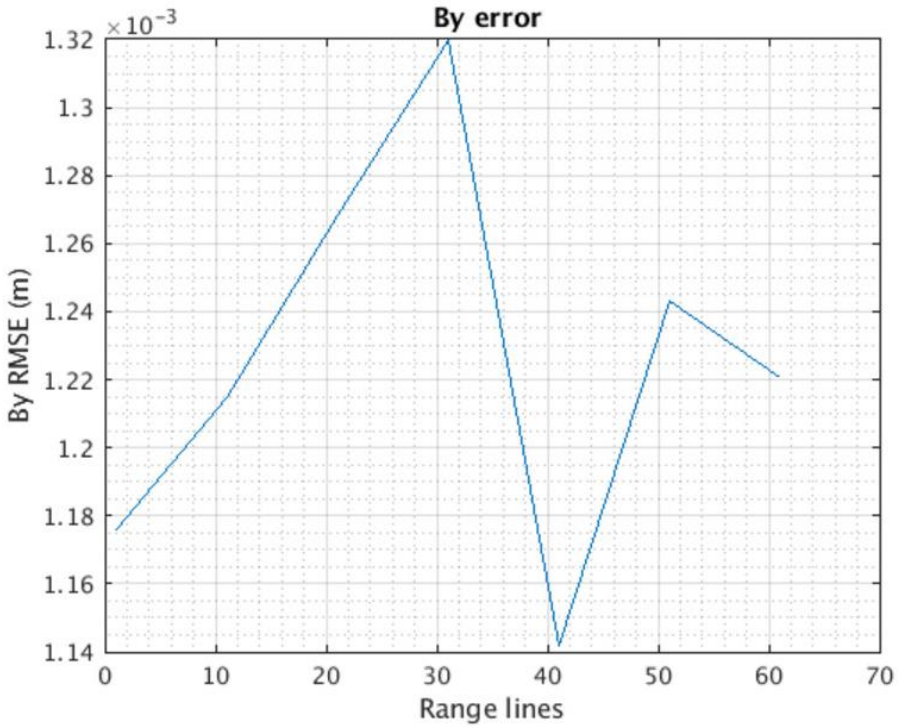

Figure 3-32: Estimated horizontal baseline error.

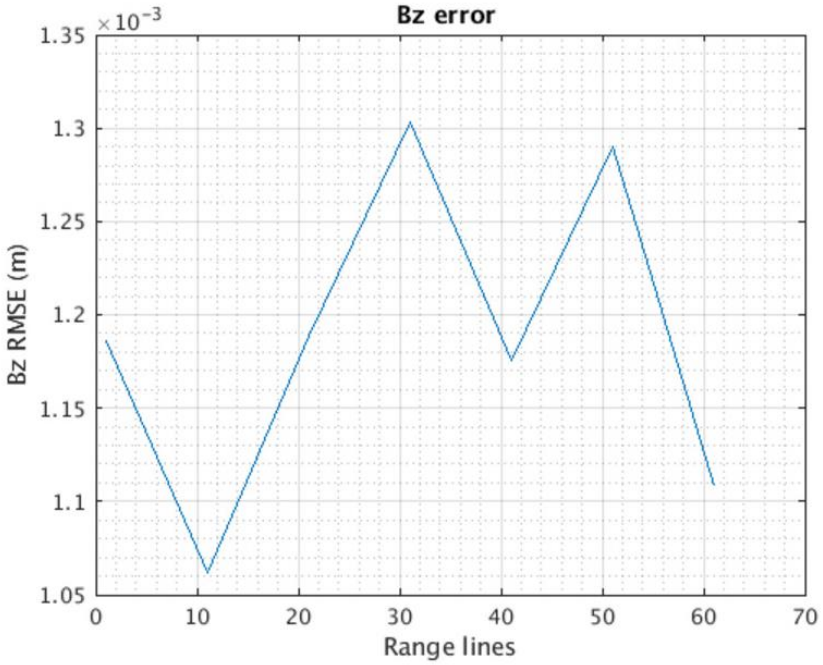

Figure 3-33: Estimated vertical baseline error.

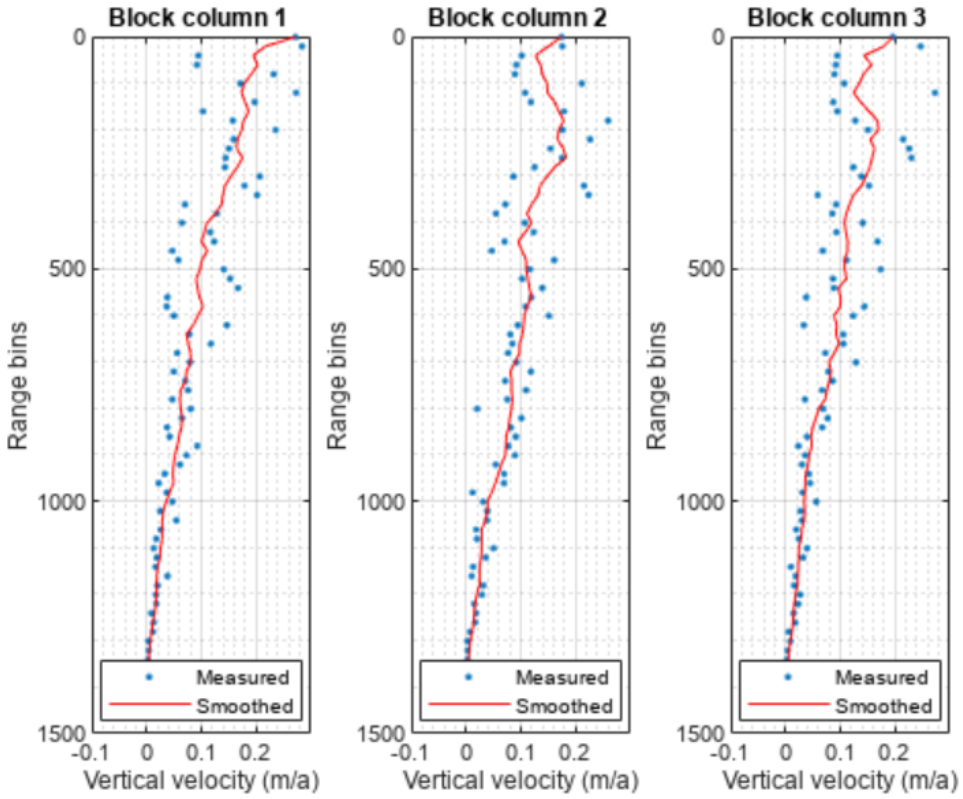

Figure 3-34: Vertical velocity joint estimation results for selected columns of blocks.

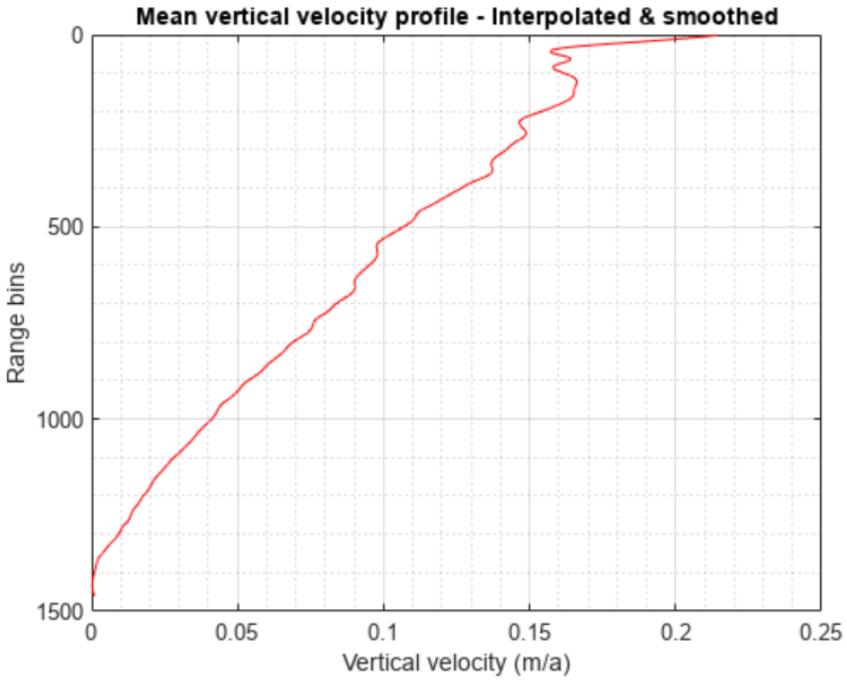

Figure 3-35: Averaged vertical velocity profile.

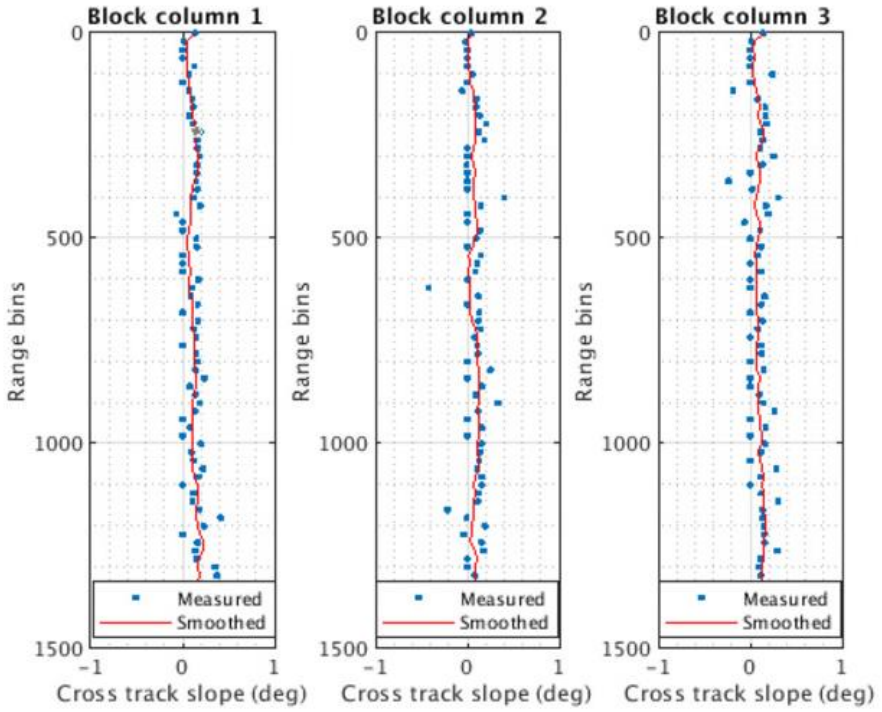

Figure 3-36: Cross-track slope joint estimation results for selected columns of blocks.

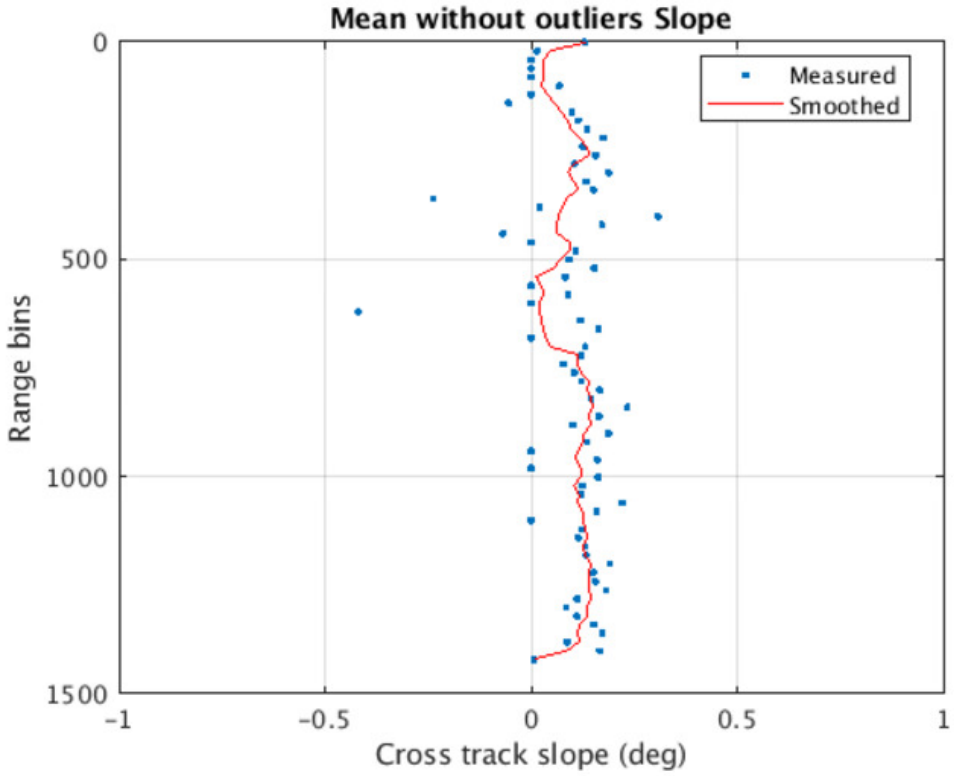

Figure 3-37: Averaged cross-track slope.

3.4.5 pRES Results for Vertical Velocity Estimation Validation

Vertical velocity estimates from pRES data around Summit (Figure 3-39) are used to compare with the results of vertical velocity from the joint estimation framework. The pRES results are taken as the ground truth because ground-based sensing systems like pRES can be precisely situated.

The process of generating vertical velocity estimates from pRES data follows the steps below:

- Load pulse compressed pRES data.
- Perform coregistration of the monitor (secondary) acquisition onto the base (reference) acquisition.
- Generate an interferogram between the two acquisitions.
- Use the unwrapped interferometric phase to calculate the displacement (Figure 3-38) between the two acquisitions using equation 3.17:

$$displacement = \phi \frac{\lambda}{4\pi} \tag{3.17}$$

  where λ is the pRES wavelength.

- Derive the vertical velocity (Figure 3-39) by dividing the displacement by the time span between acquisitions:

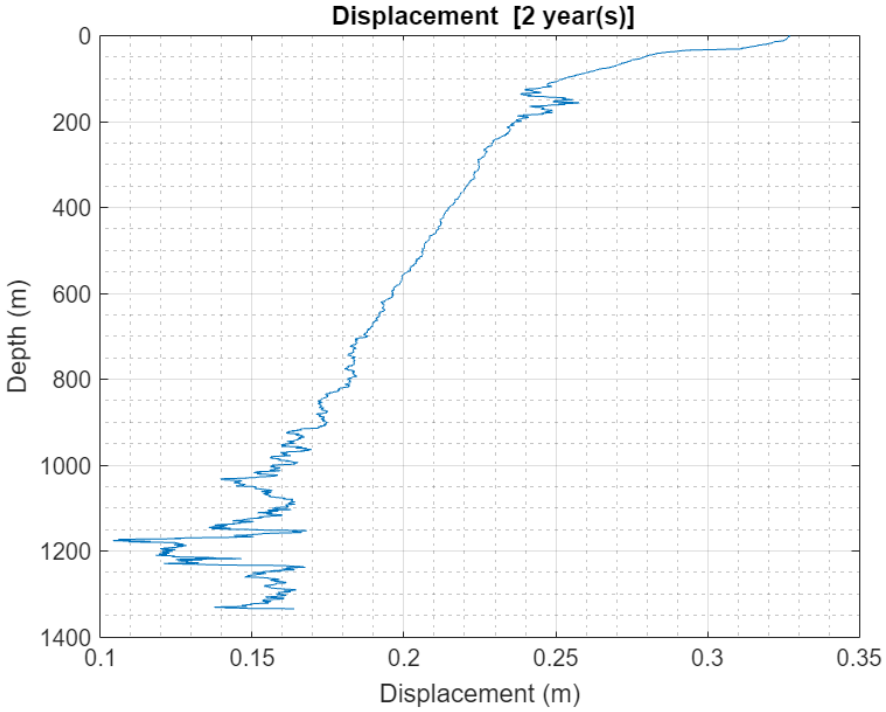

Figure 3-38: pRES displacement.

The vertical velocity profile generated from pRES data shows a reducing trend toward the bed rock as expected from Lliboutry's model. This result is used as the ground truth to evaluate the performance of the joint estimation framework in estimating the vertical velocity profile from airborne radar data as shown in Figure 3-40 and Figure 3-42.

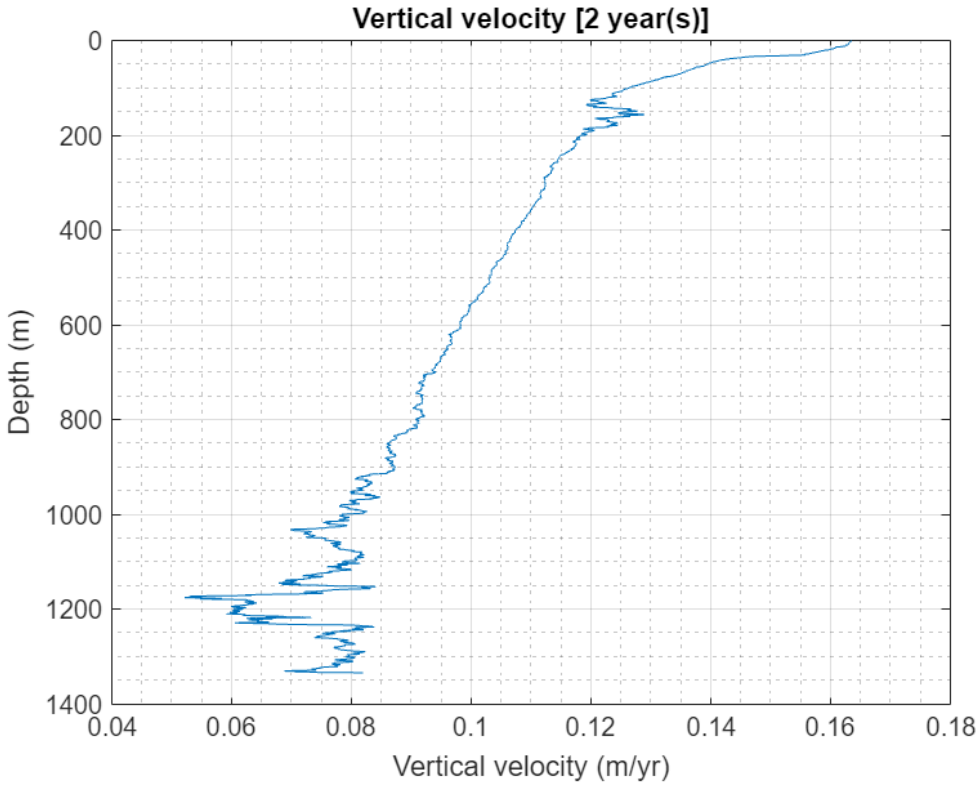

Figure 3-39: pRES vertical velocity estimation.

The temporal baseline between measurements for the pRES site was two years, and the corresponding vertical velocity estimate is shown in Figure 3-39. The vertical velocity estimates from the joint estimation framework and pRES are plotted together in Figure 3-40. We see that they both have the same gradient trend, and the corresponding error plot is shown in Figure 3-42. The errors near the surface (within the firn) and at depths beyond 1000 m have big error magnitudes due to the quality of data in these regions. From the magnified plots (Figure 3-41 and Figure 3-43), we see that the joint estimation results for vertical velocity matched those generated from the pRES data.

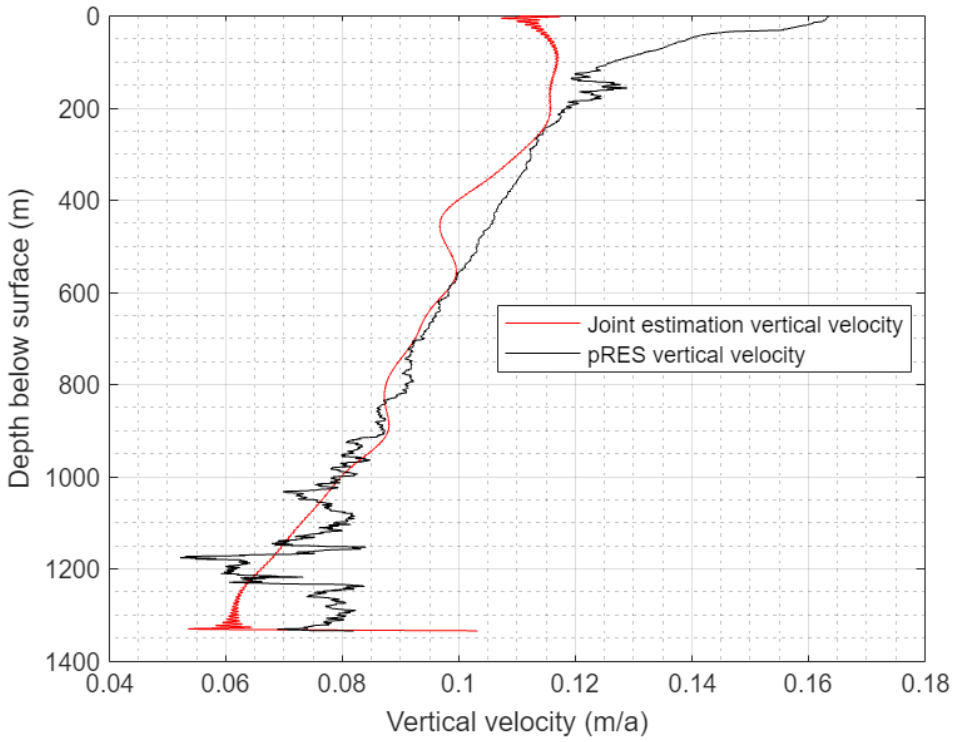

Figure 3-40: Validation of joint estimation vertical velocity results with pRES results.

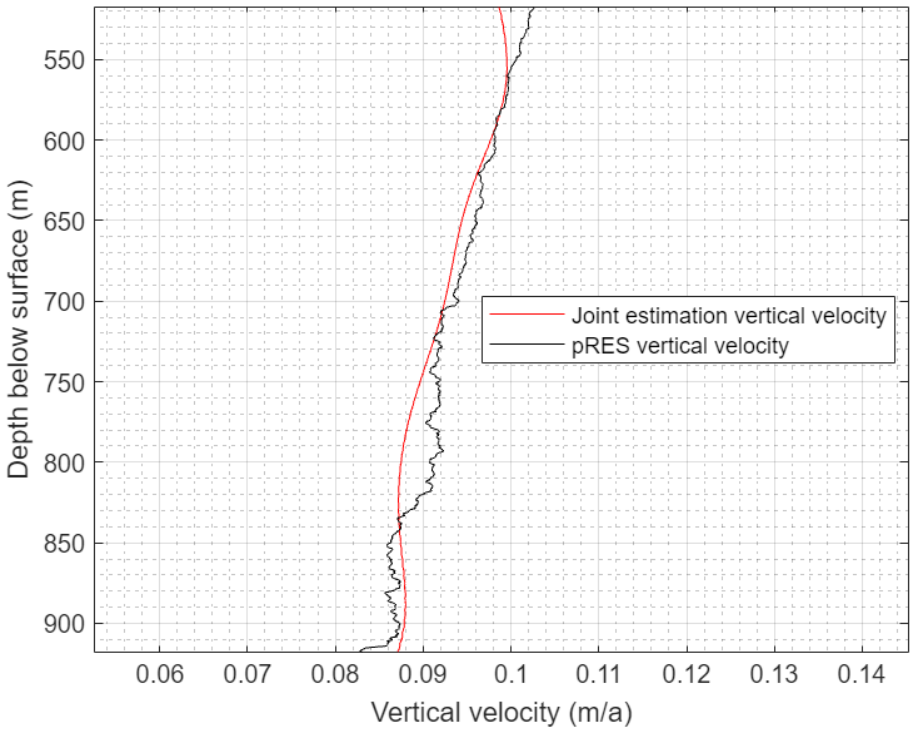

Figure 3-41: Validation of joint estimation vertical velocity results with pRES results (magnified).

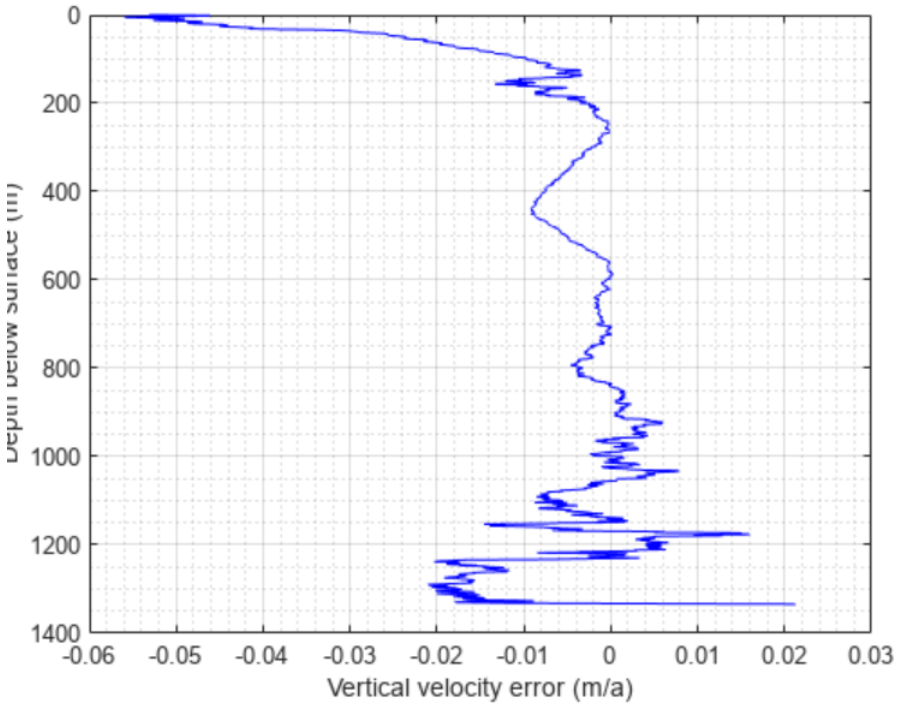

Figure 3-42: Error in vertical velocity estimation.

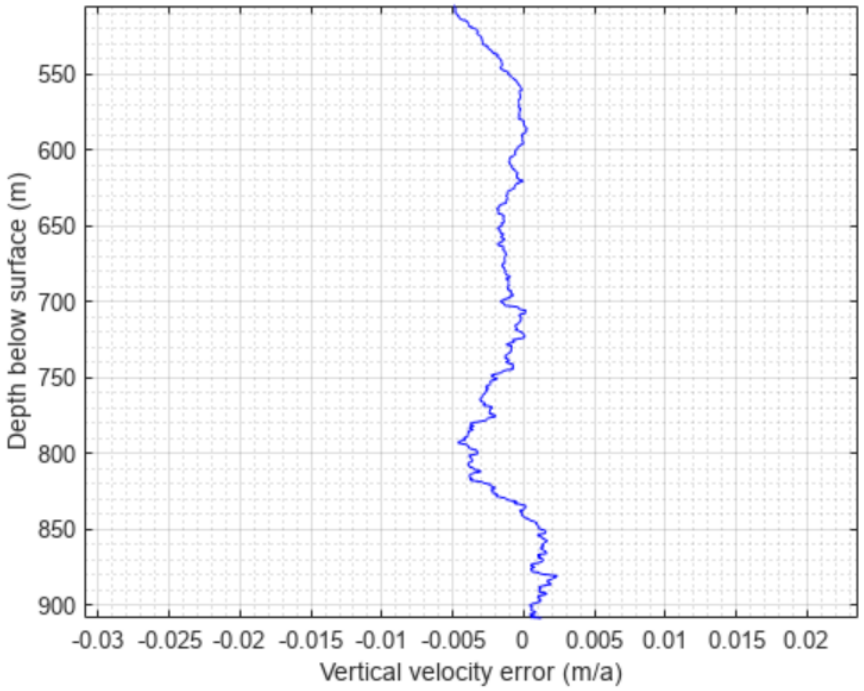

Figure 3-43: Error in vertical velocity estimation. (magnified).

3.4.6 Crossover Analysis for Slope Estimation Validation

Crossover analysis is the technique used to validate the accuracy of cross-track slope estimates obtained from the joint estimation framework. The technique involves comparing the slopes estimated from two radar tracks that intersect at a common location or crossing point. The rationale behind this technique is that if the slopes estimated from the two tracks are accurate, they should be consistent with each other at the crossing point. The crossing line needs to be at about a 90-degree angle to the primary line for the along-track slope of the crossing line to match the cross-track slope of the primary line. If the angle is too oblique, then this method does not work well.

We use crossover analysis as the ground truth to assess the accuracy of the joint estimation of the cross-track slope. The steps below outline the process of obtaining the slope using crossovers:

Obtaining Crossover Data: Crossover data refers to measurements taken by the radar depth sounder that flies over the same location at different times, creating a "crossover" point where the tracks intersect. The perfect crossover data is obtained when the tracks intersect at 90 degrees such that the along track slope of the crossing track at this point is aligned with the cross-track slope of the primary track.

Identification of Crossover Points: Identify the crossover points in the data where the aircraft flew over the same location at different times. This is done using the layer tracking tool developed by CReSIS for radar depth sounder data. The primary frame is 41 from the 201405_01 segment (Figure 3-25). Figure 3-44 shows the available crossovers that are over 80 degrees at the intersection. The dotted vertical line indicates the crossing point. We use frame 20180423_01_55, which is at 85.47 degrees and has the lowest error, as shown in Figure 3-44. The coordinates of the intersection are 72.668 N, -37.980 W. The range line values for the intersection are obtained from the layer tracking tool for both the primary and the crossover frame.

Estimate Cross-track Slope: Using the joint estimation framework, we estimate the cross-track slope as before and extract the cross-track slope as a function of depth at the specific crossing point.

Estimate Along-track Slope of the Crossing line: We extract data around the crossover point without a lot of variability in the slope profile in the crossover frame. We use two methods to estimate the along-track slope of the crossing line: manual and automatic.

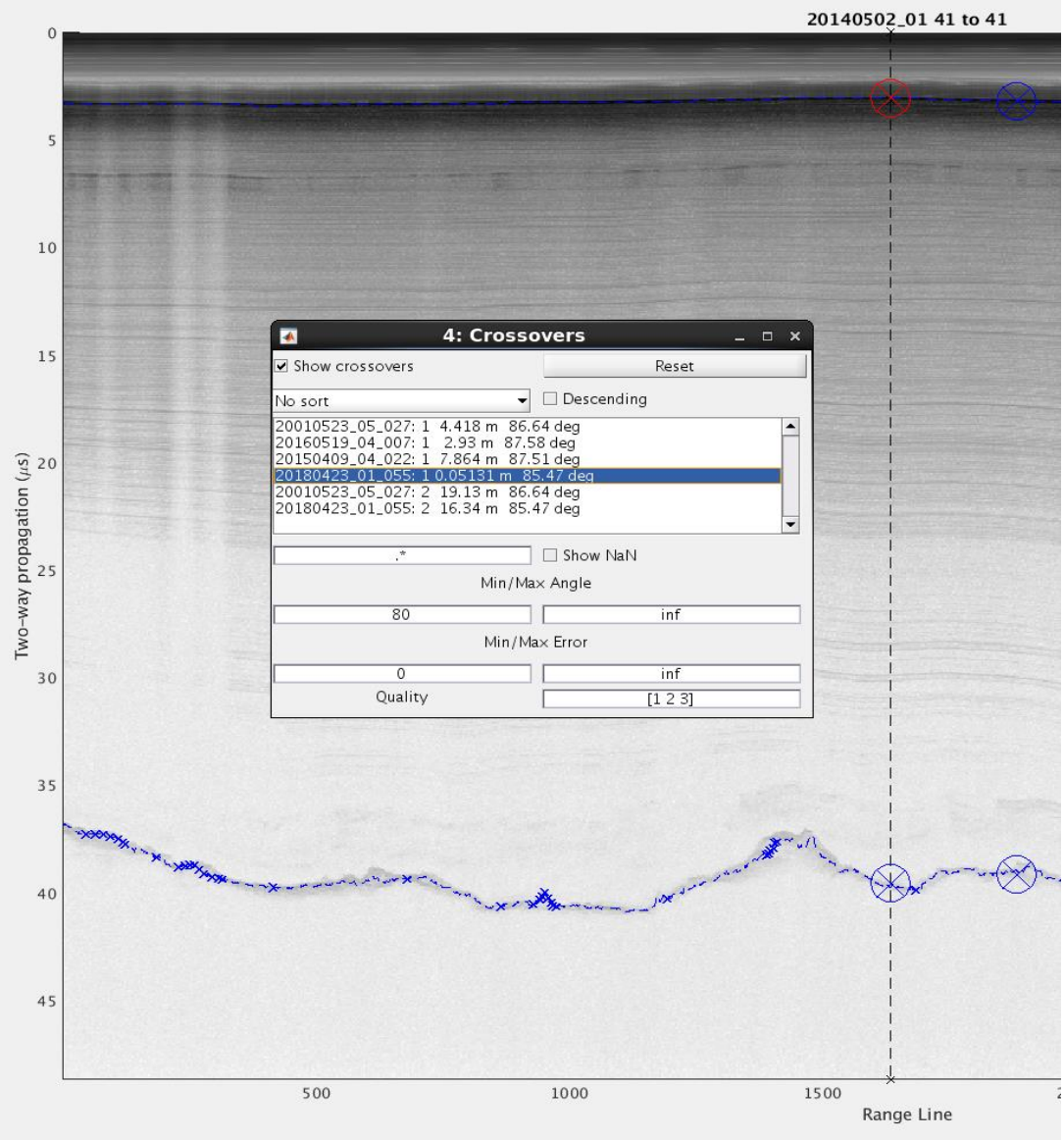

Figure 3-44: Crossover analysis in 20140502_01_41 frame.

3.4.6.1 Manual Crossover Analysis

Using frame 20180423_01_55, we manually track the layers (Figure 3-45) and calculate the along track slopes of the crossover frame at different depths (Table 3-2). This gives a rough estimate of the slope since the height change is manually picked with the cursor.

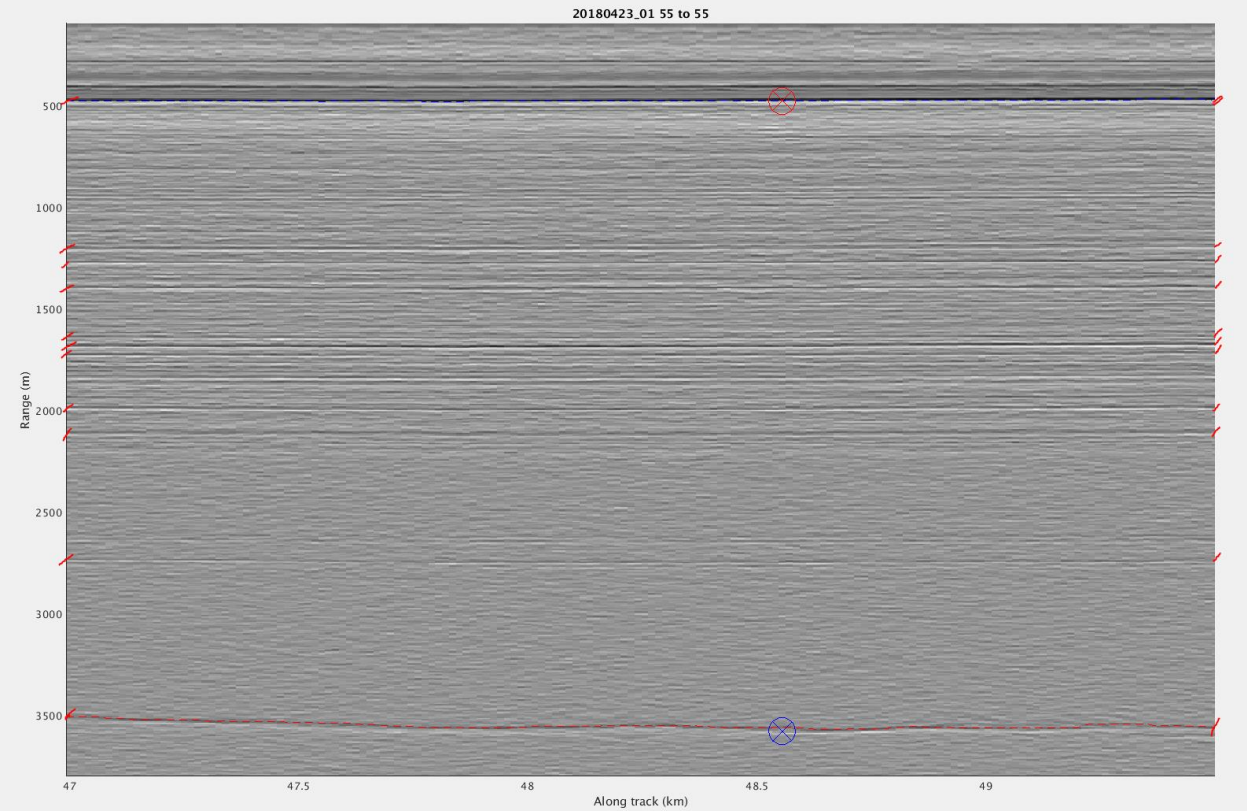

Figure 3-45: Manual tracking of depth change within the crossing line frame.

The manually obtained depth changes are tabulated in Table 3-2 and the corresponding along track slopes calculated. The comparison of the joint estimation cross-track layer slope results with the crossing line along-track layer slope calculation is shown in Figure 3-46 and Figure 3-47. We see that even with the rough along-track slope estimates, the joint estimation of cross-track layer slopes is not far off from the ground truth. These rough estimates also serve as inputs to constrain the joint estimation algorithm.

Table 3-2: Rough calculation of along-track slope by manually tracing the depth change.

Depth at 47 km along track (m)	Depth at 49.5 km along track (m)	Gradient (rad)	Slope (rad) [arctan(Gradient)]	Slope in degrees
474.476	470.603	-0.00155	-0.00155	-0.08876
1202.56	1198.65	-0.00156	-0.00156	-0.08961
1276.15	1268.4	-0.0031	-0.0031	-0.17762
1400.08	1396.2	-0.00155	-0.00155	-0.08892
1640.19	1636.32	-0.00155	-0.00155	-0.08869
1682.79	1675.05	-0.0031	-0.0031	-0.17739
1729.26	1717.65	-0.00464	-0.00464	-0.26608
1992.62	1981	-0.00465	-0.00465	-0.26631
2732.32	2728.45	-0.00155	-0.00155	-0.08869
3506.88	3561.1	0.021688	0.021685	1.242436

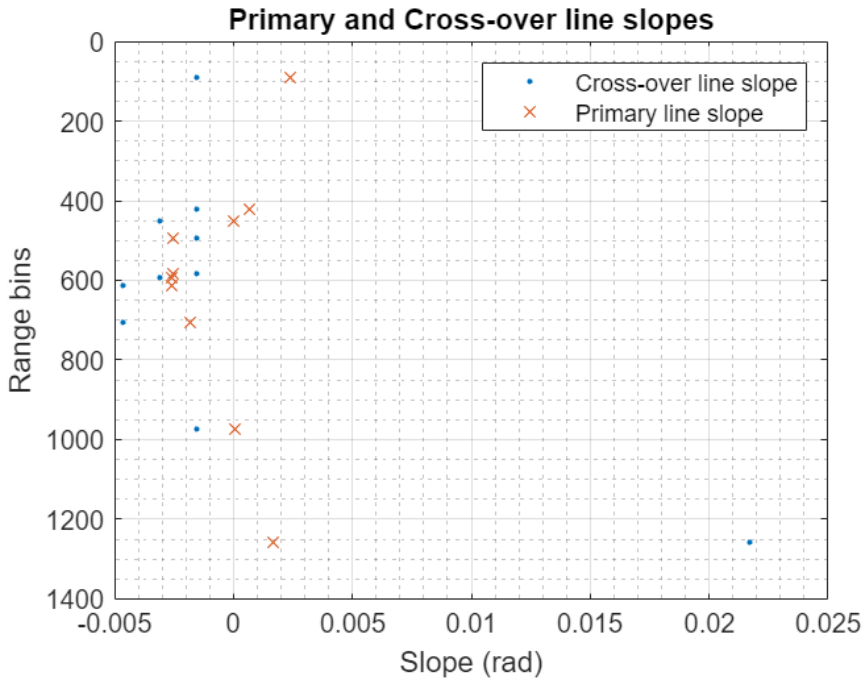

Figure 3-46: Crossover analysis to validate the cross-track slope estimate from the joint estimation framework.

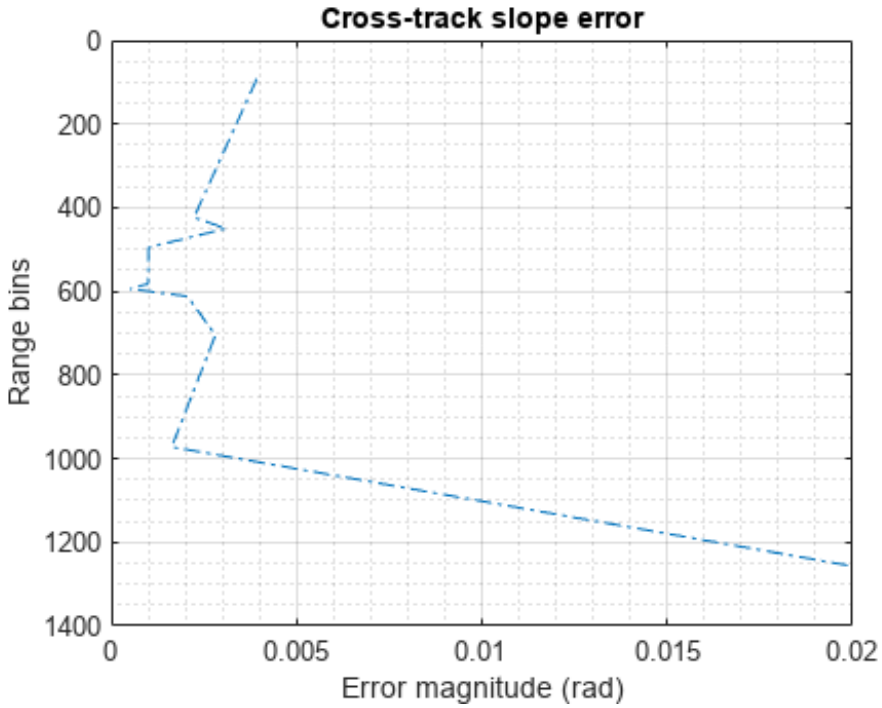

Figure 3-47: Error in the cross-track slope estimate from the joint estimation framework.

3.4.6.2 Automatic Crossover Analysis

To automate and to obtain better estimation of the along track slope in the crossing line, we have developed the process where we use the phase ramp within the along-track FFT filter coefficients and a Constant False Alarm Rate (CFAR) detector. The CFAR detector is an algorithm that is capable of estimating the noise variance for a specific range cell, known as the cell under test (CUT), by analyzing data from adjacent range cells that serve as training cells. This method assumes that the noise characteristics of the training cells are similar to those of the cell under test. Additionally, the CFAR detector assumes that the training cells are free from any target signals, and that the data in the training cells only consist of noise. Buffer cells, or guard cells, are included between the CUT and the training cells to prevent signal leakage into the training cells, which may adversely affect the estimation of the noise variance. Furthermore, the training cells should be selected from ranges that are not too distant from the CUT, as illustrated in Figure 3-48. The CFAR method used is the greatest-of-cell-averaging.

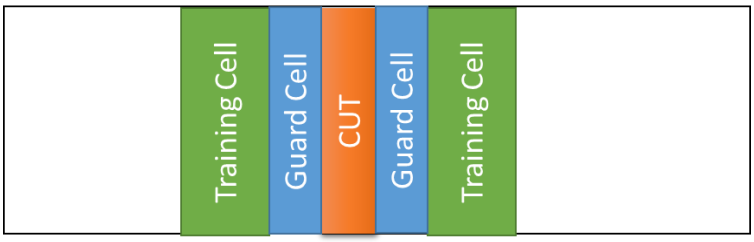

Figure 3-48: CFAR structure (*credit: Mathworks*).

The automatic along-track process follows the steps below:

- Load radar data.
- Determine the number of range lines before and after the crossing point reference line based on the size of the data matrix and layer roughness.

- Perform coherent noise removal and also remove DC components by averaging in the along-track dimension.
- Compute FFT (with oversampling) of the extracted data along each along–track row and convert the output to power (the square of absolute values).
- Apply a 2D filter to average in the fast-time domain.
- Apply the CFAR filter in the fast-time dimension to remove clutter.
- Find the index of maximum magnitude in each row in the along-track dimension.
- Compute the FFT coefficients that account for the phase shift due to the slope and calculate the phase shift, $\Delta\phi$, corresponding to the index of maximum magnitude (idx_{max}):

$$\Delta\phi = \ -j2\pi\frac{idx_{max}}{N}, \tag{3.18}$$

where N is the size of the FFT.

- Convert the phase shift to range shift, d_r, by dividing it by the wavenumber:

$$d_r \ = \frac{\Delta\phi}{k_r}, \tag{3.19}$$

where $k_r \ = \ 4\,\pi/\lambda$.

- Finally, convert the range shift to slope by dividing the range shift by the along-track spacing (dx):

$$slope = arcsin\left(\frac{d_r}{dx}\right) \quad 3.20$$

This along-track slope (3.20) is compared with the joint estimation cross-track slope result.

We use the CReSIS Qlook[2] script to load data for frames 55 and 56 of the 20180423_01 segment and combine them. We use two frames because the crossing point within frame 55 is near the end of the frame, and to allow for about 1000 range lines around the crossing point, we need to combine the two frames. We select 1000 range lines around a crossing point and compute the FFT (Figure 3-49) of the data in the along-track dimension. CFAR (Constant False Alarm Rate) filtering is applied to the Fourier-transformed data to remove clutter (Figure 3-50). The index of the maximum magnitude in the FFT is used to calculate the phase change (Figure 3-51) in the data. The phase change is directly proportional to the along-track slope. The plot of the estimated along-track slope around the crossing point is shown in Figure 3-52.

[2] https://ops.cresis.ku.edu/wiki/index.php/Qlook

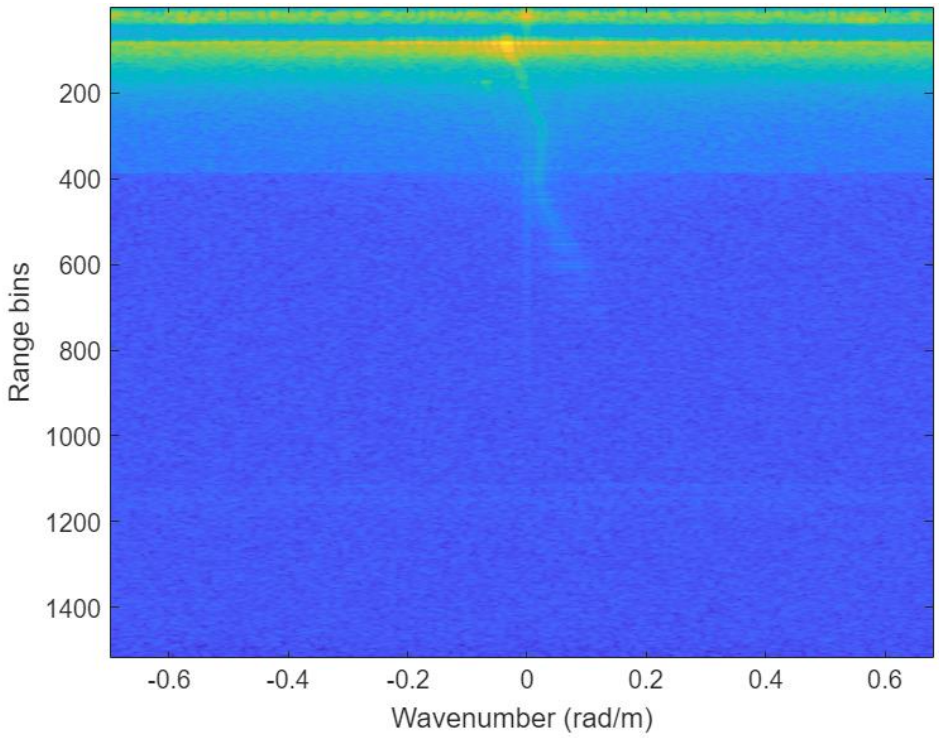

Figure 3-49: Azimuth FFT around the crossing point.

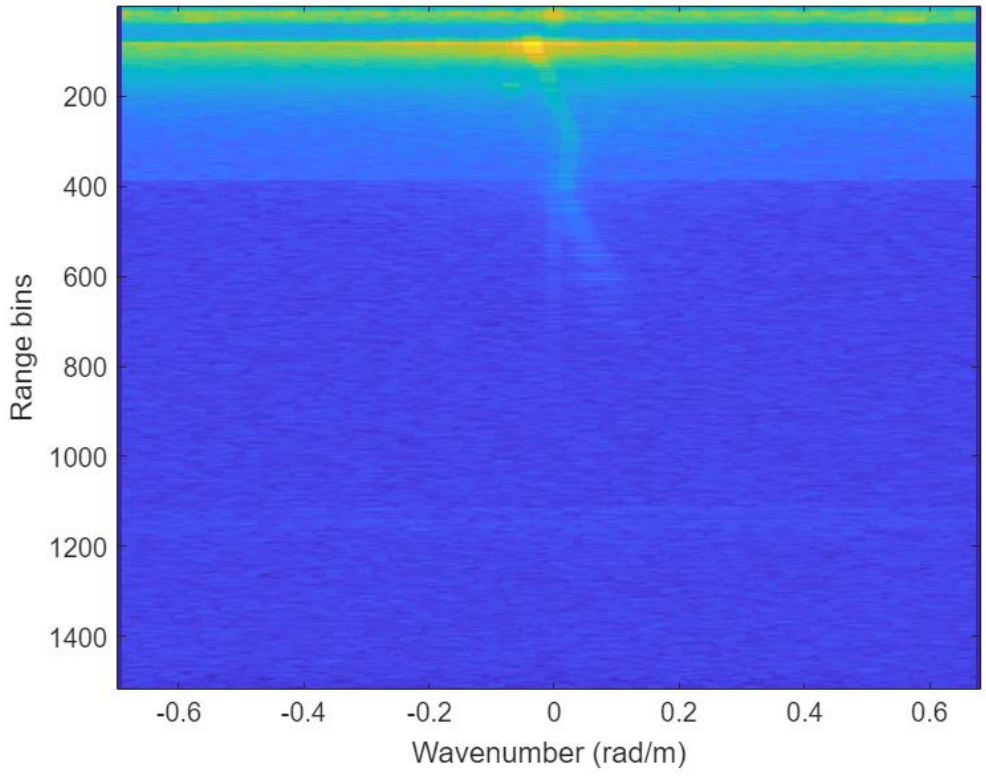

Figure 3-50: CFAR detection.

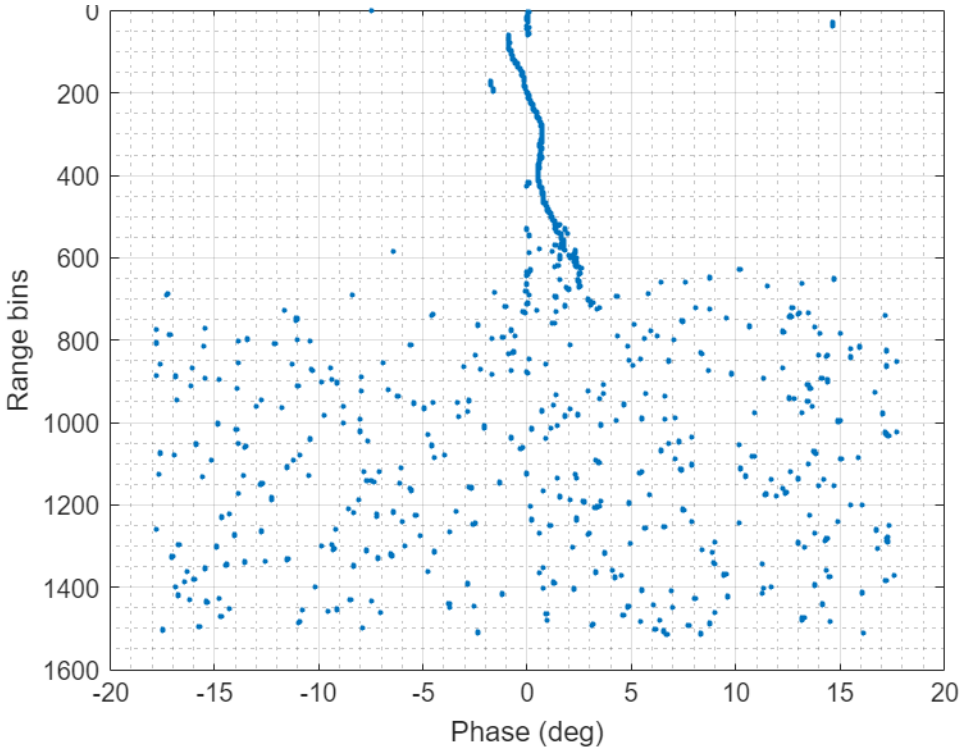

Figure 3-51: Crossline along-track phase change.

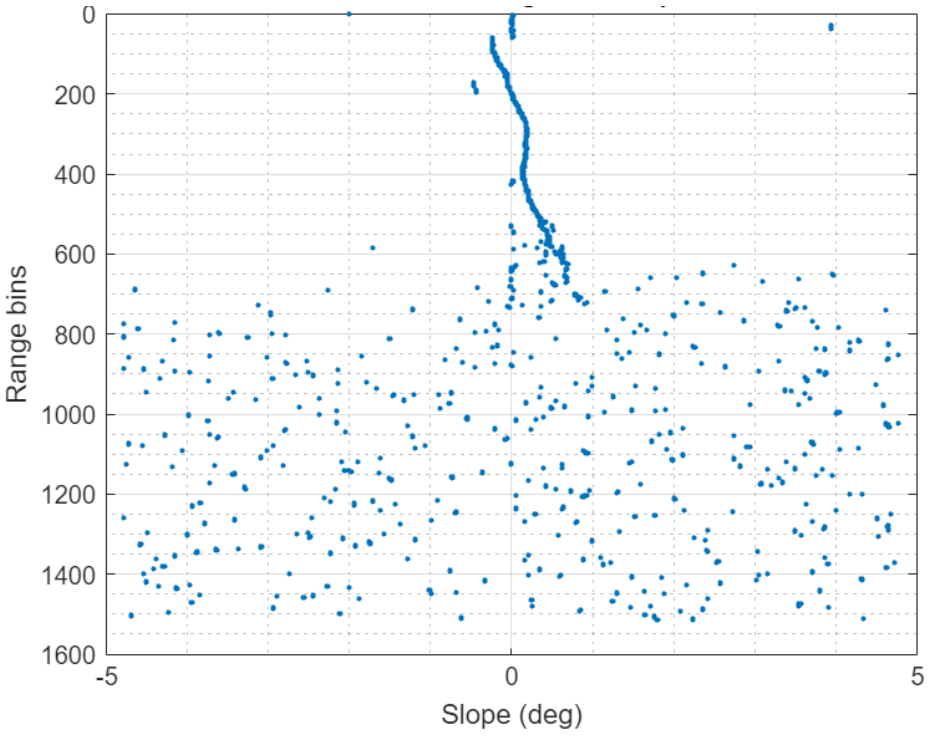

Figure 3-52: Crossline along-track slope.

Figure 3-52 shows the estimated along-track slope at the crossing point in degrees. The slope represents the change in elevation with respect to the along-track direction of the radar. The accuracy of the slope estimation is poor below range bin 600 because the layers at these depths are not clearly imaged (poor data quality). The error between the joint estimation slope values and the corresponding along-track slope estimates gives an indication of the accuracy of the joint estimation algorithm for the cross-track slope variable.

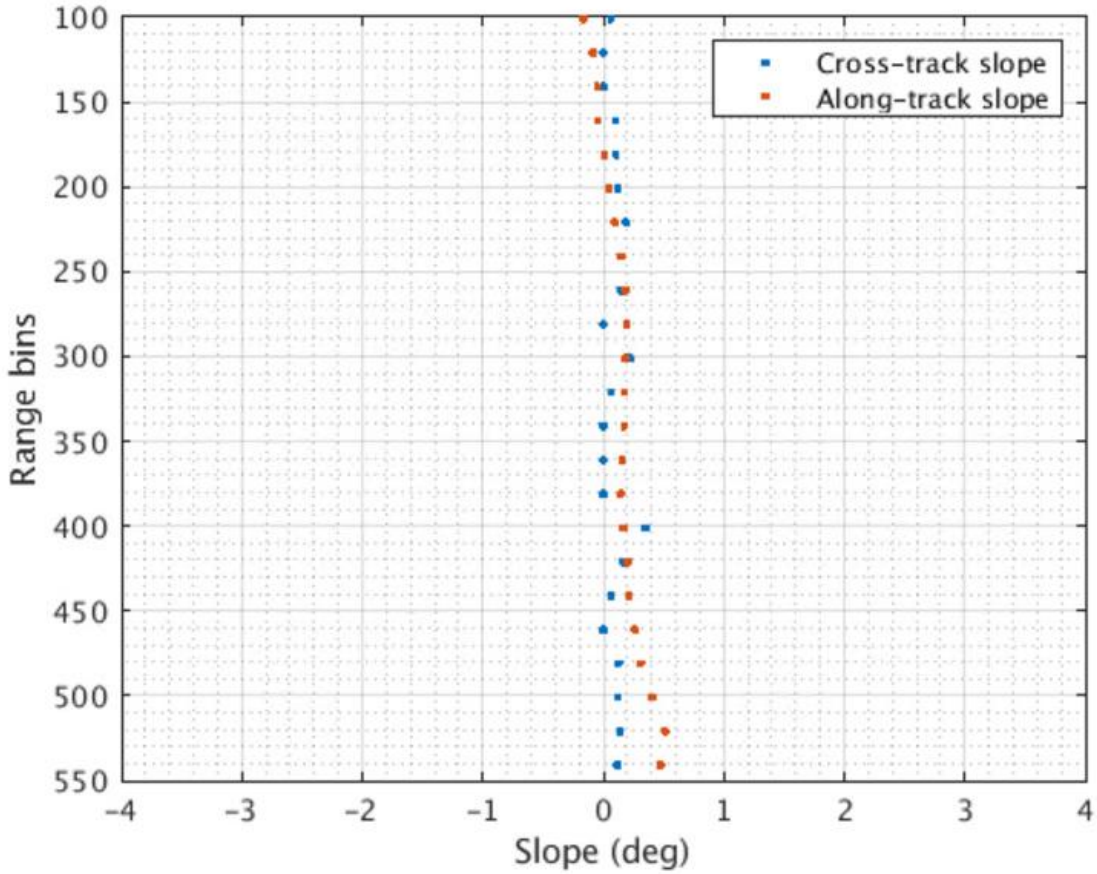

Figure 3-53: Validation of cross-track slope with along-track slope from crossover analysis.

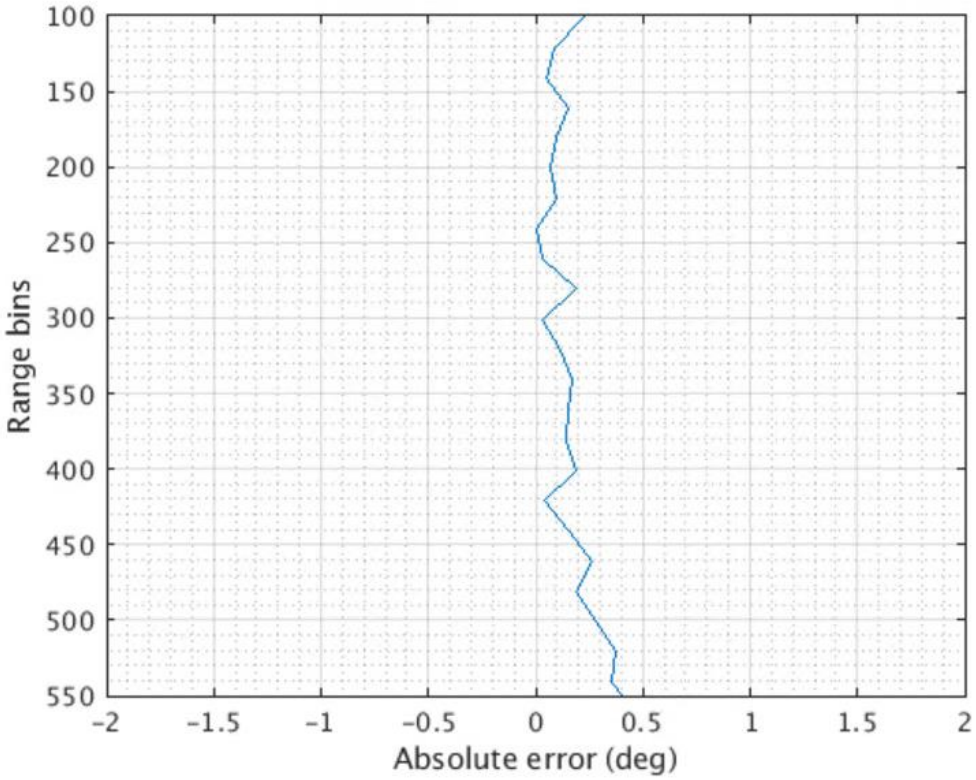

Figure 3-54: Absolute error in estimating the cross-track slope.

The absolute error between the good range bins shows that the joint estimation of the cross-track slope was very close to the along-track slope estimate.

3.4.7 Inter-Waveform Equalization

Multiple (usually two or three) waveforms of varying durations and gains are required to reliably image the surface, inner layers, and ice bottom. The images corresponding to each waveform are formed and then combined to form one composite image, as illustrated in Figure 3-55 for frame 20140405_01_001 from the 2014 Greenland campaign. Due to changes in the radar settings for each waveform, the system impulse response is slightly different for each waveform.

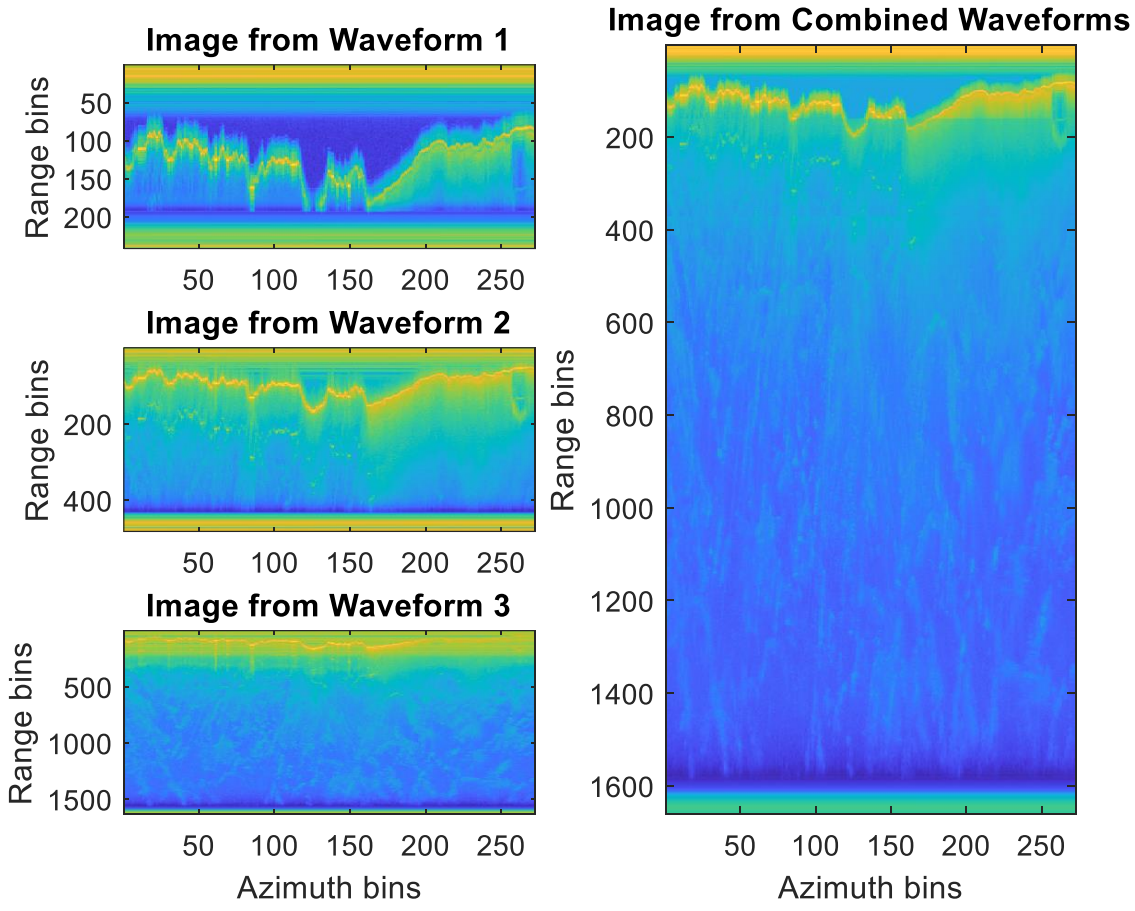

Figure 3-55: Three images (waveform 1 focused on the surface, waveform 2 focused on the near-surface internal layers, and waveform 3 focused on the deep internal layers and ice bottom) create the combined image on the right.

The interferometric phase plot between the two different passes is expected to be a smooth and continuous curve when the SNR is high. However, there can be inter-waveform phase and amplitude discontinuities at the waveform transitions especially if the passes are from different radar configurations where the waveform transitions of the two passes do not coincide. For example, if pass one used three waveforms and pass two used two waveforms. The combined image may have discontinuities corresponding to each inter-waveform transition. For passes from

the same radar configuration with the same settings, the waveform transitions occur concurrently so the interferometric phase is continuous, as illustrated in Figure 3-56 (a). If waveform transitions occur at different points in the equalization record or the change between waveforms varies, then fast-time discontinuities in the interferometric phase will occur as illustrated in Figure 3-56 (b).

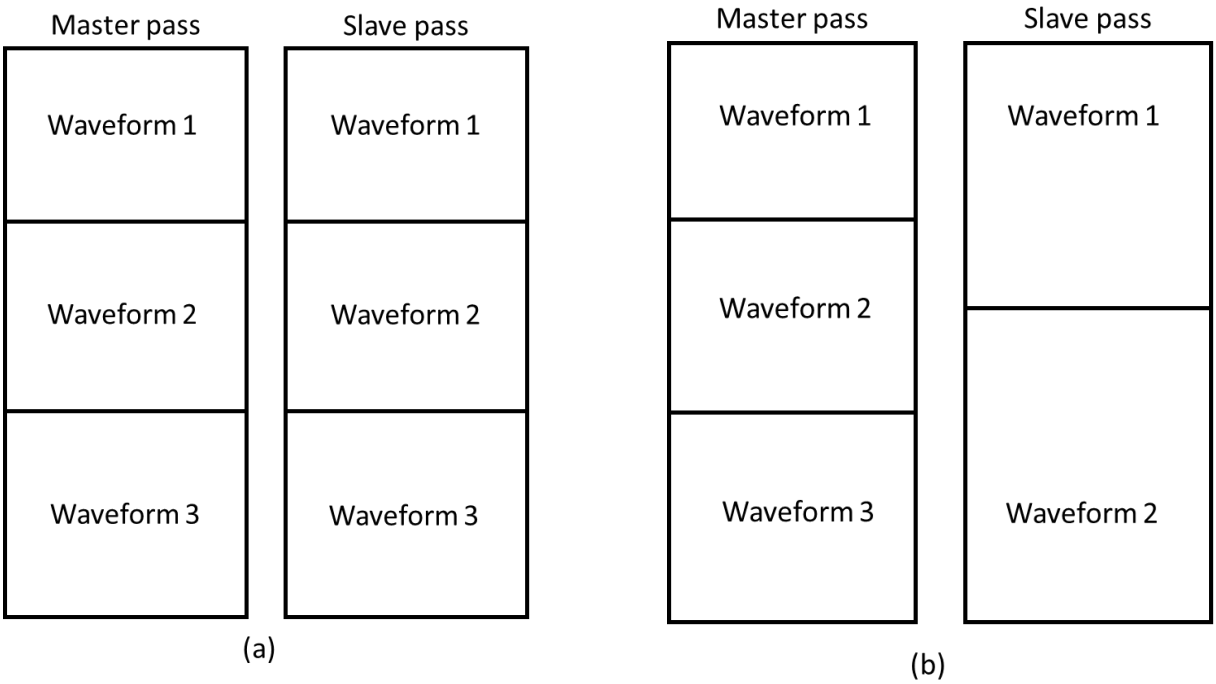

Figure 3-56: (a) Concurrent inter-waveform transition between passes. (b) Discontinuities can occur due to the master pass transitions from waveform 1 to waveform 2 and waveform 2 to waveform 3.

When processing radar data, equalization is employed to abate errors induced by the non-ideal system hardware. These errors modify the magnitude and phase response of the received waveforms. The current equalization process accounts for relative errors between the ADC channels but not relative errors between the waveforms.

Equalization will be implemented using two approaches to mitigate these waveform-to-waveform discontinuities. Both methods involve finding a complex coefficient for each waveform to multiply the corresponding waveform by, such that unwanted system variations between waveforms are eliminated.

The first method is to apply a complex coefficient correction to each waveform by finding the optimal offset that causes the least root mean square fitting error to the interferogram phase model derived from the Lliboutry (1979) ice sheet velocity model at the waveform-to-waveform transition in the interferograms. This method is applicable to inter-waveform transitions that don't have an overlapping region at the transition (as illustrated in Figure 3-57) and therefore no common target between the waveforms. This lack of sufficient overlap between waveforms leads to gaps in the resulting interferograms.

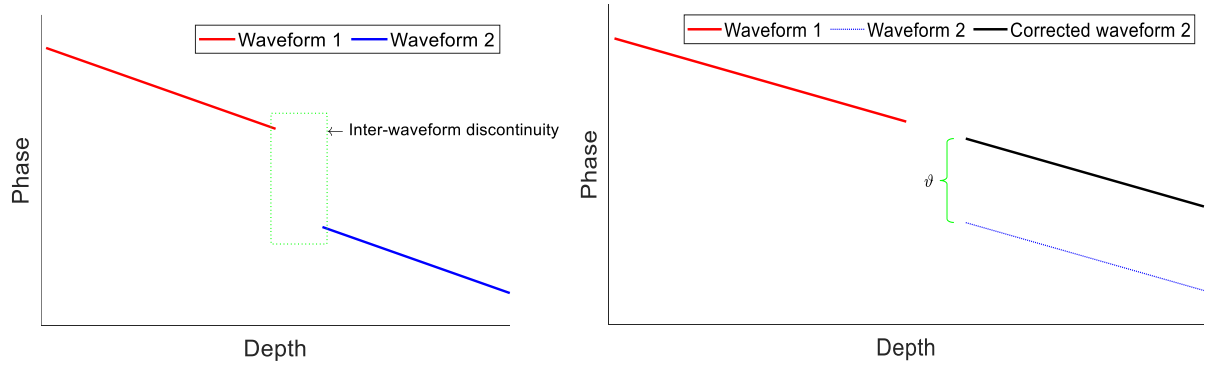

(a) (b)

Figure 3-57: (a) Inter-waveform phase discontinuity illustration with no overlapping region. (b) Inter-waveform phase discontinuity correction.

To correct for the discontinuity, such that waveform 2 as illustrated in Figure 3-57 follows the trend of waveform 1, a complex number that eliminates the discontinuity is estimated. Due to the

expected smoothness (trend) of the phase, it is possible to take the measurement from the waveform 1 region and estimate what it should be in the waveform 2 region near the transition. Then a multiplicative scaling complex coefficient is applied to waveform 2 to shift it to the right value and remove the discontinuity as illustrated by the black line in Figure 3-57.

The second approach is to estimate equalization coefficients by tracking an internal layer at the transition when waveforms overlap so that both waveforms measure the same internal layer and then use this common target to find a coefficient that makes the measurements from each waveform as consistent as possible. The coefficient is estimated by averaging the complex ratio of waveform 2 to waveform 1 scattering in the overlapping region. The random phase from the SAR processed data for two waveforms is illustrated by the sketch in Figure 3-58 (a) where we have an inter-waveform transition region that overlaps (waveform 1 – red and waveform 2 – blue). This means that the waveforms capture the same target in this overlapping region in fast-time and the corresponding phase due to the scatterers in the overlap region should be the same (ignoring thermal noise) in both instances since the radar system and the scene are the same. The multiplicative scaling coefficient of the form $g \cdot e^{j\vartheta}$ is applied to waveform 2 to shift it to the right value and remove the discontinuity as shown by the black waveform in Figure 3-58 (b). g

represents the relative amplitude change and ϑ the relative phase change between the passes at the transition region for the common target.

We assume that the complex coefficient estimates for method 1 and method 2 are constant as a function of time such that all pixels in the overlap region for a segment (i.e., many range bin - range line combinations) can be used to estimate the single complex equalization coefficient.

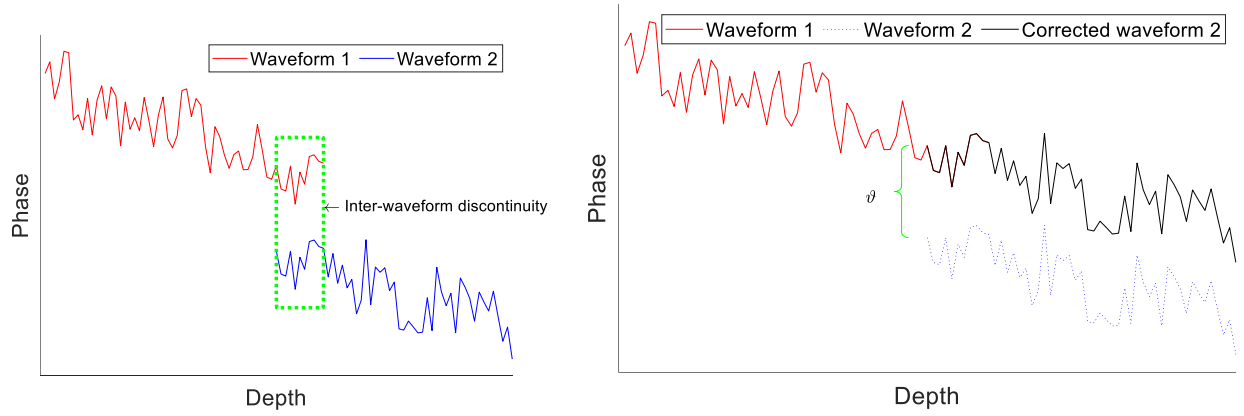

Figure 3-58: (a) Illustration of inter-waveform discontinuity when both waveforms measure the same target. (b) Interferogram phase after inter-waveform phase discontinuity correction.

3.4.7.1 Inter-Waveform Equalization Results

The averaged phase for waveform 1 and waveform 2 before inter-waveform equalization is shown in the plot of Figure 3-59. We see a discontinuity around the range bin 280 to 300. This is compensated for, and Figure 3-60 shows the averaged phase after inter-waveform equalization, and the discontinuity around the range bin 280 to 300 has been eliminated. Furthermore, the vertical velocity profile plot (Figure 3-62) after the inter-waveform equalization does not have the kink evident in the pre-equalization plot (Figure 3-61).

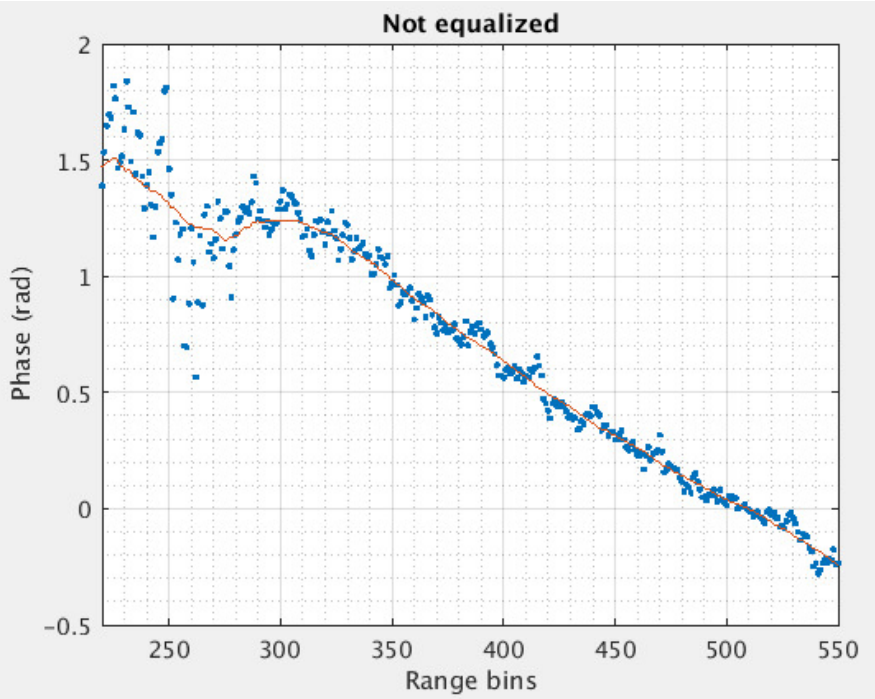

Figure 3-59: Averaged phase without inter-waveform equalization between waveform 1 and waveform 2.

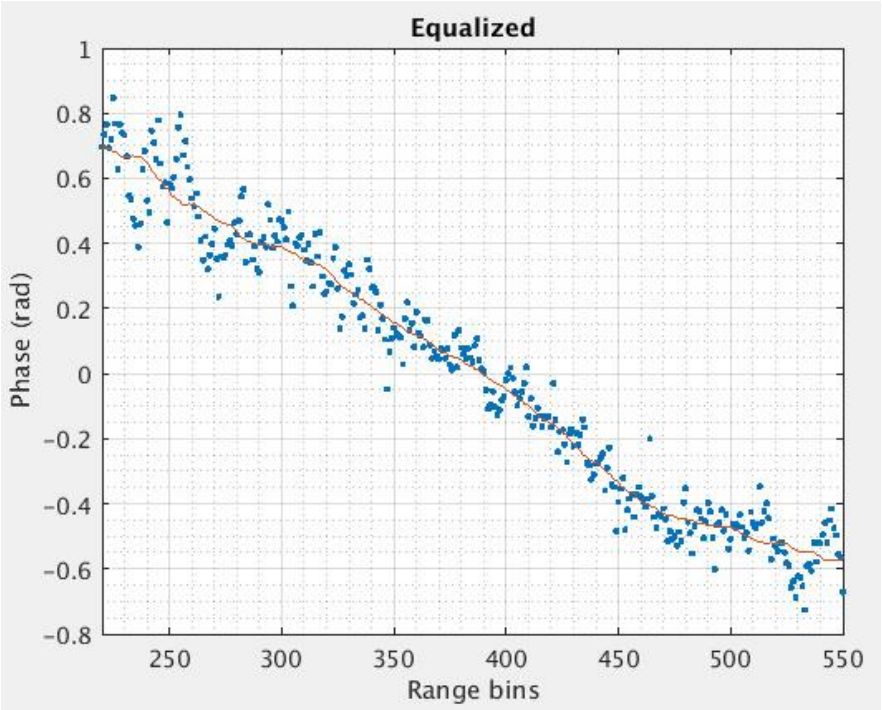

Figure 3-60: Averaged phase after inter-waveform equalization between waveform 1 and waveform 2.

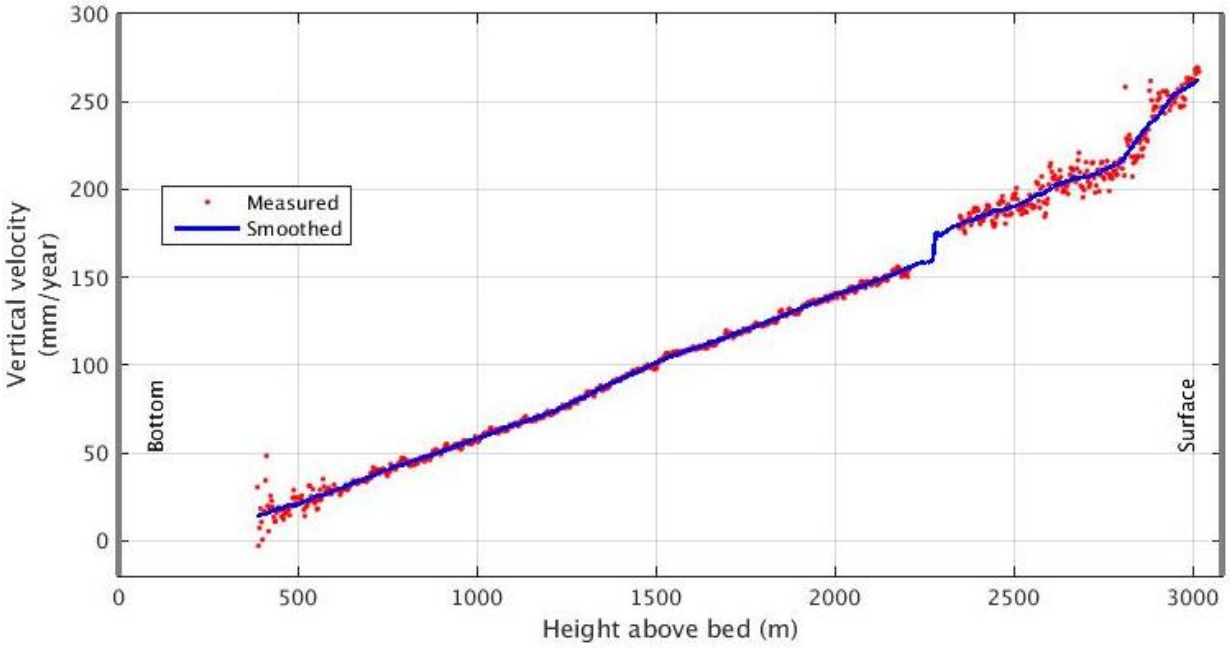

Figure 3-61:Vertical velocity profile without inter-waveform equalization.

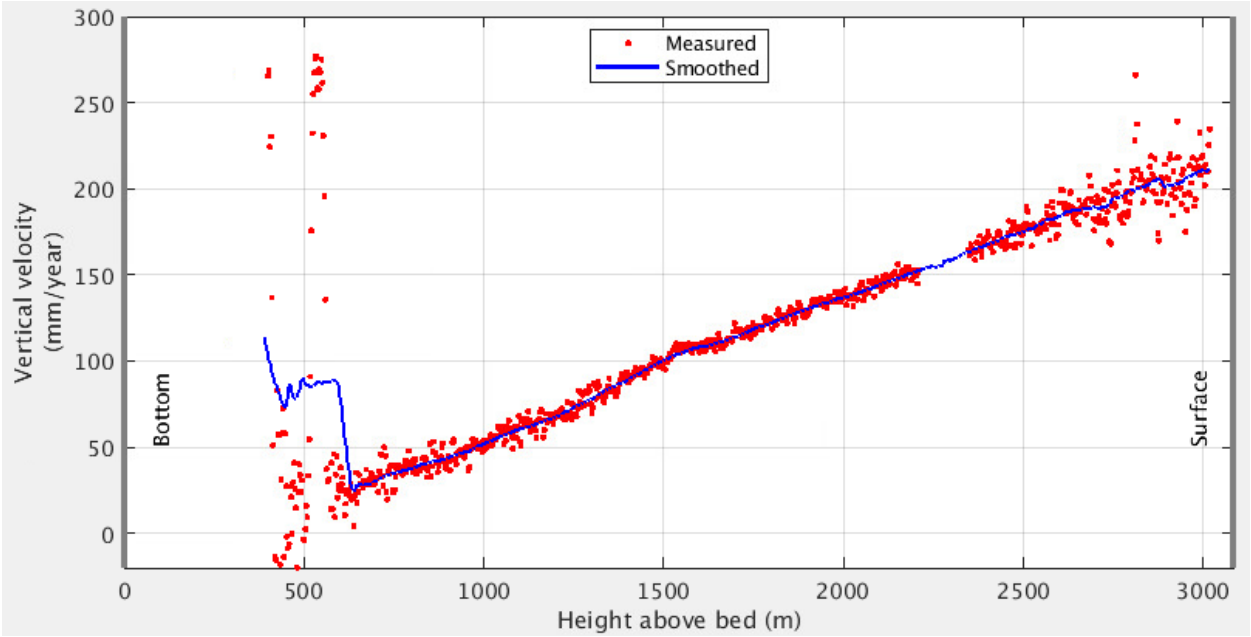

Figure 3-62:Vertical velocity profile after inter-waveform equalization.

4 FOCUSING MATRICES

4.1 Introduction

As discussed in section 2.5.5.2, transformation or focusing matrices are used to coherently combine sub-bands. This process provides improved results over incoherent wideband DOA methods [27]. The focusing matrices transform the signal subspace of each sub-band in the wideband signal into the reference frequencies signal subspace. The DOA estimation is then carried out via narrowband signal processing. The challenge is to design the optimal focusing matrices that can do this transformation appropriately. From Equation 2.51, we can see that the angles defining the steering vectors that form the matrices $\boldsymbol{A}(\omega_k)$ and $\boldsymbol{A}(\omega_0)$ are unknown, which creates a challenge in defining the focusing matrix $\boldsymbol{T}(\omega_k)$. In this report we shall focus on rotational signal subspace (RSS) focusing matrices that were shown to be effective in [55].

4.2 Problem formulation

To deal with the problem of unknown steering angles, we build candidate steering matrices denoted by $\boldsymbol{B}(\omega_k)$ that use initial DOA estimates such that $\boldsymbol{T}(\omega_k) = \boldsymbol{B}(\omega_0)\boldsymbol{B}(\omega_k)^{-1}$. The matrix $\boldsymbol{B}(\omega_k)$ is of size $P \times P$. For RSS focusing matrices, rather than making the candidate matrices to be $P \times P$, the following constrained minimization is done:

$$\text{minimize } \| \boldsymbol{B}(\omega_0, \boldsymbol{\alpha}) - \boldsymbol{T}(\omega_k)\boldsymbol{B}(\omega_j, \boldsymbol{\alpha}) \|_F \qquad 4.1$$

$$\text{subject to } \boldsymbol{T}(\omega_k)^H \boldsymbol{T}(\omega_k) = \boldsymbol{I}$$

where $\boldsymbol{\alpha}$ is a set containing angles, obtained before the estimation process, that define the steering vectors of $\boldsymbol{B}$. $\boldsymbol{\alpha}$ contains the angles $\{\theta_q, \theta_q - 0.25 * bandwidth, \theta_q + 0.25 * bandwidth\}$ for $q > 1$. These focusing angles can be preliminary DOA

estimates from a beamformer. The solution to Equation 4.1 is detailed in [55] and is given by;

$$\boldsymbol{T}(\omega_k) = \boldsymbol{V}(\omega_k)\boldsymbol{U}(\omega_k)^H \quad 4.2$$

where $\boldsymbol{V}$ and $\boldsymbol{U}$ are the left and right singular vectors of $\boldsymbol{A}(\omega_k, \boldsymbol{\alpha})\boldsymbol{A}(\omega_0, \boldsymbol{\alpha})^H$.

4.3 Review of Prior Work

Maximum likelihood (ML) and signal subspace approaches are prominent methods for direction of arrival finding in array signal processing. The signal subspace methods in contrast to maximum likelihood, do not require a slow nonlinear iterative search which also poses a risk of not converging to the desired solution due to many local minima [56]. The signal subspace methods in wideband scenarios are classified as either incoherent or coherent. The incoherent processing category involves the decomposition of the wideband signal into narrowband components. Each non-overlapping narrowband component is then subjected to narrowband signal subspace processing to obtain preliminary estimates which are averaged to yield the final estimate [56].

Wang and Kaveh in [27] proposed the application of focusing matrices in coherent signal subspace processing for DOA estimation of wideband sources. The signal subspaces of the narrowband components of the wideband signal are aligned using focusing matrices. To perform parameter estimation, one reduced covariance matrix is generated by combining the focused narrowband covariances.

4.4 RSS Focusing Matrices

To implement RSS focusing matrices, a wideband signal model was developed for *P* sensors, *Q* sources, *K* sub-bands, and *M* snapshots in MATLAB as follows:

$$\boldsymbol{X}_m(f_k) = \boldsymbol{A}_\theta(f_k)\boldsymbol{S}_m(f_k) + \boldsymbol{N}_m(f_k) \qquad k = 1, \dots K \text{ and } m = 1, .., M \qquad 4.3$$

where f is the ordinary frequency which is related to angular frequency by $f = \omega/2\pi$, $\boldsymbol{X}_m\,(f_k) = [x_{1m}\,(f_k), x_{2m}(f_k), \cdots x_{Pm}(f_k)]^T$ is the discrete Fourier coefficients of the received signal, $\boldsymbol{S}_m\,(f_k) = \left[S_{1m}\,(f_k), S_{2m}(f_k), \cdots S_{Qm}(f_k)\right]^T$ is the discrete Fourier coefficients of the unknown signal radiated by the q^{th} source, $\boldsymbol{N}_m\,(f_k) = [N_{1m}\,(f_k), N_{2m}(f_k), \cdots N_{Pm}(f_k)]^T$ is the discrete Fourier coefficients of the additive noise received at the p^{th} sensor, $\boldsymbol{A}_\theta(f_k) = \left[\boldsymbol{a}_{\theta 1}(f_k), \boldsymbol{a}_{\theta 2}(f_k), \cdots \boldsymbol{a}_{\theta q}(f_k)\right]$ is the $P \times Q$ steering matrix, and $\boldsymbol{a}_{\theta q}(f_k) = \left[e^{-j2\pi f \tau_1(\theta_q)}, e^{-j2\pi f \tau_2(\theta_q)}, \dots e^{-j2\pi f \tau_P(\theta_q)}\right]^T$ is the steering vector.

Here we note that for a Uniform Linear Array (ULA) $\tau_p(\theta_q) = \frac{(p-1)d}{c}\sin(\theta_q)$ with d, θ_q , and c referring to sensor separation, arrival angle, and speed of light respectively. For the case of arbitrary array, the delay is given by Equation 2.15.

With the signal model implemented, the RSS focusing matrix described above was constructed by following three stages:

- Computation of $\boldsymbol{A}_\theta(f_k)\boldsymbol{A}_\theta^H(f_o)$
- Computation of the left $\boldsymbol{U}(f_k)$ and right $\boldsymbol{V}(f_k)$ singular vectors[3] of $\boldsymbol{A}_\theta(f_k)\boldsymbol{A}_\theta^H(f_o)$.
- Computation of the RSS focusing matrix $\boldsymbol{T}_\theta(f_k) = \mathbf{V}(f_k)\boldsymbol{U}(f_k)^H$

[3] SVD reference: https://web.mit.edu/be.400/www/SVD/Singular_Value_Decomposition.htm

The algorithm for applying focusing matrices in wideband DOA estimation is outlined below. Householder Signal Subspace Transformations (HSST) that are well explained in [56], are included for comparison.

- Construct the signal model.
- Use MVDR-S to estimate initial group angles, β_i and number of sources, Q.
- Calculate preliminary focusing angles using the group angles:

For RSS: use $\beta_i, \beta_i - 0.25 * Beamwidth, \beta_i + 0.25 * Beamwidth.$

For HSST: use $\beta_i, \beta_i - 0.1 * Beamwidth, \beta_i + 0.1 * Beamwidth.$

- Initialize the transformed measurement covariance matrix $\boldsymbol{R}(f_o)$ to zeros.
- For K sub-bands:

Estimate the narrow band covariance matrix, $\boldsymbol{R}(f_k)$.

If $Q = 1$, build diagonal focusing matrix $T(f_k)$.

If $Q > 1$, build RSS or HSST focusing matrix $\boldsymbol{T}(f_k)$.

Update $\boldsymbol{R}(f_o) = \boldsymbol{R}(f_o) + \boldsymbol{T}(f_k)\boldsymbol{R}(f_k)\boldsymbol{T}(f_k)^H$.

- Use MUSIC to estimate the wideband spectrum using $\boldsymbol{R}(f_o)$.

To demonstrate the functionality of the algorithm, a Monte Carlo simulation using four uncorrelated sources at 8, 13, 33, and 35 degrees was done, and the following results were obtained. An eight-element uniform linear array of omnidirectional sensors was used like in [55].

For each of the 100 snapshots used, a processing band of 80 to 120 Hz (f_0 is 100 Hz) is traversed by $K = 33$ frequency bins.

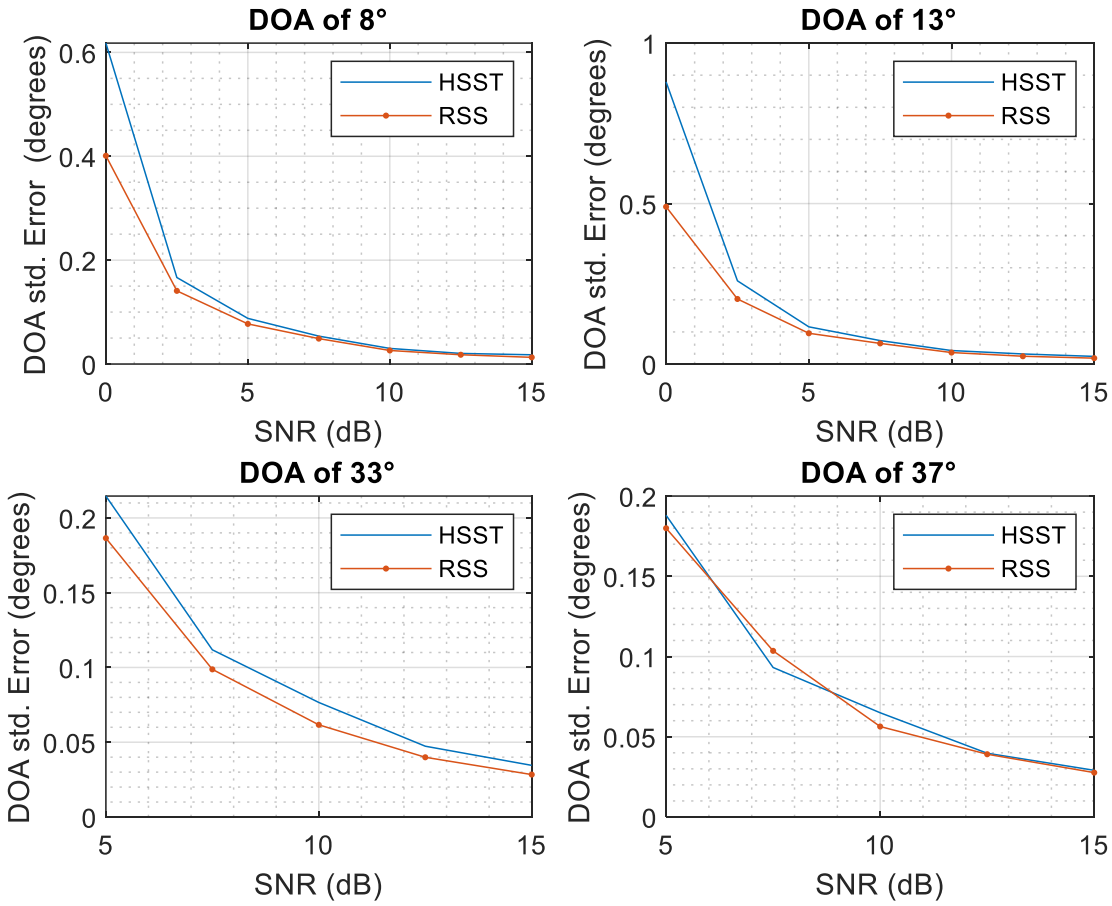

Figure 4-1: The sample statistics of the bearing errors for the RSS and HSST methods.

RSS method has comparable performance as HSST method except at low SNR values. Figure 4-2 shows that the DOAs can be correctly estimated using the MUSIC algorithm.

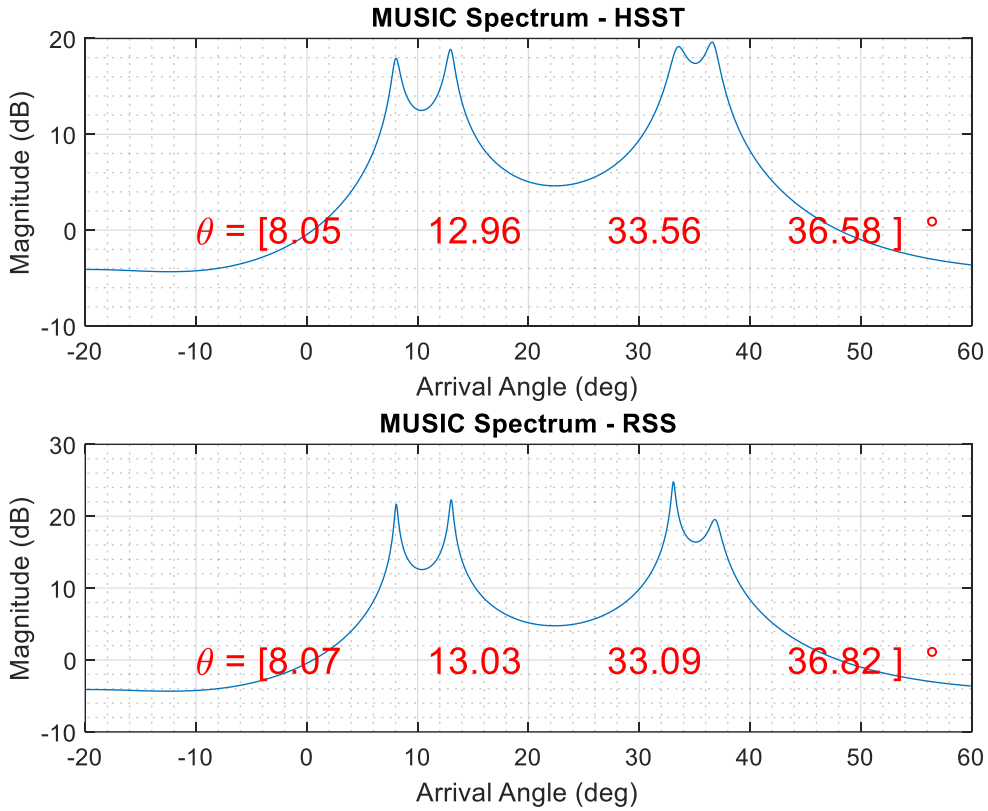

Figure 4-2: MUSIC Spectrum for RSS and HSST methods.

4.5 Comparison of Focusing Matrices with Other Wideband Methods

DOA mean square error (MSE) analysis is used to compare the focusing matrices method against other wideband methods such as wideband MLE, wideband MUSIC, and wideband MVDR and the results are shown in Figure 4-3 and Figure 4-4. From these plots, we see that the extra processing cost of using focusing matrices may not be advantageous over the other wideband methods currently being used in radar depth sounder data processing.

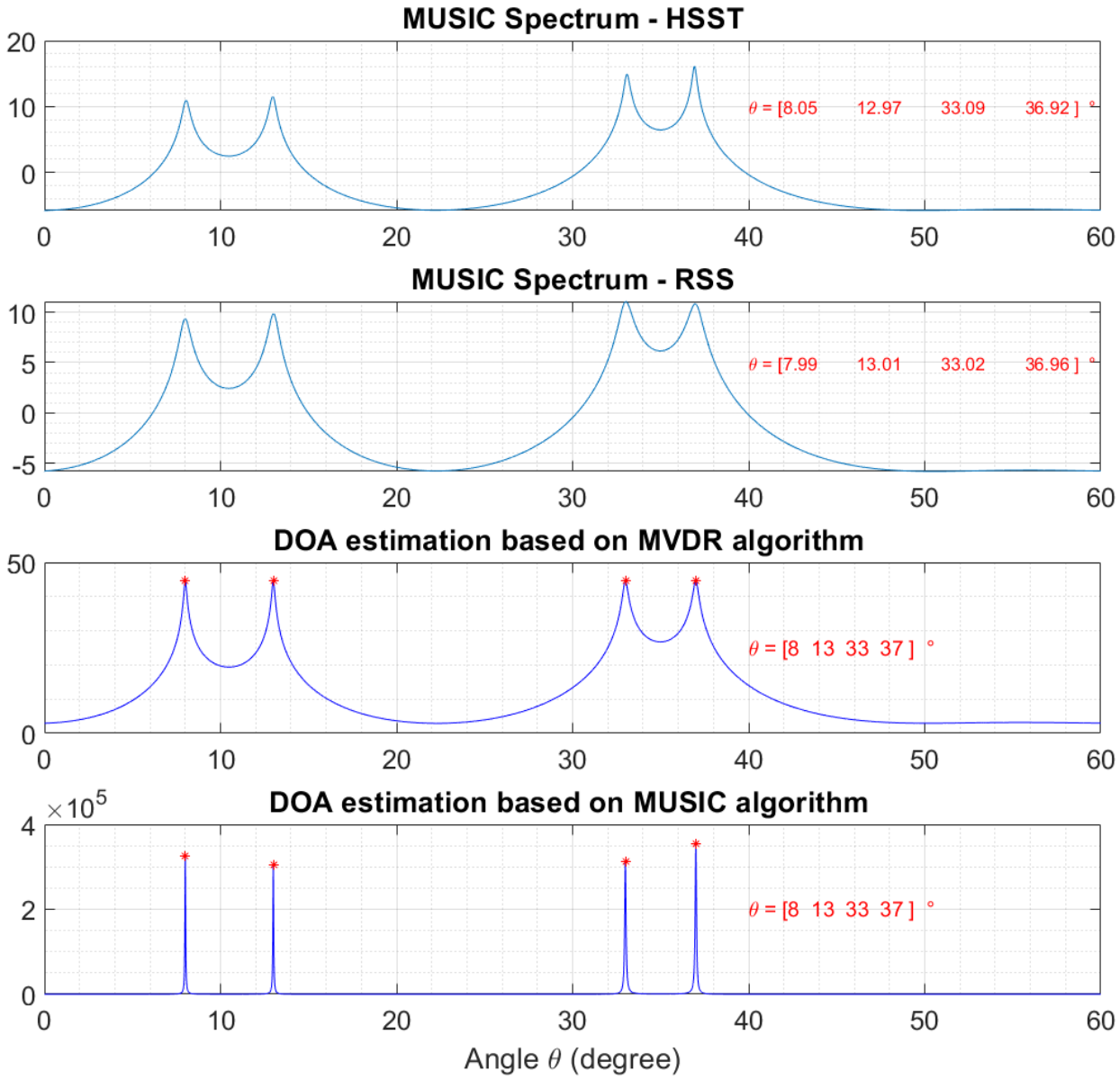

Figure 4-3: Comparison with other wideband methods.

The MUSIC and MVDR spectra (Figure 4-3) are superior to the spectrum obtained using focusing matrices. Likewise, the RMSE plot (Figure 4-4) shows no clear advantage of using focusing matrices over MUSIC and MVDR.

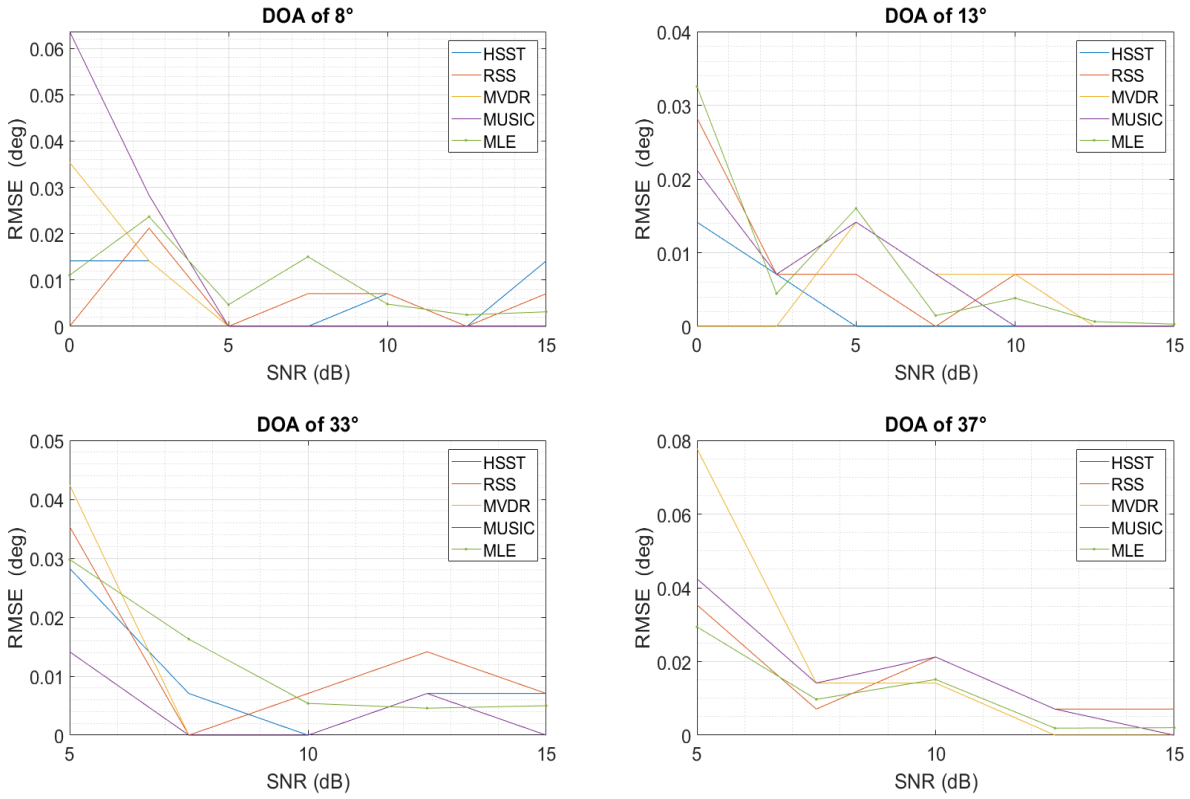

Figure 4-4: RMSE comparison with other wideband methods

5 CONCLUSIONS AND FUTURE WORK

The work presented in this dissertation aims to measure the vertical velocity of ice sheets using differential interferometric synthetic aperture radar (DInSAR) techniques. The research explores using a maximum likelihood estimator to jointly estimate the vertical velocity, cross-track internal layer slope, and unknown baseline error due to GPS and inertial navigation system errors. The joint estimation framework produces results for baseline errors, vertical velocity, and cross-track slope, which are validated against ground-based and crossover analysis results. The research findings demonstrate that the joint estimation framework can estimate the vertical velocity profile from airborne radar data with reasonable accuracy, especially within the region where the echogram data quality is good.

The study also investigates the use of focusing matrices against other wideband direction of arrival methods. The results suggest that the extra processing cost of focusing matrices may not be advantageous over the other wideband methods currently used in radar depth sounder data processing.

This work contributes to understanding ice flow in glaciers and ice sheets. It has potential applications for improving models used in predicting the behavior of ice sheets in response to climate change.

5.1 Future Work

The joint estimation framework presented in this dissertation could be further improved by incorporating machine learning or artificial intelligence techniques (e.g., feature extraction, post-processing and analysis). Machine learning techniques can be used to extract relevant features from SAR data and other auxiliary data, such as topography and surface elevation, that can be used as inputs to the Maximum likelihood joint estimation framework. Artificial intelligence techniques

can be used to post-process and analyze the Maximum likelihood joint estimation framework's outputs, such as identifying patterns or anomalies in the estimated parameters. These can lead to more accurate and efficient estimation of ice sheet vertical velocity and tomography measurements. These techniques can be explored to further improve the accuracy and robustness of the joint estimation framework.

The current joint estimation framework presented in this work can be further improved by incorporating additional information, such as the ice temperature and density, which can affect the ice rheology and flow.

While this work focused on Greenland, DInSAR techniques can be applied to other regions to obtain vertical velocity measurements and improve our understanding of ice flow dynamics. This can help to refine existing ice flow models and improve predictions of future ice sheet and glacier behavior under different climate scenarios.

6 REFERENCES

1. Swords, S.S., *Radar fundamentals*, in *Technical History of the Beginnings of Radar*. IET. p. 5-41.
2. Rohling, H., *From Huelsmeyer's telemobiloskop to the digital radar*, in *2014 11th European Radar Conference*. 2014, IEEE.
3. Cohen, E.A. and R. Buderi, *The Invention That Changed the World: How a Small Group of Radar Pioneers Won the Second World War and Launched a Technological Revolution.* Foreign Affairs, 1997. **76**(2): p. 179.
4. Richards, M.A., Scheer, J. A., & Holm, W. A. , *Principles of Modern Radar: Basic principles*. 2010, Institution of Engineering and Technology.
5. Saeedi, J., *Feasibility Study and Conceptual Design of Missile-Borne Synthetic Aperture Radar*. IEEE Transactions on Systems, Man, and Cybernetics: Systems, 2017. **PP**: p. 1-12.
6. Massom, R. and D. Lubin, *Polar Remote Sensing.* Ice Sheets, 2006. **II**.
7. Fernando Rodríguez-Morales, et al., *Advanced Multifrequency Radar Instrumentation for Polar Research.* IEEE TRANSACTIONS ON GEOSCIENCE AND REMOTE SENSING, 2013.
8. Raju, G., W. Xin, and R.K. Moore, *Design, Development, Field Observations, and Preliminary Results of the Coherent Antarctic Radar Depth Sounder (CARDS) of the University of Kansas, U.S.A.* Journal of Glaciology, 1990. **36**: p. 247 - 254.
9. Davies, B. *A introduction to the hierarchy of ice-sheet models*. 2020; Available from: https://www.antarcticglaciers.org/glaciers-and-climate/numerical-ice-sheet-models/hierarchy-ice-sheet-models-introduction/.

10. Reigber, A. and R. Scheiber, *Airborne differential SAR interferometry: first results at L-band.* IEEE Transactions on Geoscience and Remote Sensing, 2003. **41**(6): p. 1516-1520.

11. Moreira, A., et al., *A tutorial on synthetic aperture radar.* IEEE Geoscience and Remote Sensing Magazine, 2013. **1**(1): p. 6-43.

12. Ager, T., *An Introduction to Synthetic Aperture Radar Imaging.* Oceanography, 2013. **26**.

13. Tomiyasu, K., *Tutorial review of synthetic-aperture radar (SAR) with applications to imaging of the ocean surface.* Proceedings of the IEEE, 1978. **66**(5): p. 563-583.

14. Ferretti, A., et al., *InSAR Principles: Guidelines for SAR Interferometry Processing and Interpretation* 2007: European Space Agency (ESA) Publications.

15. Madsen, S.N., A. Zebker, and J. Martin, *Topographic Mapping Using Radar Interferometry: Processing Techniques.* IEEE Transactions on Geoscience and Remote Sensing, 1993. **31**(1): p. 246-256.

16. Alaska_Satellite_Facility. *How to Create an Interferogram Using ESA's Sentinel-1 Toolbox*. [cited 2020 August]; Available from: https://asf.alaska.edu/how-to/data-recipes/create-an-interferogram-using-esas-sentinel-1-toolbox/.

17. European_Space_Agency_(ESA). *InSAR processing: a practical approach*. Available from: http://www.esa.int/esapub/tm/tm19/TM-19_ptB.pdf.

18. Gatelli, F., et al., *The Wavenumber Shift in SAR Interferometry.* Geoscience and Remote Sensing, IEEE Transactions on, 1994. **29**: p. 855-865.

19. Rosen, P.A., et al., *Synthetic aperture radar interferometry.* Proceedings of the IEEE, 2000. **88**(3): p. 333-382.

20. Brook, N.A.G. *Introduction to SAR Interferometry –Generating a Digital Elevation Model (DEM).* Applied Remote Sensing Trainning Program.

21. Abedin, M.J. and A.S. Mohan. *Localization of near-field radiating sources with an arbitrary antenna array*. in *2008 IEEE Antennas and Propagation Society International Symposium*. 2008.

22. Stoica, P. and R. Moses, *Spectral analysis of signals*. 2005: Prentice Hall. 268-271.

23. Schmidt, R., *Multiple emitter location and signal parameter estimation.* IEEE Transactions on Antennas and Propagation, 1986. **34**(3): p. 276-280.

24. Athinarapu, S., et al., *Model order estimators using optimal and suboptimal methods with numerical tuning.* 2018 IEEE Radar Conference (RadarConf18), 2018: p. 1537-1542.

25. Al-Ibadi, M., et al., *Wideband Model Order Estimation Using Machine Learning.* 2019 IEEE International Symposium on Phased Array System & Technology (PAST), 2019: p. 1-7.

26. M.Wax and T. Kailath, *Detection of signals by information theoretic criteria.* IEEE Transactions on Acoustics, Speech and Signal Processing, 1985. **33**: p. 387-392.

27. Wang, H. and M. Kaveh, *Coherent signal-subspace processing for the detection and estimation of angles of arrival of multiple wide-band sources.* IEEE Transactions on Acoustics Speech Signal Processing, 1985. **ASSP-33**: p. 823-831.

28. Ziskind, I. and M. Wax, *Maximum likelihood localization of multiple sources by alternating projection.* IEEE Transactions on Acoustics, Speech, and Signal Processing, 1988. **36**(10): p. 1553-1560.

29. Doron, M.A., A.J. Weiss, and H. Messer, *Maximum-Likelihood Direction Finding of Wide-Band Sources.* IEEE Transactions on Signal Processing, 1993. **41**(1): p. 411.

30. Cumming, I.G. and F.H.-c. Wong, *Digital processing of synthetic aperture radar data : algorithms and implementation*. 2005, Boston: Artech House.

31. Carcione, J.M., L.T.P. Feliciangeli, and M. Zamparo, *The exploding-reflector concept for ground-penetrating-radar modeling.* Annals of Geophysics, 2002. **45**.

32. Cai, L., *Ultra-Wide-Band Model-Based Synthetic Aperture Radar Imaging through Complex Media*. 2000, Ohio State University.

33. Skjelvareid, M., et al., *Synthetic Aperture Focusing of Ultrasonic Data From Multilayered Media Using an Omega-K Algorithm.* Ultrasonics, Ferroelectrics and Frequency Control, IEEE Transactions on, 2011. **58**: p. 1037-1048.

34. Tammana, C.L.a.S.G.a. *SAR Processing of Radar Echo Sounder Data*. 2000.

35. CRESIS *Radar Depth Sounder*.

36. Bailey Miller, et al. *Multipass SAR processing for radar depth sounder clutter suppression, tomographic processing, and displacement measurements.* in *2020 IEEE International Geoscience and Remote Sensing Symposium*. 2020.

37. Nicholls, K.W., et al., *A ground-based radar for measuring vertical strain rates and time-varying basal melt rates in ice sheets and shelves.* Journal of Glaciology, 2015. **61**(230): p. 1079-1087.

38. Paden, J., et al., *Ice-sheet bed 3-D tomography.* Journal of Glaciology, 2010. **56**(195): p. 3-11.

39. Kingslake, J., et al., *Full-depth englacial vertical ice-sheet velocities measured using phase-sensitive radar.* Journal of Geophysical Research: Earth Surface, 2014. **119**.

40. Gillet-Chaulet, F., et al., *In-situquantification of ice rheology and direct measurement of the Raymond Effect at Summit, Greenland using a phase-sensitive radar.* Geophysical Research Letters, 2011. **38**(24).

41. Gabriel, A.K., R.M. Goldstein, and H.A. Zebker, *Mapping small evaluation changes over large areas: Differential radar interferometry.* Journal of Geophysical Research, 1989. **94**: p. 9183.

42. Goldstein, R.M., et al., *Satellite Radar Interferometry for Monitoring Ice Sheet Motion: Application to an Antarctic Ice Stream.* Science, 1993. **262**(5139): p. 1525-1530.

43. Sansosti, E., R. Lanari, and P. Lundgren. *Dynamic deformation of Etna volcano observed by satellite radar interferometry*. in *IGARSS '98. Sensing and Managing the Environment. 1998 IEEE International Geoscience and Remote Sensing. Symposium Proceedings. (Cat. No.98CH36174)*. 1998.

44. Massonnet, D. and K.L. Feigl, *Satellite radar interferometric map of the coseismic deformation field of the M = 6.1 Eureka Valley, California Earthquake of May 17, 1993.* Geophysical Research Letters, 1995. **22**(12): p. 1541-1544.

45. Chang, H.C., L. Ge, and C. Rizos, *DInSAR for mine subsidence monitoring using multi-source satellite SAR images*. 2005, Institute of Electrical and Electronics Engineers (IEEE): Piscataway, NJ. p. 1742-1745.

46. Ferretti, A., C. Prati, and F. Rocca, *Nonlinear subsidence rate estimation using permanent scatterers in differential SAR Interferometry.* Geoscience and Remote Sensing, IEEE Transactions on, 2000. **38**: p. 2202-2212.

47. Ferretti, A., C. Prati, and F. Rocca, *Permanent scatterers in SAR interferometry. IEEE Trans Geosci Remot Sen.* Geoscience and Remote Sensing, IEEE Transactions on, 2001. **39**: p. 8-20.

48. Sophie, N. and S. Helene, *Projections of Future Sea Level Contributions from the Greenland and Antarctic Ice Sheets: Challenges Beyond Dynamical Ice Sheet Modeling.* Oceanography, 2018. **31**.

49. Castelletti, D., et al., *Permanent Scatterers in Repeat-Pass Airborne VHF Radar Sounder for Layer-Velocity Estimation.* IEEE Geoscience and Remote Sensing Letters, 2020: p. 1-5.

50. Zebker, H.A. and J. Villasenor, *Decorrelation in interferometric radar echoes.* IEEE Transactions on Geoscience and Remote Sensing, 1992. **30**(5): p. 950-959.

51. Theresa Moore, J.P., *ARRAY MANIFOLD CALIBRATION FOR MULTICHANNEL RADAR ICE SOUNDERS*, in *IEEE International Geoscience and Remote Sensing Symposium*. 2020.

52. Koenig, L., et al., *Annual Greenland accumulation rates (2009–2012) from airborne snow radar.* The Cryosphere, 2016. **10**: p. 1739-1752.

53. Joughin, I., R. Kwok, and M. Fahnestock, *Estimation of ice-sheet motion using satellite radar interferometry: method and error analysis with application to Humboldt Glacier, Greenland.* Journal of Glaciology, 1996. **42**: p. 564-575.

54. Mousavi, S., et al., *Wideband Autocorrelation Radiometry for Lake Icepack Thickness Measurement With Dry Snow Cover*. IEEE Geoscience and Remote Sensing Letters, 2019. **16**(10): p. 1526-1530.

55. Hung, H. and M. Kaveh, *Focussing matrices for coherent signal-subspace processing.* IEEE Transactions on Acoustics, Speech and Signal Processing, 1988. **36**(8): p. 1272-1281.

56. Doron, M.A. and A.J. Weiss, *On Focusing Matrices for Wide-Band Array Processing.* IEEE Transactions on Signal Processing, 1992. **40**(6): p. 1295-1302.

7 APPENDIX

7.1 Processing of Non-contiguous Radar Transmission Spectra

This is a draft of a paper being prepared for submission to *the IEEE Transactions on Radar Systems*. This work on *processing of non-contiguous Radar transmission spectra* was undertaken before the main Ph.D. research objective was streamlined and therefore it is only included here in the appendix. The authors are Gordon Ariho, James M. Stiles, and Peng Sen Tan.

***Abstract*— In recent times, the issue of spectral congestion has become a growing concern in the radar community. Furthermore, the telecommunications industry has been advocating for access to segments of the spectrum that have traditionally been generously allocated to radar systems. To address this issue, an information theoretic approach is used to design optimally "thinned" transmission spectra. However, this thinning of the spectrum can lead to a degradation in estimation accuracy. In scenarios where there is a sparse target profile, reduced estimation performance can be deemed acceptable, and the bandwidth can be thinned to improve spectral efficiency. Achieving spectral efficiency allows for the freeing of portions of the radar bandwidth, enabling spectrum sharing between radar and other wireless systems. To process the thinned spectra, an iterative reduced-rank minimum mean-square error (MMSE) algorithm is proposed. This algorithm is applied to the radar measurement model, with simulated target profiles used to evaluate the algorithm's performance. The results demonstrate the effectiveness of the proposed iterative algorithm and the potential for achieving significant spectral efficiency gains through the thinning of the radar spectrum. This work is of particular interest to researchers and practitioners in the fields of radar systems and telecommunications, where efficient spectrum utilization is crucial for meeting increasing demand.**

***Index Terms*— Sparse spectrum, MMSE, Iterative Reduced-Rank MMSE, Spectral Efficiency, Spectrum Sharing.**

I. INTRODUCTION

Radar applications have enjoyed generous frequency allocations within the UHF band for a long time. However, with the increasing demand for bandwidth-hungry applications in other communication systems and spectral congestion within radar systems, this privileged status can no longer be sustained indisputably. Spectrum is a costly resource and radar technologies must now be designed with spectral efficiency in mind. Within the radar array processing framework, spectral efficiency can be defined as the optimal use of bandwidth to achieve acceptable performance with minimal degradation as if the original full bandwidth were still in use, enabling lower bandwidth occupancy. Spectral efficiency further requires that the radar has good spectral containment within its allocated bandwidth to avoid interfering with other wireless applications' signals, taking into consideration the high-power transmission typical of active radars. Consequently, if this spectral efficiency could be achieved, then some portions of the radar bandwidth can be freed to facilitate spectrum sharing between radar with other wireless communications systems.

If the spectrum is modeled as a summation of distinct spectral lines, then a contiguous spectrum can be represented by the expression in equation (1) for a pulsed radar:

$$s(\omega) = \sum_{n-1}^{N} s_n \delta(\omega - n\omega) \tag{1}$$

where $s(\omega)$ is the original contiguous spectrum, N is the number of spectral lines, each defined by the Dirac-Delta function $\delta(\omega)$ shifted by a frequency location $n\omega$, and s_n is the weighting.

By inspection of (1) for a pulsed radar system, it can be seen that spectral thinning can be

performed by optimally removing some spectral lines without degrading the radar resolution. The remainder of the spectral lines can now be spaced at any frequency interval as long as it is lower than the pulse repetition frequency (to avoid range ambiguity). This is equivalent to pulse repetition interval jittering in pulsed radar. If we consider each spectral line as an individual narrow-band coherent transmitter/receiver, then the contiguous spectrum can be represented by a uniform linear array (ULA) in which each array element (a coherent transmitter/receiver) corresponds to a spectral line. Linear arrays allow many different array patterns to be synthesized depending on how each element is excited [1].

It can be shown that when the ULA is not filled (hence a non-uniform array at this point), it can still achieve almost similar performance to the original filled ULA with some estimation degradation. Consequently, higher peak side-lobe levels (PSL) and higher integrated side-lobe levels (ISL) can occur leading to possible false alarm detection and higher target estimation error variance respectively. The level of degradation in performance is directly proportional to the number of removed elements [1]. These removed spectral lines can be utilized by other wireless applications. Marginal Fisher's Information (MFI) [2] is used to design informationally-optimal sparse spectra as detailed in [1]. These MFI generated sparse spectra are used to study the performance of the reduced-rank minimum mean-square error (RRMMSE) algorithm being proposed here.

When the classic one-step MMSE is applied to low-sample support cases, it results in either many false alarms or missed detections of the real targets of interest. Reduced-rank MMSE (RRMMSE) is proposed for low-sample support situations where it is applied iteratively to perform estimation of sparse targets within range. The proposed RRMMSE is related to compressive sensing, matched pursuits, and clean algorithm. Compressive sensing uses fewer measurements than conventional methods to recover signals by taking advantage of the signal sparsity and sensing incoherence [3].

Matched pursuit incrementally constructs a series of sparse approximations to the signal [4]. The clean algorithm is primarily a deconvolution method that is used to clean noisy observed data in order to recover a sparse illumination distribution, for example, stars in the sky [5].

One of the previous research done on RRMMSE involved algorithms that employ correlation-subtraction architecture based on the multistage Wiener filter [6]. In this research, it is demonstrated that the reduced rank algorithm performed as good as the full-rank MMSE when sufficient sample support was ensured. This is achieved without implementing eigen-decomposition, matrix inversion, or construction of blocking matrices, which would be computationally expensive. Another RRMMSE algorithm that is proposed in [7], is based on a classification algorithm and a release-merge adaptive partition algorithm which updated the partition and the receiver's coefficients concurrently. This algorithm is shown to perform better than the previously proposed ones such as the partial despreading MMSE receiver and the cyclically shifted filter bank receiver, with even a smaller number of taps [8]. This paper seeks to expound and propose a statistical iterative reduced-rank MMSE algorithm by building on work done in [1].

II. Problem Formulation

To model the received radar signal, a general linear model is considered (2):

$$\mathbf{v} = \mathbf{H}\,\boldsymbol{\gamma} + \mathbf{n} \tag{2}$$

where $\mathbf{v}$ is a $K \times 1$ radar measurement vector, $\mathbf{H}$ is a $K \times M$ observation matrix (sensing matrix), $\boldsymbol{\gamma}$ is an $M \times 1$ vector with each element γ_i corresponding to the complex scattering coefficient of an individual target within range, and $\mathbf{n}$ is complex measurement noise vector (Gaussian). The matrix $\mathbf{H}$ defines the propagation characteristics of a channel for a given transmit signal.

A sparse transmit spectrum results in a matrix $\mathbf{H}^H\mathbf{H}$ that is less than full rank (i.e., insufficient independent measurements for the number of unknowns!). Frequently, the range profile $\boldsymbol{\gamma}$ is not

full rank since there are many resolution cells without detectable targets. For these cases, a sparse transmit spectrum might be informationally sufficient to estimate $\boldsymbol{\gamma}$. The problem is to determine the subspace of $\mathbf{H}^H\mathbf{H}$ where detectable targets exist. An iterative approach has been developed, wherein a reduced-rank MMSE is used to iteratively identify and construct this detectable target subspace.

A. Cramer-Rao Lower Bound (CRLB) and Marginal Fisher Information

From the linear model in (2), we can denote the estimation of the vector $\boldsymbol{\gamma}$ with $\widetilde{\boldsymbol{\gamma}}$. There is always an error associated with this estimation of $\boldsymbol{\gamma}$, such that the estimated $\widetilde{\boldsymbol{\gamma}}$ will not be identical to the original $\boldsymbol{\gamma}$. The estimation error, $\boldsymbol{\epsilon}$, and corresponding covariance matrix, $\mathbf{K}_\epsilon$, when using the MMSE estimator can be obtained as follows:

$$\boldsymbol{\epsilon} = \widetilde{\boldsymbol{\gamma}} - \boldsymbol{\gamma} \tag{3}$$

$$\mathbf{K}_\epsilon = \mathbb{E}\{\boldsymbol{\epsilon}\boldsymbol{\epsilon}'\} \tag{4}$$

The lower bound of the error covariance is given by the Cramer-Rao Lower Bound (CRLB) [9]. The CRLB is equal the inverse of the Fisher Information matrix of the measurement vector which can be expressed by:

$$\mathbf{J} = \mathbb{E}\left\{\left[\nabla\boldsymbol{\gamma} \ln\left(f_{(v|\gamma)}(\mathbf{v})\right)\right]\left[\nabla\boldsymbol{\gamma} \ln\left(f_{(v|\gamma)}(\mathbf{v})\right)\right]^H\right\} \tag{5}$$

where ∇ is the gradient operator and $f_{(v|\gamma)}(\mathbf{v})$ is the probability density function of $\mathbf{v}$ given $\boldsymbol{\gamma}$.

MFI is a measure of the new information gained when the K^{th} spectral element is added to the $(K-1)^{th}$ previous spectral elements. It can be viewed as the reduction in uncertainty from an information theory perspective. The Marginal Fisher Information matrix obtained from the K^{th} spectral element is defined as the nonnegative definite matrix $\Delta\mathbf{I}(K)$ given by:

$$\Delta\mathbf{I}(K) = \mathbf{J}_{K-1}^{-1} - \mathbf{J}_K^{-1} \tag{6}$$

where $\mathbf{J}_K$ is the Fisher Information matrix obtained from K spectral elements in vector $\mathbf{v}$, and $\mathbf{J}_{K-1}$ is the Fisher Information matrix from $(K-1)$ spectral elements.

From the MFI matrix, $\Delta\mathbf{I}(K)$, the MFI from the K^{th} spectral elements is defined as:

$$\text{MFI} = \frac{1}{M} \times \text{Tr}\big(\Delta\mathbf{I}(K)\big) \tag{7}$$

where $\text{Tr}(\cdot)$ is the trace operator and M is the number of elements (targets) in the vector $\boldsymbol{\gamma}$. Equation (7) can further be written as:

$$\text{MFI} = \frac{1}{M} \times [\text{Tr}(\mathbf{J}_{K-1}^{-1}) - \text{Tr}(\mathbf{J}_K^{-1})] \tag{8}$$

which can also be written in terms of the covariance matrix as:

$$\text{MFI} = \frac{1}{M} \times \left[\text{Tr}\big(\mathbf{K}_{\epsilon(K-1)}\big) - \text{Tr}\big(\mathbf{K}_{\epsilon(K)}\big)\right] \tag{9}$$

MFI measures the incremental change in information resulting from one change in elemental design. It is analogous to Mutual information in Shannon information theory.

The sparse spectra used in this research are generated based on the MFI algorithm developed in [1] where a more detailed expose of the algorithm is given. For completeness of this paper, a high-level description of the construction of the sparse arrays using the MFI algorithm is provided. MFI measures the change in information resulting in one individual element in relation to the remainder of the elements in the sensor. In [1], it is shown that the construction of the sparse spectrum by employing the MFI metric can be achieved by removing either a block of frequencies or an individual frequency at a time during the optimization process. The approach of using a block of frequencies at a time allows for construction of practical sparse spectrum that is less granulated. The single spectral line at a time approach leads to a resultant sparse spectrum with small gaps that are not practical for reuse in other applications. Optimal spectral locations for the frequency blocks

are determined iteratively using the MFI metric. The frequency block size used in this paper is 1.25\% of the filled spectrum. Investigation done with other block sizes is not included in this paper. The interval between adjacent frequency samples within each block satisfies the Nyquist sampling requirement.

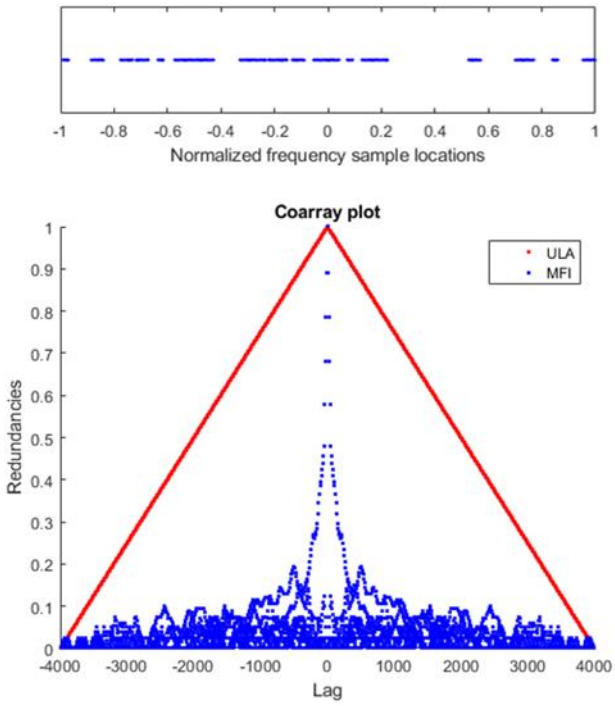

Fig. 1. 50% bandwidth sparse spectrum

The coarray, $c(l)$, of a sparse array is defined as the autocorrelation of the element weights [11] and it is used to evaluate the constructed sparse spectrum arrays.

$$c(l) = \sum_{n=0}^{N-|l|-1} w_n w_{n+|l|} \tag{10}$$

where $w_n \in \{0,1\}$ is the element weight that corresponds to the presence (1) or absence (0) of the array element at location n and N is the total number of elements in the filled array. When $c(l) > 1$, l is a redundant lag whereas for $c(l) = 0$ the coarray has a hole at lag l. A perfect array should

have a coarray with no holes or redundancies except for lag zero. These perfect arrays do not exist for $n > 4$.

MFI is used to iteratively construct sparse, non-contiguous radar transmission spectra that is informationally optimal. We showcase the 50% and 75% filled spectra in Fig.1 and Fig.2, respectively. These figures show the MFI generated frequency locations (top), and the corresponding coarray (bottom).

The MMSE estimator (11) is applied to the radar measurement vector from (2) to obtain the estimated $\tilde{\boldsymbol{\gamma}}$ as shown (12):

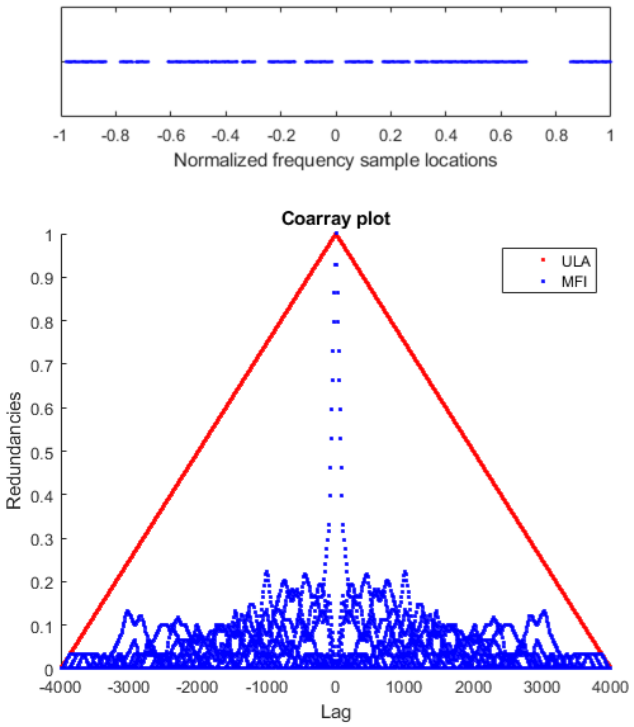

Fig. 2. 75% bandwidth sparse spectrum

$$\mathbf{W}_{MMSE} = \mathbf{K}_{\gamma}\mathbf{H}^{H}\left(\mathbf{H}\mathbf{K}_{\gamma}\mathbf{H}^{H} + \mathbf{K}_{n}\right)^{-1} \tag{11}$$

$$\tilde{\boldsymbol{\gamma}} = \mathbf{W}_{MMSE}\mathbf{v} \tag{12}$$

where $\mathbf{K}_\gamma$ is the a priori target covariance matrix and $\mathbf{K}_n$ is the covariance matrix due to the measurement noise. Correspondingly, the error covariance when using the MMSE estimator can be given by:

$$\mathbf{K}_\epsilon = \mathbf{K}_\gamma - \mathbf{K}_\gamma \mathbf{H}^H \left(\mathbf{H}\mathbf{K}_\gamma \mathbf{H}^H + \mathbf{K}_n\right)^{-1} \mathbf{H}\mathbf{K}_\gamma \tag{13}$$

which is equivalent to [10]:

$$\mathbf{K}_\epsilon = \left(\mathbf{H}^H \mathbf{K}_n^{-1} \mathbf{H} \ + \mathbf{K}_\gamma^{-1}\right)^{-1} \tag{14}$$

Since the Fisher information matrix, $\mathbf{J}_K$ is equal to the inverse of the error covariance matrix, $\mathbf{K}_\epsilon$, then $\mathbf{J}_K$ can be written as:

$$\mathbf{J}_K = \left(\mathbf{H}^H \mathbf{K}_n^{-1} \mathbf{H} \ + \mathbf{K}_\gamma^{-1}\right) \tag{15}$$

If $\mathbf{K}_\gamma$ and $\mathbf{K}_n$ are defined as $\sigma_\gamma^2 \boldsymbol{I}$ and $\sigma_n^2 \boldsymbol{I}$ respectively, then (14) and (15) can be rewritten as (16) and (17) respectively:

$$\mathbf{K}_\epsilon = \left(\sigma_n^{-2} \mathbf{H}^H \mathbf{H} \ + \sigma_\gamma^{-2} \boldsymbol{I}\right)^{-1} \tag{16}$$

$$\mathbf{J}_K = \left(\sigma_n^{-2} \mathbf{H}^H \mathbf{H} \ + \sigma_\gamma^{-2} \boldsymbol{I}\right) \tag{17}$$

III. RRMMSE ALGORITHM

The flow chart in fig.3 highlights the iterative RRMMSE algorithm. The algorithm starts by assuming that there is only one target and takes the highest estimate to be the only target. In the next iteration, the algorithm assumes there are two targets and takes the highest two estimates as the true targets. This goes on until all the targets are estimated. The number of targets should be less than or equal to spectral lines within the thinned spectrum for this algorithm to work. The key performance metric is the mean-squared error of the scattered range profile estimate. The baseline for the evaluation is a conventional fully filled (i.e. contiguous) transmission spectrum and matched filtering.

The iterative RRMMSE is applied to the measurement vector $\mathbf{v}$ and the simulated range profile

estimated. The MATLAB simulation is setup as described below:

Initialization: Detectable sparse targets $\boldsymbol{\gamma}$ are simulated to occupy 10%, 20%, 30%, 40%, 50% and 60% of the resolution cells using random permutation. The target profile amplitude ranges from -10 to 30dB. The complex Gaussian noise, $\mathbf{n}$ is generated as: $\mathbf{K}_n = \sigma_n^2 \boldsymbol{I}$. The apriori sensing matrix (normalized response to each range bin), $\mathbf{H}$ is generated. The apriori target covariance matrix, $\mathbf{K}_\gamma$ is generated as $\mathbf{K}_\gamma = \sigma_\gamma^2 \boldsymbol{I}$. The linear observation model is implemented as: $\mathbf{v} = \mathbf{H}\,\boldsymbol{\gamma} + \mathbf{n}$.

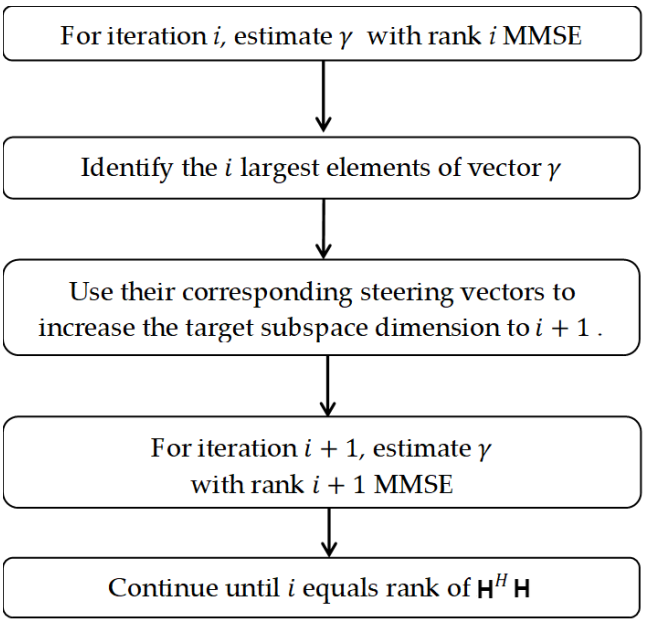

Fig. 3. Iterative Reduced-Rank MMSE

Iterative Reduced Rank MMSE: The RRMMSE estimator is applied to the measurement vector, and the target scattering coefficient γ_i among all M possible targets in the range profile that has the largest magnitude identified. This is assumed to be the true value of the target at this location; $\tilde{\boldsymbol{\gamma}} = \mathbf{W}_{MMSE}\mathbf{v}$ where, $\mathbf{W}_{MMSE} = \mathbf{K}_\gamma \mathbf{H}^H \left(\mathbf{H}\mathbf{K}_\gamma \mathbf{H}^H + \mathbf{K}_n\right)^{-1}$. The apriori target covariance matrix $\mathbf{K}_\gamma$ for the location in the radar range profile is then updated using: $\sigma_\gamma^2 = \tilde{\gamma}^2 + \sigma_\epsilon^2$. Since it can be shown that $\mathbf{H}\mathbf{K}_\gamma\mathbf{H}^H = \sum_m \sigma_{\gamma m}^2 H_m H_m^H$, we can update only $\mathbf{K}_\gamma$ instead of the sensing matrix $\mathbf{H}$.

For the next iterations, the RRMMSE estimator is applied to the set of all combinations of G target scattering coefficients with each G-target combinations consisting of the already tracked (identified) target locations $(j_1, j_2, \ldots, j_{G-1})$ along with the g^{th} target location. From the set of M combinations of the estimated G-element $\tilde{\gamma}_G$, the g^{th} target location to be identified is the location that has the largest magnitude among all the M locations excluding $(j_1, j_2 \ldots, j_{G-1})$. The current estimated values of the target scattering coefficients $(\gamma_{j1}, \gamma_{j2}, \ldots, \gamma_{jg})$ are assumed to hold the true values of the targets at these locations. Like in the first step, the a priori target covariance matrix $\mathbf{K}_\gamma$ is updated.

The iterations continue till the average mean square error (MSE) of all M targets in the error covariance matrix, $\mathbf{K}_\epsilon$ converge: $\mathbf{K}_\epsilon = \mathbf{K}_\gamma - \mathbf{K}_\gamma \mathbf{H}^H \left(\mathbf{H}\mathbf{K}_\gamma \mathbf{H}^H + \mathbf{K}_n\right)^{-1} \mathbf{H}\mathbf{K}_\gamma$.

This iterative RRMMSE estimator algorithm (summarized in fig.3) is applied to each of the target profile scenarios and the result is a computationally tractable estimate of range profile $\boldsymbol{\gamma}$, with near MMSE accuracy.

IV. Results and Discussion

The reduced-rank MMSE algorithm described above is applied to the different sparse spectra and the mean square error (MSE) performance analyzed. Different target profiles which are a percentage of range cells with detectable targets are used: 10%, 20%, 30%, 40%, 50% and 60%. Key results that demonstrate a particular pattern are showcased here. The average MSE from the error covariance matrix and the average MSE from ground truth are calculated using (18) and (19) respectively.

$$\mathrm{MSE}_{K_\epsilon} = \frac{1}{M} \times \mathrm{Tr}(\mathbf{K}_\epsilon) \tag{18}$$

$$\mathrm{MSE}_{GT} = \frac{1}{M} \times [(\boldsymbol{\gamma} - \tilde{\boldsymbol{\gamma}})^H (\boldsymbol{\gamma} - \tilde{\boldsymbol{\gamma}})] \tag{19}$$

The baseline for this evaluation is a conventional fully filled (i.e. contiguous) transmission spectrum

and matched filtering.

Matched filtering provides extremely poor estimate accuracy for thinned transmit spectra as shown in fig.4 and fig.5 for the 20% and 50% detectable targets using 50% and 75% filled spectrum respectively.

Fig.6 illustrates the gradual improvement in estimation accuracy with increasing iterations. The first snapshot shows that the target estimation is still poor because this is a matched filter result. The next snapshot shows an improvement in estimation of the targets, and this gets better till the significant targets are all estimated as shown in the last snapshot of the process.

The Iterative Reduced-Rank MMSE estimator can provide excellent estimation accuracy for all, but the smallest targets as shown in fig.7 and fig.8 for the 20% and 50% detectable targets using 50% and 75% filled spectrum respectively.

If the number of detectable targets is less than the measurement rank, a sparse spectrum can be as effective as a fully filled transmit bandwidth. Thinning the spectrum will increase time to convergence as shown in fig. 9 and increasing the number of detectable scatterers in the range profile will also increase time to convergence as shown in fig.10. Fig. 10 shows that the 100% target profile estimation with a 75% filled spectrum doesn’t converge since the target profile is greater than the 75% filled spectrum.

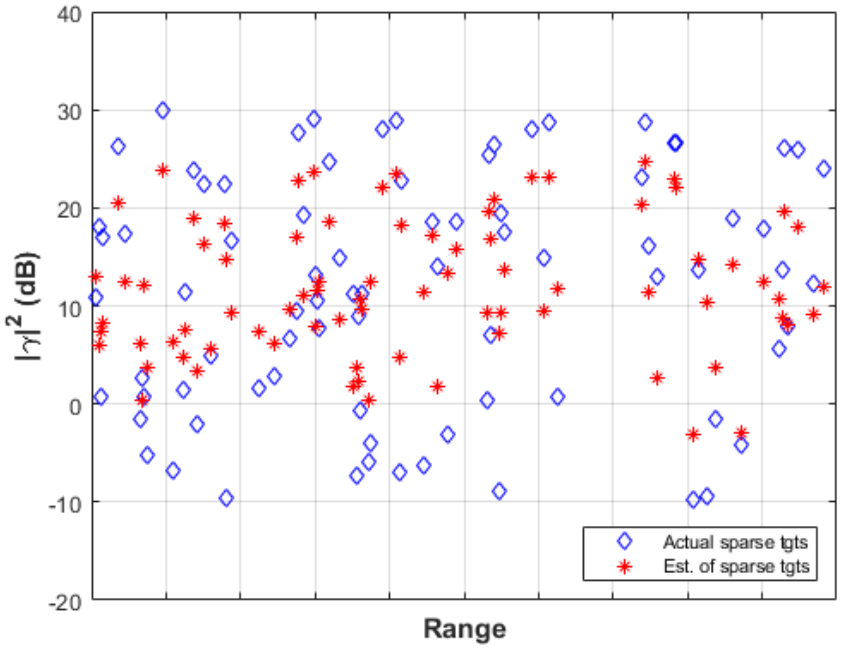

Fig. 4. Matched filtering: 20% detectable targets, 50% filled spectrum.

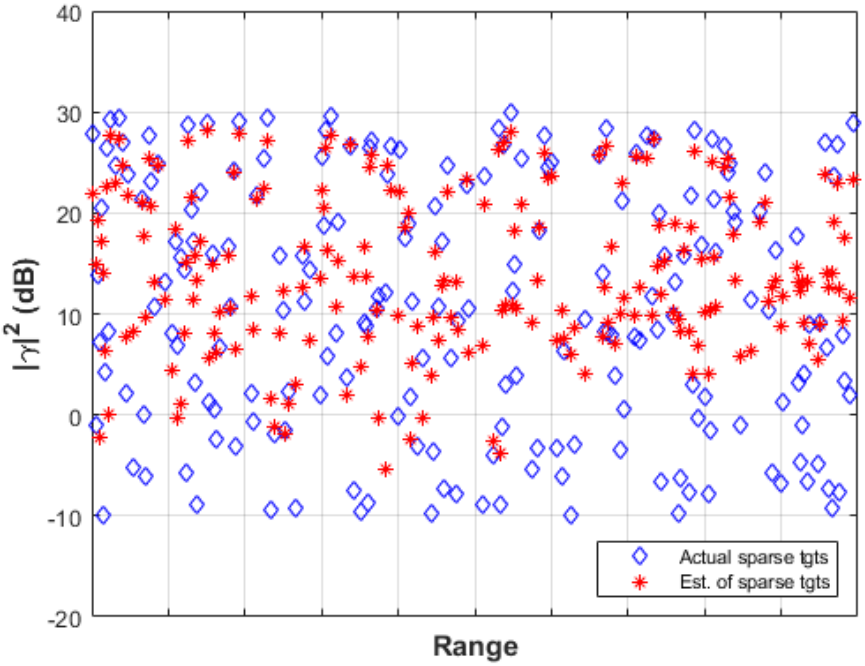

Fig. 5. Matched filtering: 50% detectable targets, 75% filled spectrum.

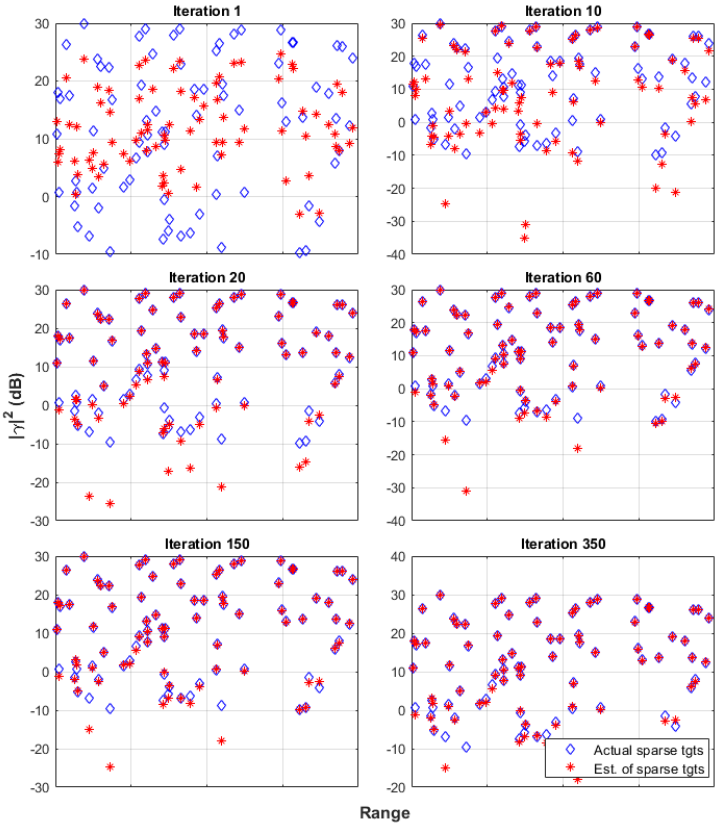

Fig. 6. Iteration Snapshots: 20% detectable targets, 50% filled spectrum.

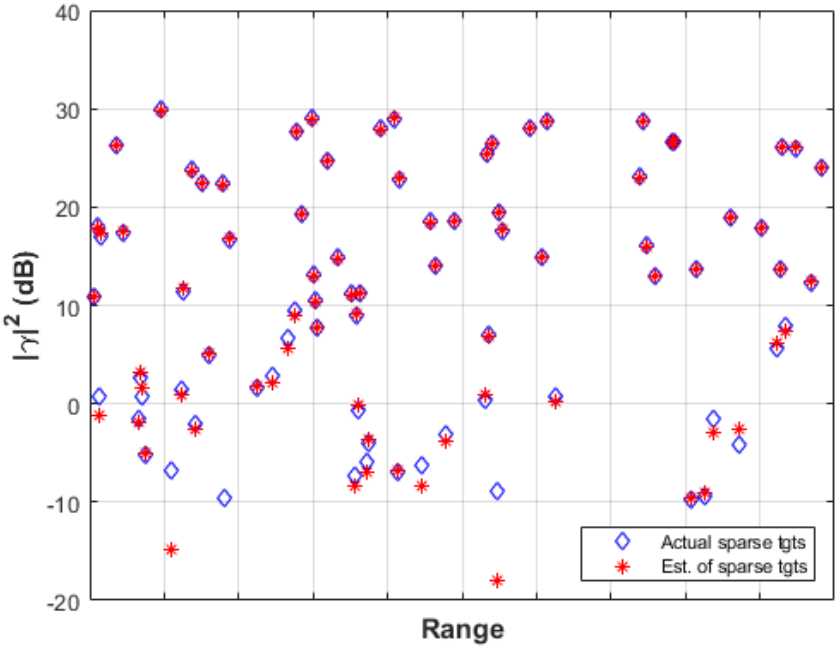

Fig. 7. Iterative RRMMSE: 20% detectable targets, 50% filled spectrum.

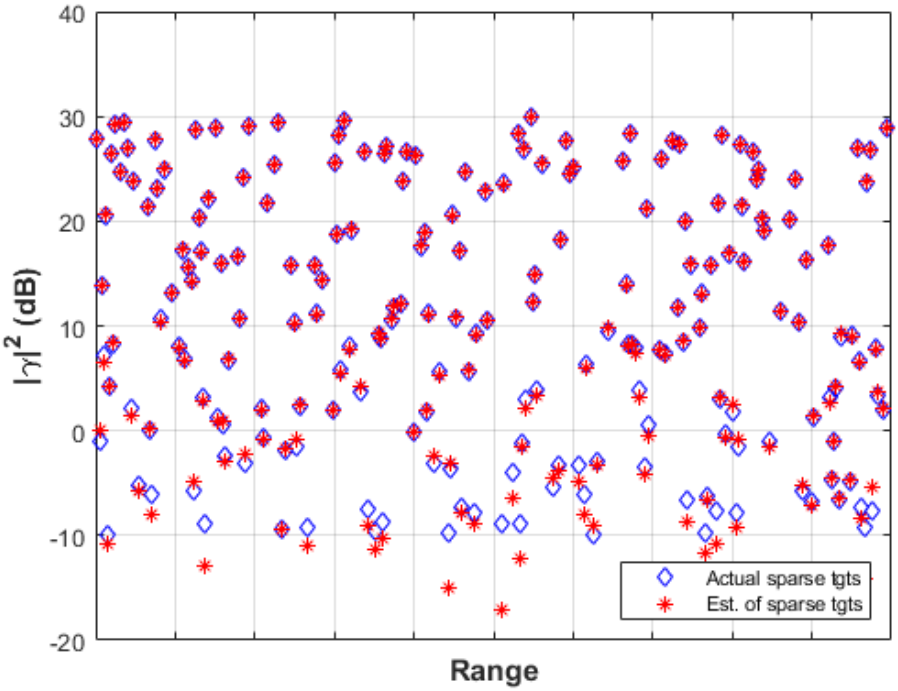

Fig. 8. Iterative RRMMSE: 50% detectable targets, 75% filled spectrum.

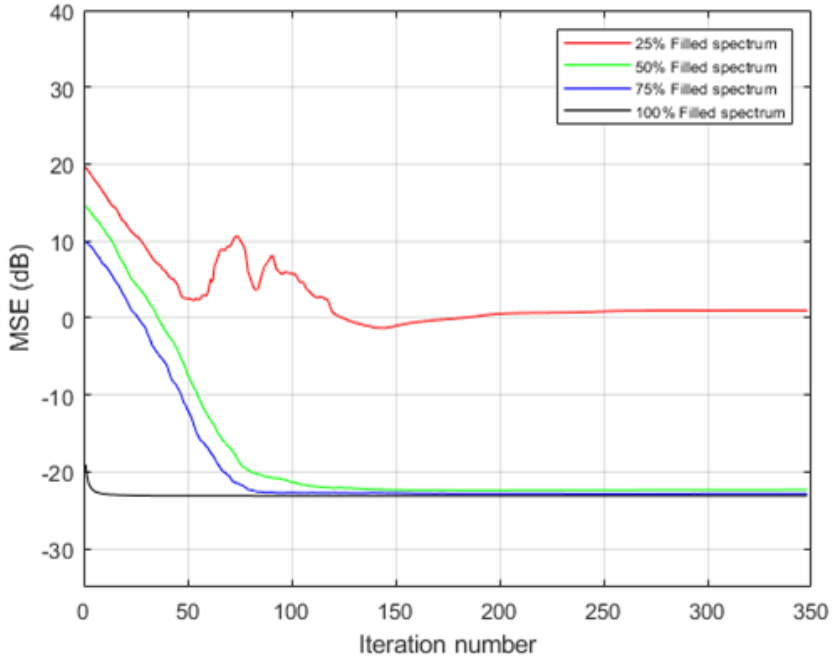

Fig. 9. Estimation Error: 20% detectable targets.

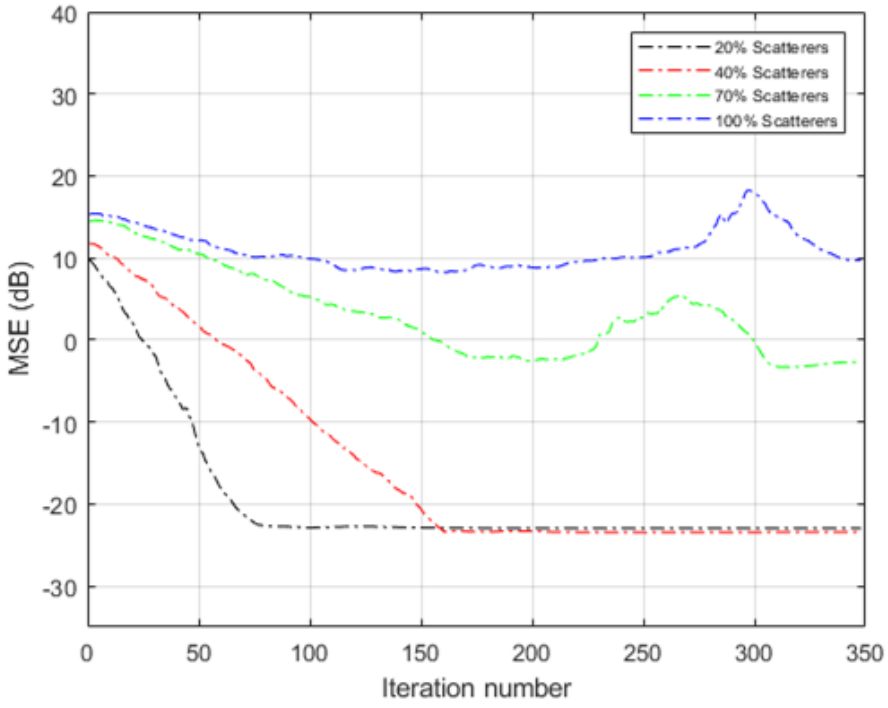

Fig. 10. Estimation Error: 75% filled spectrum.

V. Conclusion

The iterative reduced-rank minimum mean-square error (RRMMSE) algorithm has been demonstrated to perform well in scenarios where the target profile is less than the sparse spectrum size. Furthermore, the effectiveness of the iterative RRMMSE algorithm has been shown in various sparse array scenarios where the sparse spectrum is greater than or equal to the target profile. The versatility of this algorithm allows for its application to MFI generated sparse spectra, uniform sparse spectra, randomly generated sparse spectra, or any other type of sparse spectra. This proposed algorithm has the potential to be extended to other areas such as direction of arrival (DOA) estimation, where the target profile is sparse. It is important to note that the proposed RRMMSE algorithm is related to compressive sensing, matched pursuits, and clean algorithm. The creation of spectral gaps through the thinning of the radar transmission spectrum can facilitate spectrum sharing, provided that other wireless emitters exist exclusively within these spectral gaps.

Additionally, the use of a sparse spectrum processed iteratively with RRMMSE can be as effective as a fully filled transmit bandwidth, as long as the number of detectable targets is less than the measurement rank. Overall, the proposed iterative RRMMSE algorithm holds promise for mitigating the effects of spectral congestion and enabling efficient spectrum sharing between radar and other wireless systems, while maintaining acceptable estimation accuracy in sparse target profile scenarios.

ACKNOWLEDGMENT

We acknowledge support from the NSF Center for Surveillance Research.

REFERENCES

[1] P. S. Tan, J. M. Stiles, and S. D. Blunt, "Optimizing sparse allocation for radar spectrum sharing", in *IEEE Radar Conference (RadarConf)*, 2016/05, http://dx.doi.org/10.1109/radar.2016.7485150

[2] J. Stiles and J. Jenshak, "Sparse Array Construction using Marginal Fisher's Information", in *International Waveform Diversity and Design Conference*, 2009/02, http://dx.doi.org/10.1109/wddc.2009.4800345.

[3] Y. Wang, H. Bai and Y. Zhao, "Image Reconstruction from Patch Compressive Sensing Measurements," in *IEEE Fourth International Conference on Multimedia Big Data (BigMM)*, 2018, pp. 1-4, doi: 10.1109/BigMM.2018.8499088.

[4] Liu Yin, Wu Shunjun, Wu Mingyu and Li Chunmao, "ESPRIT matching pursuit algorithm for DOA estimation with single snapshot," in *IEEE CIE International Conference on Radar*, 2011, pp. 315-318, doi: 10.1109/CIE-Radar.2011.6159540.

[5] R. Bose, "Active CLEAN: A Modified CLEAN Algorithm for HRRPs of Contiguous Targets with Thinned Spectrum," in *IEEE Transactions on Aerospace and Electronic Systems*, vol. 48, no. 2, pp. 930-939, APRIL 2012, doi: 10.1109/TAES.2012.6178039.

[6] S. Sud, W. L. Myrick, J. S. Goldstein, and M. D. Zoltowski, "A reduced rank MMSE receiver for a DS-CDMA system in frequency selective multipath", *IEEE*, vol. 2, pp. 1109-1113, 2001.

[7] Z. Guo and K. B. Letaief, "A low complexity reduced-rank MMSE receiver for DS/CDMA communications", *IEEE Transactions on Wireless Communications*, vol. 2, pp. 59-68, 2003.

[8] R. Singh and L. B. Milstein, "Adaptive interference suppression for DS-CDMA", *IEEE Transactions on Communications*, vol. 50, no. 12, pp. 1902-1905, 2002/12 2002.

[9] S. M. Kay, *Fundamentals of Statistical Signal Processing* - Estimation Theory, Volume I, Prentice Hall Signal Processing Series, New Jersey, 1993.

[10]S. K. Sengupta and S. M. Kay, "Fundamentals of Statistical Signal Processing: Estimation Theory", *Technometrics*, vol. 37, no. 4, p. 465, 1995/11 1995.

[11]J.-F. H. S. Holm, "The Coarray of Sparse Arrays with Minimum Sidelobe Level", *IEEE NORSIG-98*, pp. 137–140, June 1989.